



DEVELOPMENT OF A STAR TRACKER-BASED
REFERENCE SYSTEM
FOR ACCURATE ATTITUDE DETERMINATION OF A
SIMULATED SPACECRAFT

THESIS

Jorge Padro, Captain, USAF

AFIT/GAE/ENY/12-M32

DEPARTMENT OF THE AIR FORCE
AIR UNIVERSITY

AIR FORCE INSTITUTE OF TECHNOLOGY

Wright-Patterson Air Force Base, Ohio

APPROVED FOR PUBLIC RELEASE; DISTRIBUTION UNLIMITED

The views expressed in this thesis are those of the author and do not reflect the official policy or position of the United States Air Force, the Department of Defense, or the United States Government. This material is declared a work of the U.S. Government and is not subject to copyright protection in the United States.

AFIT/GAE/ENY/12-M32

DEVELOPMENT OF A STAR TRACKER-BASED REFERENCE SYSTEM
FOR ACCURATE ATTITUDE DETERMINATION OF A SIMULATED
SPACECRAFT

THESIS

Presented to the Faculty
Department of Aeronautics and Astronautics
Graduate School of Engineering and Management
Air Force Institute of Technology
Air University
Air Education and Training Command
In Partial Fulfillment of the Requirements for the
Degree of Master of Science in Aeronautical Engineering

Jorge Padro, B.S., Mechanical Engineering
Captain, USAF

March 2012

APPROVED FOR PUBLIC RELEASE; DISTRIBUTION UNLIMITED

DEVELOPMENT OF A STAR TRACKER-BASED REFERENCE SYSTEM
FOR ACCURATE ATTITUDE DETERMINATION OF A SIMULATED SPACECRAFT

Jorge Padro, B.S., Mechanical Engineering
Captain, USAF

Approved:

<hr/>	<hr/>
//signed//	07 March 2012
Eric D. Swenson, PhD (Chairman)	Date
<hr/>	<hr/>
//signed//	07 March 2012
Ronald J. Simmons, Lt Col, USAF (Member)	Date
<hr/>	<hr/>
//signed//	07 March 2012
William E. Wiesel, PhD (Member)	Date

Abstract

The goal of this research effort is to investigate the analysis, design, integration, testing, and validation of a complete star tracker and star field simulator system concept for AFIT's satellite simulator, SimSat. Previous research has shown that while laboratory-based satellite simulators benefit from star trackers, the approach of designing the star field can contribute significant error if the star field is generated on a flat surface. To facilitate a star pattern that better represents a celestial sky, a partially hemispherical dome surface is suspended above SimSat and populated with a system of light emitting diodes of various intensities and angles of separation. Test results show that the spherical star pattern surface is effective in minimizing the effects of parallax when imaging in a finite conjugate mode and that more reliable attitude information within 1 degree of accuracy can be attained. The added capability to research star pattern recognition and attitude determination algorithms in the future is also significant.

Look Mom! Look Dad!! No Hands!!!

Acknowledgements

First and foremost, I wish to express my immense appreciation to the ENY department and to my research advisor, Dr. Eric Swenson. Dr. Swenson always supported my ideas, added in his own, and helped keep things focused whenever I had trouble seeing 'the forest for the trees'. His support and enthusiasm towards my research efforts were exactly what I needed to get the job done.

Next, I'd like to thank the ENY laboratory technicians led by Jay Anderson. During my extensive time spent in their labs and shops, I've witnessed first-hand how much they clean up their students' messes, figuratively and literally. I can say without a doubt that the successes each lab student from ENY may or may not acknowledge on this page are in no small part to the hard work and dedication of this team. A special thanks to Jay Anderson, Chris Zickefoose, and Jorge Ureña for the many hours and skillful work they've dedicated to this project.

I also wish to thank the AFIT model shop for building the necessary mounting hardware and helping to prepare the SkyDome, especially Brian Crabtree. Their work was timely and efficient, and Brian's feedback was key to ensuring that everything was done right the first time.

Finally, I want to thank my friends and family for their unending support. Your understanding of my efforts and enthusiasm for my work are what kept me going throughout this challenging time. Thank you for believing in me.

Jorge Padro

Table of Contents

	Page
Abstract	iv
Acknowledgements	vi
List of Figures	x
List of Tables	xiv
List of Acronyms	xv
I. Introduction	1
1.1 Background	1
1.2 Problem Statement	4
1.3 Research Objectives	5
1.4 Methodology	5
1.5 Preview	6
II. Background	7
2.1 Spacecraft Attitude Determination	7
2.2 Spacecraft Dynamics	9
2.2.1 Reference Frames	9
2.2.2 Rotation Matrices	11
2.2.3 Quaternions	13
2.3 Star Tracker Operation	16
2.3.1 Technical Characteristics	16
2.3.2 Accuracy	20
2.3.3 Ideal Pinhole Camera	23
2.3.4 Vector Mapping	24
2.4 Star Pattern Recognition Algorithm	25
2.4.1 Overview	25
2.4.2 Angle Algorithm	29
2.4.3 Mapping	34
2.4.4 Error Estimation	34
2.4.5 The Direct Match Test	35
2.4.6 Star and Pair Catalogs	37
2.4.7 Star Pattern Recognition Algorithm Summary	41
2.5 Attitude Determination Algorithm	41
2.5.1 Overview	41
2.5.2 QUEST Algorithm	43

	Page
2.5.3 Attitude Determination Algorithm Summary	47
2.6 Laboratory Testing	47
2.7 Satellite Simulators	50
2.7.1 AFIT SimSat	50
2.7.2 NPS TAS-2	52
2.8 Summary	56
III. Methodology	57
3.1 Introduction	57
3.2 Key Requirements	57
3.3 SimSat Star Camera and Lens System	60
3.4 LED Development	62
3.4.1 LED Preliminary Studies	62
3.4.2 LED Controller	78
3.4.3 Final LED Sub-System Concept	81
3.5 Star Field Surface Development	84
3.5.1 Flat Surface Analysis	84
3.5.2 Spherical Surface Analysis	88
3.5.3 Dome Specification and Production	89
3.5.4 Dome Installation and Measurement	93
3.6 MATLAB [®] Algorithm	96
3.6.1 Configuration	96
3.6.2 Common Functions	96
3.6.3 Calibration	99
3.6.4 Cataloging	101
3.6.5 Pattern Recognition	101
3.6.6 Attitude Determination	101
3.7 System Validation	102
3.7.1 LED Testing	102
3.7.2 Dome Surface Testing	102
3.7.3 Algorithm Testing	104
3.8 Summary	106
IV. Results and Analysis	107
4.1 Introduction	107
4.2 Test 1 Results	107
4.3 Test 2 Results	110
4.4 Test 3 Results	116
4.4.1 Test 3 Calibration	118
4.4.2 Test 3 Star Pattern Recognition and Attitude Determination	124
4.5 Summary	131

	Page
V. Conclusion and Recommendations	133
5.1 Conclusion	133
5.2 Recommendations for Future Development	137
5.2.1 Star Representation Improvements	137
5.2.2 Star Field Improvements	138
5.2.3 Algorithm Improvements	139
Appendix A. Supplemental Results Figures	141
A.1 Test 1 Results	141
A.2 Test 2 Results	147
A.3 Test 3 Results	152
Bibliography	159
Vita	161

List of Figures

Figure		Page
1	SimSat II Current Configuration	4
2	Relation Between the Celestial Sphere and a Spacecraft Reference Frame	8
3	Typical Attitude Determination Process Flowchart	9
4	Earth-Centered Inertial and Body-Fixed Frames	10
5	Observed Stars in the Tracker Frame	11
6	3-2-1 Rotation Sequence from Inertial to Star Tracker Frame	13
7	Euler Axis Rotation Relating Frame A to B	14
8	Star Tracker Operational Sketch	16
9	Ideal Pinhole Camera Assumption	23
10	Star Image Centroid Illustration	24
11	Mapped Star Vectors in the Tracker Frame	26
12	Typical Attitude Determination Algorithm Flowchart	27
13	Angle Method	27
14	Planar Triangles Method	28
15	Spherical Triangle Method	29
16	Star Tracker Data	31
17	Primary Pair and Candidate Selection	32
18	The Primary Assumption	33
19	The Direct Match Test - Correct Mapping	36
20	The Direct Match Test - Incorrect Mapping	37
21	Boeing Star Catalog Architecture	38
22	Fixed Star Tracker Testbed	48
23	Minituarized Optical Simulator	49
24	JPL Optical Simulator	50
25	SimSat Previous Configuration	51

Figure		Page
26	NPS TAS-2 with monitor	53
27	Vector Representation of Flat Star Field and Reference Frames . . .	54
28	Equal Separation Angles from Two Observation Points	60
29	Lumenera Lu205c Camera	62
30	Preliminary light emitting diode (LED) Radiation Pattern Plots . .	65
31	Preliminary LED Physical Characteristics	66
32	Patch Board Pattern	66
33	Patch Board Schematic	67
34	Patch Board	68
35	SimSat with Preliminary LED Test Stand	69
36	Patch Board Image Focus and Aperture Adjustments	71
37	Star Recognition Thresholding	73
38	Multi-Positional LED Brightness Variations	75
39	Patch Board with Sanded LEDs	76
40	Multi-Positional Brightness Variations of Diffuse LEDs	77
41	Arduino Mega 2560	78
42	Simplified pulse-width modulation (PWM) Graph	79
43	PWM Analysis on Color LEDs with Duty Cycles Displayed	81
44	Final LED Radiation Pattern Plot	82
45	Final Patch Board Preparation	83
46	PWM Analysis on White LEDs with Duty Cycles Displayed	84
47	Flat Surface Geometric Analysis	85
48	Flat Surface Image Plane Analysis	86
49	Spherical Surface Geometric Analysis	88
50	Spherical Surface Image Plane Analysis	89
51	Hemispherical Dome Design Sketch	91
52	Dome Sketch with Actual Contour Measurement Overlaid	92
53	Spherical Air Bearing Cup Measurement	94

Figure		Page
54	Dome FARO Arm Probing	95
55	Laser Level Alignment and Apex Location	96
56	Algorithmic Vector Frame Transformation Illustration	98
57	Image Frame Calibration Screen	100
58	LED Test SimSat Position 1	103
59	Dome Test SimSat Position 1	104
60	Dome Test SimSat Positions 2 (left) and 3 (right)	105
61	Algorithm Test SimSat Position 1	106
62	Test 1 Snapshot, Position 1	108
63	Test 1 Snapshots, Positions (clockwise from top left): 2, 3, 4, and 5	109
64	Test 1 Magnitude Distribution Across Positions, by LED	110
65	Test 1 Magnitude Distribution Across Positions, Combined	111
66	Test 1 Angular Separation Distribution Across Positions, Combined	113
67	Test 2 Snapshot, Position 1	113
68	Test 2 Snapshot, Positions 2 (top) and 3 (bottom)	114
69	Test 2 Magnitude Distribution Across Positions, by LED	114
70	Test 2 Magnitude Distribution Across Positions, Combined	115
71	Test 2 Angular Separation Distribution Across Positions, Combined	115
72	Test 3 Snapshot, Position 1	117
73	Test 3 Snapshots, Positions (clockwise from top left): 2, 3, 4, and 5	118
74	Test 3 Magnitude Distribution Across Positions, by LED	119
75	Test 3 Magnitude Distribution Across Positions, Combined	120
76	Test 3 Angular Separation Distribution Across Positions, Combined	121
77	Test 3 LED X, Y Inertial Coordinate Distributions, Combined	123
78	Test 3 LED Z Inertial Coordinate Distributions, Combined	124
79	Test 3 Mean X-Y Coordinate Scatter Plot	125
80	Test 3 Attitude Estimation Visualization, Position 1	126
81	Test 3 Attitude Estimation Visualization, Position 2	127

Figure		Page
82	Test 3 Attitude Estimation Visualization, Position 3	128
83	Test 3 Attitude Estimation Visualization, Position 4	129
84	Test 3 Attitude Estimation Visualization, Position 5	131
85	Test 1: Magnitude Distribution at Position 1, by LED	141
86	Test 1: Magnitude Distribution at Position 2, by LED	142
87	Test 1: Magnitude Distribution at Position 3, by LED	143
88	Test 1: Magnitude Distribution at Position 4, by LED	144
89	Test 1: Magnitude Distribution at Position 5, by LED	145
90	Test 1: Magnitude Distribution at Positions 1 and 2, Combined . .	146
91	Test 1: Magnitude Distribution at Positions 3 and 4, Combined . .	146
92	Test 1: Magnitude Distribution at Position 5, Combined	146
93	Test 2: Magnitude Distribution at Position 1, by LED	147
94	Test 2: Magnitude Distribution at Position 2, by LED	148
95	Test 2: Magnitude Distribution at Position 3, by LED	149
96	Test 2: Magnitude Distribution by Position, Combined	150
97	Test 2: Angular Separation Distribution by Position	151
98	Test 3: Magnitude Distribution at Position 1, by LED	152
99	Test 3: Magnitude Distribution at Position 2, by LED	153
100	Test 3: Magnitude Distribution at Position 3, by LED	154
101	Test 3: Magnitude Distribution at Position 4, by LED	155
102	Test 3: Magnitude Distribution at Position 5, by LED	156
103	Test 3: Magnitude Distribution at Positions 1 and 2, Combined . .	157
104	Test 3: Magnitude Distribution at Positions 3 and 4, Combined . .	157
105	Test 3: Magnitude Distribution at Position 5, Combined	158

List of Tables

Table		Page
1	Image Plane Dimension vs. Vehicle Orientation - Flat Star Field . . .	87
2	Test 1 Mean Instrument Magnitude Data Across All Positions . . .	112
3	Test 2 Mean Positional Instrument Magnitude Values (Non-Dimensional)	112
4	Test 2 Standard Deviation Values of Mean Positional Instrument Magnitudes	112
5	Test 2 Mean Angular Separation Data Across by Position	116
6	Test 3 Inertial Measurement Unit (IMU) Euler Angle Data for Each Position	118
7	Test 3 Mean Instrument Magnitude Data Across All Positions . . .	119
8	Test 3 Mean Separation Angle Values Across All Positions	122
9	Test 3 Algorithm Error Values	124
10	Test 3 Attitude Estimation Results, Position 1	127
11	Test 3 Attitude Estimation Results, Position 2	128
12	Test 3 Attitude Estimation Results, Position 3	129
13	Test 3 Attitude Estimation Results, Position 4	130
14	Test 3 Attitude Estimation Results, Position 5	130
15	Test 3 Attitude Estimation Results, Position 5	131

List of Acronyms

ACS	attitude control system
AFIT	Air Force Institute of Technology
APS	Active Pixel Sensor
ASC	Acquisition Star Catalog
CCD	Charge-Coupled Device
CMOS	complimentary metal-oxide semiconductor
CTE	charge transfer efficiency
CMG	control moment gyroscope
ECI	Earth-Centered Inertial
FOV	field of view
IMU	Inertial Measurement Unit
LED	light emitting diode
LOS	line of sight
LIS	Lost in Space
NPS	Naval Postgraduate School
NEA	noise equivalent angle
PC	Pair Catalog
PWM	pulse-width modulation
QE	Quantum Efficiency
QUEST	Quaternion Estimation
TAS-2	Second-Generation Three-Axis Spacecraft

DEVELOPMENT OF A STAR TRACKER-BASED REFERENCE SYSTEM FOR ACCURATE ATTITUDE DETERMINATION OF A SIMULATED SPACECRAFT

I. Introduction

1.1 *Background*

Attitude determination is a key component of spacecraft operations, especially in applications requiring positioning and pointing accuracy. A satellite's (generalized as a "spacecraft" or "vehicle" in this thesis) attitude is defined as the orientation of its fixed body frame with respect to an external reference frame, typically an inertial frame. Attitude determination is the process by which the spacecraft utilizes either internal and/or external sensory information to estimate its attitude. Depending on its mission, a spacecraft may be required to point a camera, sensor, or communications equipment towards a specific planetary or celestial location. Another concurrent application is the need for a satellite to point its solar panel arrays towards the sun and its thermal radiators away from the sun. With multiple, simultaneous, and often precise pointing requirements for modern spacecraft, the need for a timely, accurate attitude solution has been a catalyst for increased interest in attitude determination since the dawn of the space age. Without accurate attitude determination, a "Lost-in-Space" case may develop, whereby a loss of dependable attitude information can result in precision pointing failure, loss of power and, in extreme cases, the spacecraft tumbling uncontrollably in space.

Several attitude determination methods have been developed since the inception of spaceflight. Aside from the many internal sources of attitude information, such as inertial or gyroscopic measurement methods, the space environment provides numer-

ous external references from which the attitude of a spacecraft may be compared to and ultimately determined. The known position of the sun and moon, relative to the spacecraft and to the Earth, may be used for a satellite in orbit. The magnetic field of the Earth can also be measured and used to estimate the spacecraft's attitude. However, the sun and moon are generally not in permanent view of an orbiting satellite, and utilizing the magnetic field of the Earth for attitude determination is not an accurate method. The celestial sky, however, is visible the majority of the time.

Determining a spacecraft's attitude using the celestial sky is facilitated using vector observations of stars relative to the spacecraft. Specially-designed sensor hardware, known as star trackers or star sensors, detect stars in a portion of the celestial sky, record specific features of these stars, and report a sensor-fixed direction vector to the detected stars. Comparing these vectors to premeasured, inertial-fixed vectors is central to the various attitude determination algorithms developed over the years. The star data collected between the two observations must typically first be matched in order to identify the portion of the celestial sky the sensor recently imaged. Then, orientation information is determined from this matching that allows the star tracker to report a best-estimated attitude solution for the spacecraft.

However, star tracking is not completely independent of measurement noise, both systematic and non systematic, which contributes appreciable errors in measurement and to which much research has been dedicated. Various star tracker sensor types and configurations have been developed to both improve the overall accuracy of the star tracker and allow the numerous end-users with flexibility in choosing the particular variant that best suites their mission applications. Additionally, the algorithms tasked with identifying stars and determining attitude solutions are designed to facilitate or mitigate applied error estimates to guarantee a solution exists with varying degrees of accuracy. The degree of accuracy then depends on the noise and

distortions related to the imaging optics, sensor, and algorithms used. There is a large choice of algorithms to incorporate in a star tracker system (20, 22, 5), each with characteristic operating parameters and associated advantages and disadvantages. While improved methods for pattern recognition and attitude determination have resulted over the course of four decades of study, algorithms with increased accuracy are typically more computationally expensive, and thus a balance is usually sought between the desired accuracy versus the system-level requirements to facilitate the increased computations.

In light of the relatively small inherent error associated with star trackers, star trackers are an obvious choice for application onto modern laboratory-based spacecraft dynamics simulators. Indeed, a sun sensor-based system would be the simplest to implement, but would only provide one reference vector which limits the spacecraft's ability to determine its orientation. A magnetometer, while sufficiently accurate, would require construction of an all-encompassing Helmholtz cage or similar magnetic field device around the spacecraft simulator. On the other hand, star trackers inherently provide the minimally-required two reference vectors. Since such simulators exhibit a limited range of orientations, the required star field surface need only be sized to provide coverage over the portion of possible simulator orientations. Furthermore, research simulators allow a large degree of flexibility with regards to accuracy requirements for its on-board sensors. Thus, implementing a star tracker-based external reference system only requires the installation of an additional sensor, a properly-designed, minimally-intrusive star field surface, and the proper software algorithms.

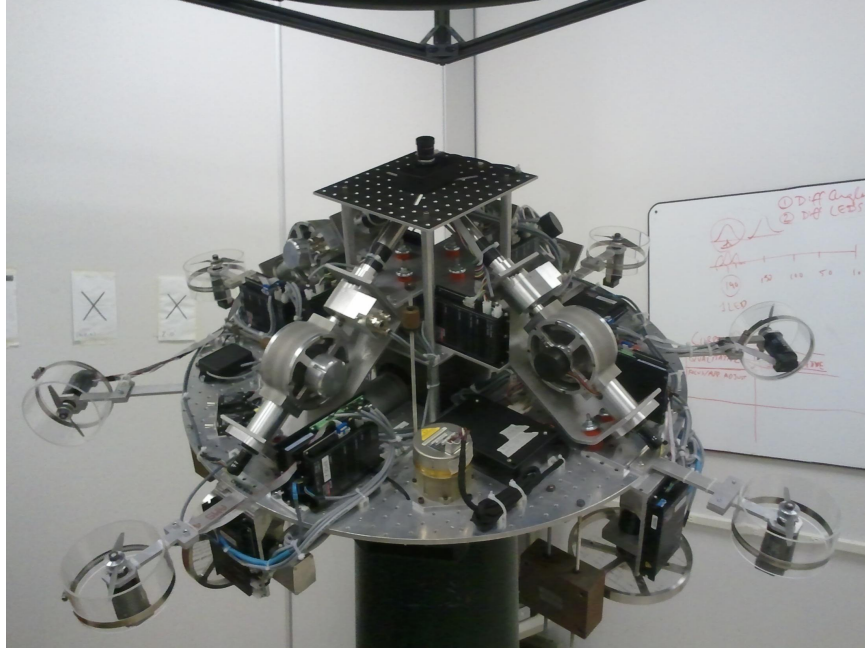


Figure 1: SimSat II Current Configuration

1.2 Problem Statement

The Air Force Institute of Technology's (AFIT's) spacecraft attitude dynamics simulator, SimSat, is used for hardware-in-the-loop validation of new satellite control algorithms. SimSat determines if it is maintaining a commanded attitude by using feedback sensory information from an on-board Inertial Measurement Unit (IMU), which is prone to gyroscopic precession resulting in loss of accurate attitude information. To provide external estimation of attitude information necessary to test the latest satellite control algorithms, SimSat needs an additional attitude reference system of a different form. While several options for reference systems were considered, a star tracker-based system providing an external reference was implemented to meet this need for a laboratory-scaled configuration.

1.3 Research Objectives

The objectives of this research effort are to investigate the critical parameters for a lab-scale star-tracker based external reference system for AFIT's SimSat, integrate a working concept of it within the current SimSat laboratory, and characterize the performance of the concept system through initial validation testing against key algorithmic requirements later identified in Section 3.2. The overall goal of this research effort is to provide SimSat with a preliminary working concept of a unique star tracker-based external reference system to act as an initial point for subsequent research towards a precise, accurate, and robust final solution.

1.4 Methodology

The research methodology was designed to parallel the analysis of space-rated star trackers as much as possible. Preliminary research focused on the key operational requirements of star trackers. The star tracker sensor and optics configuration was narrowed to an industrial Machine-Vision camera. Next, the study and development of the representative star field was composed of two portions: the star-emulation method and the star field surface method. light emitting diode (LED)s where chosen as the star-representative hardware, which was analyzed with regards to their performance when coupled with the selected camera hardware. A final physical configuration was then conceptualized and analyzed for the LEDs. The star field surface was selected to be spherical based on lessons learned from previous research as well as additional surface analysis conducted in this research effort. Both portions were tested via on-board star tracker image collection tests to validate the conceptual approaches discussed in this research. Finally, the pattern recognition and attitude determination algorithms required to validate the complete concept system were coded into MATLAB[®] and executed during subsequent SimSat testing to produce estimated attitude solutions

compared against SimSat's existing attitude sensor. The Angle method for star pattern recognition and the Quaternion Estimation (QUEST) algorithm for attitude determination were utilized in this research.

1.5 Preview

Chapter II consists of a literature review of related topics used in this research, including spacecraft attitude determination, spacecraft dynamics, star tracker operation, star pattern recognition and attitude determination algorithms, and contemporary examples of laboratory star tracker testing and spacecraft simulators. The analysis, design, integration, and testing of the concept reference system is covered in Chapter III. Chapter IV presents the results and analysis of the validation testing performed on the external reference system using SimSat. Finally, Chapter V presents the conclusions of this research and recommendations for future work.

II. Background

2.1 *Spacecraft Attitude Determination*

Spacecraft attitude determination may be separated into two phases: Attitude Knowledge Acquisition, where spacecraft attitude is determined given little or no *a priori* attitude-related information, and Normal Mode Attitude Determination, where updates and refinements of existing attitude estimates are made. The first phase occurs at the beginning of the mission or after a fault results in lost or unreliable attitude data. The second phase occurs routinely throughout the mission (14). Many different devices exist for modern spacecraft that are capable of estimating the vehicle's attitude with varying degrees of reliability, accuracy, and computational efficiency. Sun and moon sensors can be used for attitude determination, but either body must be in view of the spacecraft. Earth-pointing spacecraft can use horizon sensors to determine their attitude, at the cost of being limited to a geosynchronous orbit or lower (25). Magnetometers, which measure Earth's magnetic field, can similarly be used. While indispensable in many applications, however, sun sensors and magnetometers suffer from relatively poor accuracy (maximum of 0.1 degrees) (22).

There is a general consensus in the literature that star trackers, sometimes known as star sensors or star cameras, are the most accurate instruments for spacecraft attitude determination (7). Star trackers are photodetector-based devices that collect images of stars and report the imaged star's vehicle-referenced direction vector and magnitude information. This information is then processed, either on-board or remotely, to determine the orientation of the spacecraft relative to an inertial reference frame. Two reference points are needed, in general, to fully determine the attitude of a spacecraft (25). Indeed, with a continuum of stars populating the celestial sky, numerous stars are always within view of a spacecraft at any given time, providing for multiple direction vectors (and thus, reference points). Furthermore, unlike special-

ized sensors for the sun, moon, and horizon, this also allows for a source of attitude information relatively independent of the spacecraft’s current orientation (14). Figure 2 illustrates the basic principle of star tracker utilization, where \mathbf{A} is the attitude solution determined after processing the star tracker-collected imagery.

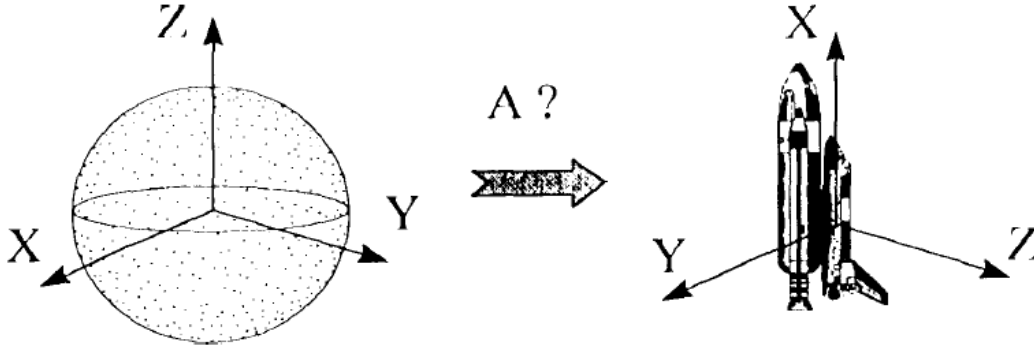


Figure 2: Relation Between the Celestial Sphere and a Spacecraft Reference Frame (7)

Although a variety of attitude determination methods have been developed over the years, they all follow the same basic process (20). Figure 3 shows the flow of a typical image-based star tracker attitude determination process. Attitude determination begins with algorithms that capture and process star pattern images in order to calculate star tracker-framed vectors to the locations of observed stars. Once these vectors are computed, a star pattern recognition algorithm will find the matching inertial-frame vectors from a database, or catalog, of stars to the input star tracker vectors. Later, the attitude determination algorithm calculates a transformation that maps the tracked vectors to the inertial-frame vectors, at which point the spacecraft’s attitude can be determined. Star pattern recognition is also known as “Star-ID” (20).

In a parallel to the two generalized attitude determination phases discussed earlier in this section, all star tracker-related algorithms fall into two categories: Lost in Space (LIS), in which no *a priori* spacecraft attitude information is available, and recursive, in which some attitude information is known. A common property of these

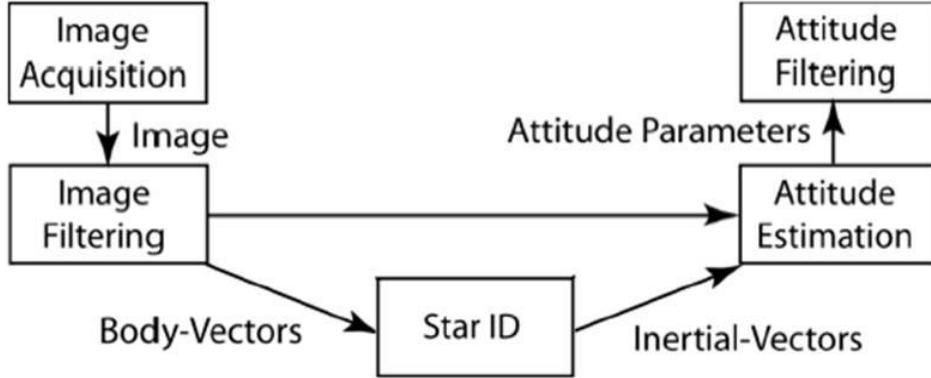


Figure 3: Typical Attitude Determination Process Flowchart (20)

algorithms is the extraction of specific features and parameters from each image. In many cases, these are the inter-star angles, or the interior angle between the position vectors of two imaged stars in the camera’s reference frame, and star brightnesses to distinguish between stars within a pattern.

A subcategory of both the LIS and recursive categories is the Non-Dimensional algorithm, in which, for example, the precise angular star separations are not needed but instead are normalized so that poor/time-varying camera calibrations are compensated for (20). It has been shown that, for certain non-dimensional algorithms, star pattern recognition and attitude determination can be performed simultaneously (8). Two major decisions are also documented: whether or not to use ordinal, or sorted, star pattern features, such as brightness or distance, as algorithmic constraints (20). The discussion of selected algorithms continues in detail in Section 2.4 and Section 2.5.

2.2 *Spacecraft Dynamics*

2.2.1 Reference Frames. Vector observation is the core mechanism that facilitates attitude determination through star tracking. Vectors to the same objects, measured at different times and from different locations, are compared and filtered. The resulting differences between these vectors forms the information used to determine

the attitude of the spacecraft. Such vector observations are made from vastly different locations and with respect to different coordinate references frames (also known as coordinate frames, or simply shortened to “frames”). The coordinate frames used in this research are the star tracker, body-fixed, and Earth-Centered Inertial (ECI) frames.

The ECI frame is fixed in inertial space and centered on the Earth. Its X-axis is in the vernal equinox direction and aligned with the radial vector from the Sun to the Earth, known also as the “Line of Aries” (5). The Z-axis is aligned with the Earth’s rotation axis and perpendicular to the equatorial plane. The Y-axis completes an orthogonal, right-handed frame. The body-fixed (or shortened to “body”) frame is non-inertial and fixed to the satellite. The body frame is generally located at the center of mass of the vehicle, and the axis are aligned with the vehicle’s principle axis. Figure 4 is an illustration of the ECI frame and the body frame of an orbiting satellite.

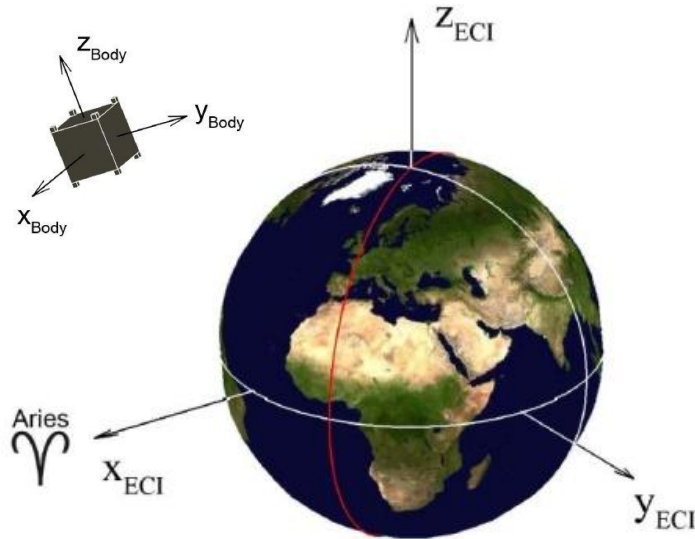


Figure 4: Earth-Centered Inertial and Body-Fixed Frames (20)

All star observations by the star tracker are initially mapped with respect to the star tracker reference frame. The star tracker frame is a three-axis, orthogonal system. Typically, two of the axes are parallel with the horizontal and vertical components of the image plane, and the third axis is aligned with respect to the star tracker boresight. This research uses the the star tracker/image plane coordinate relationship shown in Fig. 5.

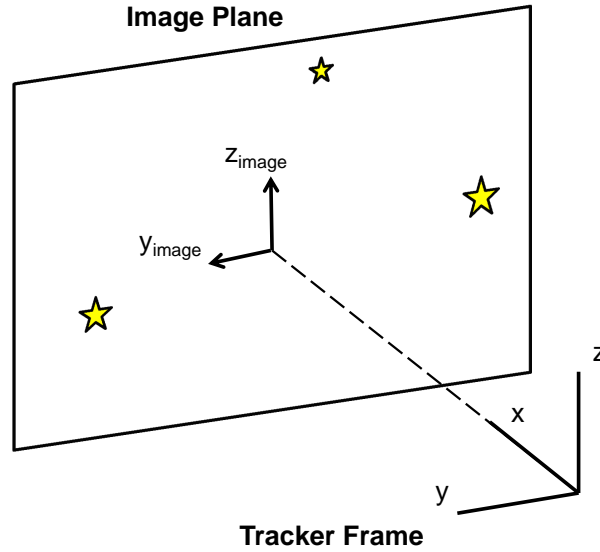


Figure 5: Observed Stars in the Tracker Frame

2.2.2 Rotation Matrices. Vector observations of stars made from Earth are typically measured with respect to the ECI frame, then stored in a star catalog. To compare the two sets of vector measurements requires that the tracker frame vectors be represented in the ECI frame through application of a rotation matrix \mathbf{R}^{it} , where the superscript it is read as “star tracker frame to inertial frame”. A similar rotation can be performed on the ECI frame into the tracker frame, where this rotation matrix is represented as \mathbf{R}^{ti} . Mapping the vectors from the inertial frame, $\vec{v}^{\{\hat{i}\}}$, to the tracker

frame, $\vec{v}^{\{\hat{s}\}}$, occurs through a vector multiplication in the form of

$$\vec{v}^{\{\hat{t}\}} = \mathbf{R}^{\mathbf{ti}} \vec{v}^{\{\hat{i}\}} \quad (1)$$

There are several sets of parameters from which rotation matrices may be constructed from. The simplest form is through use of Euler Angles, which describe one or more rotations through corresponding angles about specified axes. The 18th century mathematician Leonhard Euler first suggested the use of a sequence of three simple rotations about a set of mutually orthogonal axes to describe the orientation of an orbital plane with respect to an inertial frame (21). While various sequences are used and best suited for different applications, this research uses the “3-2-1” sequence, where each number designates the order of the rotation axis. Figure 6 is a sketch of a 3-2-1 rotation from the inertial frame to the tracker frame, where $\{\hat{i}\}$ and $\{\hat{s}\}$ represent the inertial and star tracker frame axis systems, respectively. The intermediate locations of the $\{\hat{i}\}$ frame basis vectors are represented by $\{\hat{i}'\}$ and $\{\hat{i}''\}$. The Euler Angles, θ_n , represent the rotation angle, with their subscripts n designating their order of application.

Each rotation in a sequence is represented by its own rotation matrix. Without derivation, the rotation matrices for a 3-2-1 rotation are

$$\mathbf{R}_3(\theta_1) = \begin{bmatrix} \cos(\theta_1) & -\sin(\theta_1) & 0 \\ \sin(\theta_1) & \cos(\theta_1) & 0 \\ 0 & 0 & 1 \end{bmatrix} \quad (2)$$

$$\mathbf{R}_2(\theta_2) = \begin{bmatrix} \cos(\theta_2) & 0 & \sin(\theta_2) \\ 0 & 1 & 0 \\ -\sin(\theta_2) & 0 & \cos(\theta_2) \end{bmatrix} \quad (3)$$

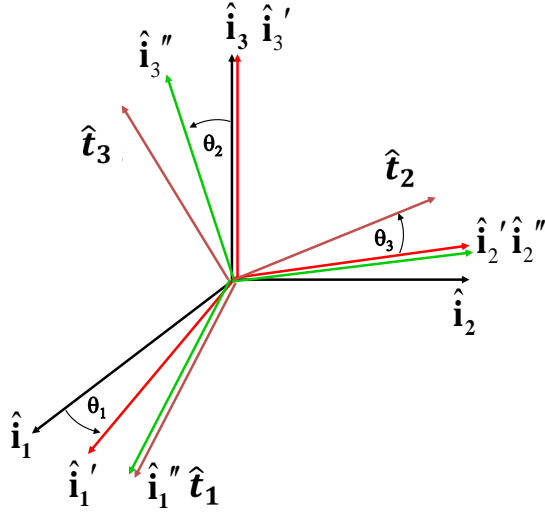


Figure 6: 3-2-1 Rotation Sequence from Inertial to Star Tracker Frame (21)

$$\mathbf{R}_1(\theta_3) = \begin{bmatrix} 1 & 0 & 0 \\ 0 & \cos(\theta_3) & -\sin(\theta_3) \\ 0 & \sin(\theta_3) & \cos(\theta_3) \end{bmatrix} \quad (4)$$

Combining these elementary rotations to form the complete rotation matrix, also known as the direction cosine matrix, involves matrix multiplication from right to left, as in

$$\mathbf{R}^{\text{ti}} = \mathbf{R}_1(\theta_3)\mathbf{R}_2(\theta_2)\mathbf{R}_3(\theta_1) \quad (5)$$

2.2.3 Quaternions. Because direction cosine matrices apply to vector rotations in general, the Euler Angles that compose a direction cosine matrix can be used to describe a spacecraft's attitude. However, the most common way to mathematically represent a spacecraft's orientation is through Euler Parameters, or commonly known

as quaternions. Leonard Euler's 1776 theorem on rigid body motion established the mathematical pretext for quaternions, which summarizes as:

In three-dimensional space, any displacement of a rigid body such that a point on the rigid body remains fixed, is equivalent to a single rotation about a fixed axis that runs through the fixed point (12).

Euler's theorem implies that any rigid body rotation can be described in terms of a rotation angle Φ , known as the Euler angle, about a body-fixed unit vector \hat{e} , known as the Euler axis. This allows for different reference frames to be related by four parameters: three from \hat{e} and one from Φ (21). Figure 7 depicts a rotation about the Euler axis \hat{e} passing through the origin of the reference frame, resulting in pure rotation from position a to position b .

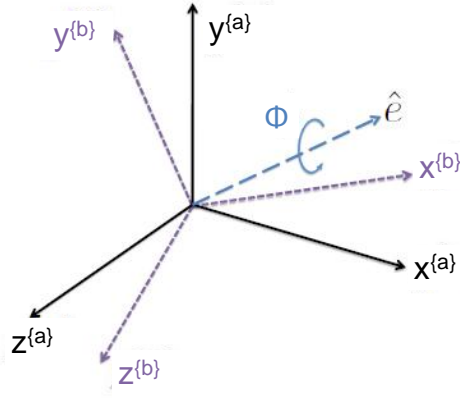


Figure 7: Euler Axis Rotation Relating Frame A to Frame B (12)

With the inherent simplicity of the Euler angle/Euler axis attitude parameterization, there is an obvious singularity when the Euler angle Φ is 0, since the Euler axis is mathematically defined by Φ (21). Similarly, for parameterization using a direction cosine matrix composed of Euler Angles with a 3-2-1 rotation sequence, an odd multiple of $\frac{\pi}{2}$ produces an identity matrix for the 2nd rotation, resulting in singularity. Such singularities cause computational problems. One method to remove the

singularity in computational methods is to use quaternions, defined as

$$\tilde{q} = \begin{bmatrix} \vec{q} \\ q_4 \end{bmatrix} = \begin{bmatrix} e_1 \sin\left(\frac{\Phi}{2}\right) \\ e_2 \sin\left(\frac{\Phi}{2}\right) \\ e_3 \sin\left(\frac{\Phi}{2}\right) \\ \cos\left(\frac{\Phi}{2}\right) \end{bmatrix} \quad (6)$$

The terms q_1 , q_2 , and q_3 are the three components of the quaternion vector \vec{q} . The fourth term, q_4 , is a scalar value, and the complete quaternion is denoted by \tilde{q} . Using quaternions, the difference between any two reference frames or orientations can be described without singularities, even for cases when the two frames are coincident (12). The difference calculation is a matrix multiplication, and results in the second orientation being defined in the first. For example, given quaternions \tilde{a} and \tilde{b} for two orientations defined in reference frame $\{\hat{i}\}$, the difference between \tilde{a} and \tilde{b} defined relative to \tilde{a} is given by

$$\tilde{b}^{\{\tilde{a}\}} = \begin{bmatrix} a_4 & a_3 & -a_2 & -a_1 \\ -a_3 & a_4 & a_1 & -a_2 \\ a_2 & -a_1 & a_4 & -a_3 \\ a_1 & a_2 & a_3 & a_4 \end{bmatrix}^T \begin{bmatrix} b_1 \\ b_2 \\ b_3 \\ b_4 \end{bmatrix} \quad (7)$$

If $\tilde{b}^{\{\tilde{a}\}}$ is $[0 \ 0 \ 0 \ 1]^T$, then \tilde{a} and \tilde{b} are the same. Equation (7) can be used by the spacecraft's attitude control system to calculate the difference between the current orientation and the desired orientation. It can also be used to compare a calculated attitude determination solution to attitude measurements made by other means, including those derived from star catalogs.

2.3 Star Tracker Operation

2.3.1 *Technical Characteristics.* Star trackers are highly sensitive electronic cameras connected to microcomputers, which receive image data of the celestial sphere and, depending on the complexity of the associated computing electronics, outputs usable data in order to finally determine the spacecraft's attitude. Modern star trackers are typically fully autonomous, which minimizes or eliminates interfacing with external subsystems, thus allowing for the solution of the LIS problem. This means the star tracker can automatically perform star pattern recognition and determine the spacecraft's attitude independently (10). Figure 8 is a component sketch of a modern star tracker.

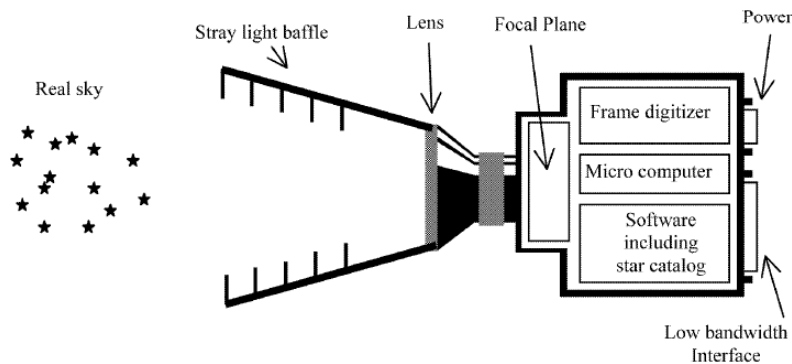


Figure 8: Star Tracker Operational Sketch (10)

Star trackers are grouped primarily according to sensor type and/or “generation” in the literature. The first star trackers developed for spacecraft in the 1950s and 1960s primarily used photomultiplier or photo-diode sensors, and were capable of field of view (FOV) of up to 35 degrees, sensitivity to stars of magnitudes up to 5.7, and pointing accuracies in the range of 120 to 10 arcseconds (18). Tracking stability, temperature, sensitivity to magnetic fields, and high voltage requirements led to the development of the first Charge-Coupled Device (CCDs) in the 1970s. These solid-state sensors provided increased image resolution, dimensional stability, photo-

metric linearity, improved sensitivity near magnitude 7, and accuracy to less than 10 arcseconds (18). Active Pixel Sensor (APSs), which are based on complimentary metal-oxide semiconductor (CMOS) technology, are the latest photodetector type to find application in star trackers. Seen as the successor to CCD, APS detectors demonstrate several advantages over CCD sensors, mainly in lower power operation, on-chip analog-to-digital integration, lower direct processing costs, anti-blooming, and direct access to individual pixels, or “windowing” (4). Pointing accuracies of less than one arcsecond are claimed by the literature (7, 18).

Star trackers categorized by generation are so grouped according to a list of ever-advancing specifications and capabilities. The sensor type is typically included as a secondary distinguisher. As an example, sample star trackers may be categorized as “First Generation Pre-CCD” as Smith does, or “Second-Generation CCD” as Eisenman *et al.* do (7). Although there are some differences in the literature as to what classifies a star tracker as first, second, or third-generation, the single most common differentiator is the ability to operate autonomously. As an example, Eisenman *et al.* (7) write on the differences between first and second-generation star trackers:

- Star constellation pattern recognition is performed autonomously utilizing internal catalogs. The solution of the LIS problem is inherent and no external processing nor additional attitude knowledge is needed for celestial pointing reference determination
- Utilization of a large number of stars in the range of 25 to 85 in the FOV is done for each data frame. Attitude determination from internal catalogs of over 25,000 stars is based on a signal which is effectively larger than in first-generation units. This significantly improves acquisition probabilities and accuracy over the whole sky.
- All compensations, including light time effects, as they apply, are performed internally.
- Attitude quaternions referenced to inertial space are output directly without the intervention of external processing (7).

It was in the 1990's when powerful microprocessors (> 10 MIPS) and large on-board memory allowed second-generation star trackers to become the recognized state-of-the-art (7). Being completely stand-alone, these units were characterized as smaller, lighter, and less taxing on vehicle interfaces and power, among other parametric improvements. Only in recent years have mentions of third and fourth-generation star trackers been observed in the literature. While fully-autonomous operation is still emphasized, improvements in key specifications seems to be the qualifying metric for this generation of star trackers. Star trackers with multiple sensors or FOVs have been developed to mitigate boresight twist angle errors and enhance sky coverage (9).

Star tracker performance is dependent on starlight sensitivity, FOV, the internal star catalog, and star tracker calibration (10, 7). The known sensitivity of the star tracker sensor, commonly referred to as the Quantum Efficiency (QE), affects the range of star brightness values the sensor can accurately detect. The QE is the fraction of the photons converted into photoelectrons on the focal plane of the image sensor (10). Converting this data to the measured photoelectrons captured per exposure, a conversion can then be computed to translate this value to the star magnitude values stored within the star catalog (10). Next, calculation of a star detection threshold, which is the minimum pixel value the star tracker is set to recognize as a star, is set to avoid any background noise from collected images. Additional star tracker characteristics are summarized by Eisenman *et al.* (7):

FOV

The FOV is arguably the most critical star tracker parameter, and ranges from a few degrees to 30 degrees diagonally. When the FOV is narrowed, the angular resolution of a single pixel improves, which results in an increase in pitch and yaw accuracy. However, even with a narrower FOV, it is always desirable to detect a given average number of stars in the FOV, so the lens aperture must increase in

order to allow the star tracker to see fainter stars as compensation. This tends to increase the mass of the star tracker, due to the increasing optics length. Consequently, tracking increasingly fainter stars requires an increasingly larger star catalog, thereby increasing the complexity of the star pattern recognition algorithm.

According to Liebe (10), assuming that the FOV is circular and FOV degrees wide, then the fraction of the sky covered by the FOV is

$$C_{FOV} = \frac{1 - \cos(FOV/2)}{2} \quad (8)$$

Sky Coverage

Sky coverage is the percentage of the sky over which the star tracker can effectively acquire and track stars. Higher-sensitivity devices will detect more stars in the sky, thus encountering less regions in the sky where “black-outs”, or lack of detectable stars, are present.

Mass

The mass of star trackers varies from less than 1 kg to 20 kg. Processing electronics and optics dominate the mass specification of a star tracker.

Star Catalog Size

The size of the star catalog is dependent on the sensitivity of the system. A larger star catalog is required for a sensitive system (large aperture, long exposure time, etc). Resource requirements, such as memory and processing power, increase with increasing catalog sizes. Therefore, it is undesirable to have large catalogs.

Processor Requirements

Processor requirements are directly related to the extent of onboard data processing occurring within the star tracker. Update rates for autonomous star

trackers are on the order of 1-30 Hz, with required processors in the 10 to 15 MIPS range. Prior-leading examples of second-generation star trackers were capable of tracking stars and performing pattern recognition in less than two seconds.

Analog-to-Digital Converter (ADC) Resolution

With large spans in brightness between the dimmest and brightest stars detected, it is usually desirable to utilize higher-resolution ADCs to preserve information. However, if employing a large number of stars (~ 50) in the star image, the number of stars requiring a 12-bit ADC is small. Therefore, the few very bright stars may be discarded, and an 8-bit ADC can be used, which carries a large computational advantage.

Update Rate

Update rate is the rate at which the spacecraft's attitude control subsystem receives the newest attitude information from the star tracker processor. Two factors affect the update rate: exposure time and processing time for the image. Longer exposure times drive better signal-to-noise ratios, but attitude control subsystems are reliant on how well (and quickly) the determined attitude can be extrapolated to a certain time. Therefore, accuracy and exposure time become trade-offs. In star trackers with large star catalogs and complex computations, computation time becomes a major factor. Finally, for rotating spacecraft, it is necessary for exposure time to be limited to avoid smearing the imaged stars across a large track, effectively losing sensitivity and accuracy.

2.3.2 Accuracy. The topic of star tracker accuracy has placed much focus on understanding the sources, effects, and mitigation of measurement errors inherent to star trackers. There are several classification schemes of star tracker error used

by leading researchers, each with specific areas of focus and levels of complexity. Smith’s approach to star tracker distortion estimation and correction is closer to that of an end-user. As such, the application of the pinhole camera model and the “black-box” star tracker assumption allowed for the utilization of a simplified scheme of three error classes: distortion, centroiding error, and noise (18). Eisenman and Liebe, whose research is centered on building star trackers, lists line of sight (LOS) uncertainty, optics error, centroiding error, noise equivalent angle (NEA), and algorithmic errors as error classes (6). All discussions regarding accuracy in this paper will be with regards to Eisenman *et al.*’s broader categorization scheme, described as (7, 6, 18):

FOV LOS uncertainty

Consists of thermal drift, ground calibration residuals, launch effects and gravity release effects. The initial value is measured in a laboratory using precisely-referenced, simulated stars. The LOS is the most difficult uncertainty to measure.

NEA

The NEA represents the star tracker’s ability to reproduce the same attitude when presented with the same star image, and therefore represents the inherent noise in the unit vectors measured by a star tracker. A noiseless, stationary star tracker would repeatedly measure the same exact unit vector to a star at all times. Since real star trackers exhibit inherent noise, a star tracker will measure a multitude of unit vectors distributed over the true direction. The angular width of this distribution of vectors is the angular equivalent of the system noise, or NEA. The NEA is nonsystematic (random).

Optics errors

Optics errors refer to the systematic distortions of the image, including ground calibration errors, optical distortions, thermal distortions, chromatic variations,

and point spread function variations over the focal plane. Common effects are distortion or warping of the sensor plane, which can cause misalignments between the measured unit vectors and the cataloged vectors.

Centroiding errors

Centroiding introduces errors due to non uniformity in pixel light sensitivity, quantization error, uncertainty in the centroiding algorithm, and CCD charge transfer efficiency (CTE). Although defocussing the star images is advantageous when determining the centroid of an imaged star, spreading the star over too great of an area will decrease the signal to noise ratio; therefore, a point spread function of a few pixels is typically chosen (7).

Algorithmic errors

Include time stamp, thresholding, star catalog uncertainties, erroneous star matches, and algorithmic approximations.

The last four components (NEA, optics errors, centroiding errors, and algorithmic errors) are considered the relative accuracy, or the star tracker accuracy, and is a measure of how well the star tracker can accurately detect changes in attitude. This is typically measured in static ground tests utilizing the real sky and the Earth's rotation (6). Given all the sources of star tracker error, the fundamental limit of star tracker pointing accuracy is the positional accuracy of the star catalogs to which tracker measurements are compared. The HIPPARCOS satellite recorded the positions and brightness of the 120,000 brightest stars with a positional accuracy of 1 milliarcsecond. This is small compared to the roughly 1 arcsecond accuracies achievable by star trackers, so the uncertainties associated with a star's cataloged true position is negligible (7).

2.3.3 *Ideal Pinhole Camera.* The optical theory of star trackers is similar to that of cameras and astronomical telescopes (18). However, the analysis of star tracker operation typically begins with a simplifying assumption that star trackers behave like an idealized pinhole camera, where rays of light from point-sources travel in straight lines and pass through the pinhole and onto the sensor focal plane (17). This assumption neglects any diffraction effects that may occur due to the onboard optics of the star tracker. Figure 9 illustrates the pinhole camera. One pair of stars, close to the boresight, is separated by some angle. Another pair, separated by the same angle, is located farther to the side. The camera's X-,Y-,Z- coordinate reference frame is set over the pinhole and behind the pinhole is the projection of the spherical sky onto the focal plane. Note that the effective FOV of the camera is depicted as being quite large.

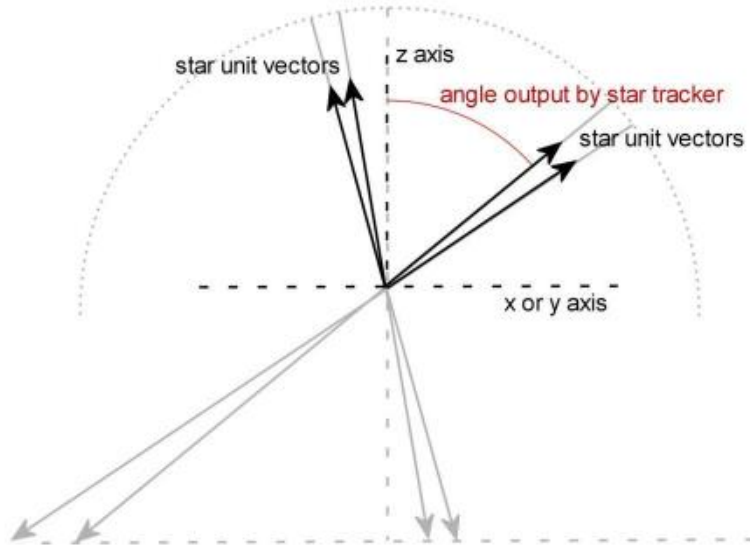


Figure 9: Ideal Pinhole Camera Assumption (18)

From Fig. 9, projecting the stars from the spherical sky to a flat focal plane results in varying linear separations projected onto the plane (18). However, their angular separations remain consistent with their focal plane projections, as do the

angular positions to every star with respect to the camera reference frame (depicted by the red arc in Fig. 9). Consistency in angular measurement is the key enabler of vector measurements using star trackers. It also allows for placing of the notional focal plane at any distance normal to the boresight away from the pinhole, which improves flexibility of analysis.

2.3.4 Vector Mapping. At the most elementary level, star trackers report the horizontal and vertical (H, V) sensor pixel positions of the star image projected onto the image plane (or, may report angles which are converted to (H, V)). The positions are determined through the process of centroiding, where the centers of the imaged stars are calculated by the internal processors in the star tracker (18). For most star trackers, the star images are slightly defocussed in order to spread each star over several pixels (7, 18). Resolutions as low as 1/100 of a pixel have been achieved (7). Figure 10 shows an image from a prototype star tracker. To the right is a close-up view of one of the stars and the calculated centroid from the star's pixel area.

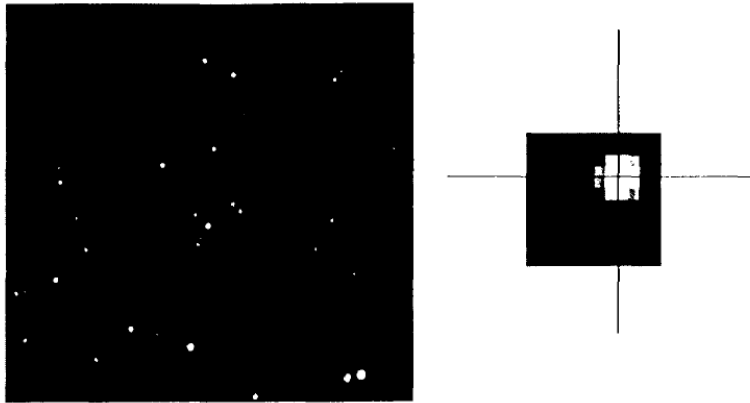


Figure 10: Star Image Centroid Illustration (7)

The tracked stars' (H, V) pixel coordinates are then transformed to a spatial coordinate system with respect to the star tracker frame, which may or may not include any error corrections. The tracked star direction in the celestial sphere with respect to the tracker frame, $\{\hat{t}\}$, can then be computed by using (H, V) and normalizing to unit vectors. If given a star S reported at (H_S, V_S) , then transformed to (y_S, z_S) in the star tracker frame $\{\hat{t}\}$, and considering no further distortion or centroiding error compensations at this point, the tracked star position is

$$\hat{v}_s^{\{\hat{t}\}} = \frac{[1 \ y_S \ z_S]}{\|1 \ y_S \ z_S\|} \quad (9)$$

The angular distance to the boresight (β) is determined by

$$\beta = \arctan \frac{\sqrt{y_S^2 + z_S^2}}{1} \quad (10)$$

Figure 11 illustrates an example with three observed stars in the image and the image plane projected in front of the tracker reference system at a unit distance. The angle β is shown for one of the stars. A star at (y_0, z_0) would map onto the tracker boresight, and thus on the tracker frame x-axis.

2.4 Star Pattern Recognition Algorithm

2.4.1 Overview. With the necessary star vectors mapped in the star tracker frame and the accompanying tracked star magnitude information stored, the next step is to correlate this information to the cataloged data stored on board the spacecraft. This is especially critical for the LIS case, since star pattern recognition is the common method applied to solve for this situation (7). There are three steps regarding Star-ID, with an optional fourth. Figure 12 shows the process for the typical Star-ID algorithm. First, features, explained in detail in the next paragraph, are extracted

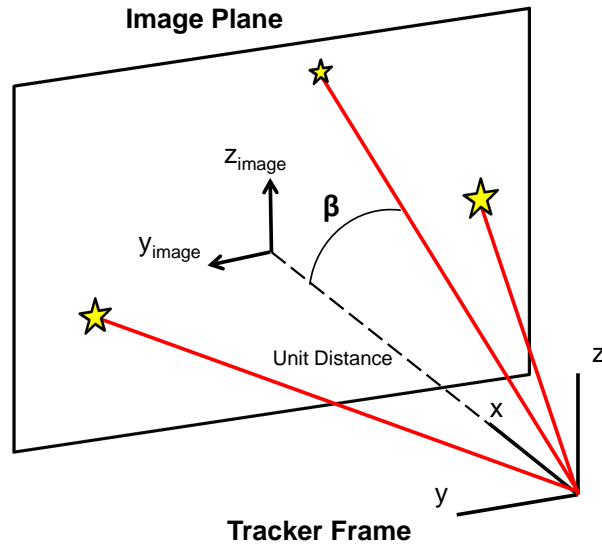


Figure 11: Mapped Star Vectors in the Tracker Frame

from the set of tracked star vectors and their associated brightness. Second, a search of the star catalog matches a subset of the observed information with entries in the database. Third, an estimate is made regarding the probability that the matches are correct. In the optional fourth step, recursive Star-ID may be implemented, where the remaining body-frame vectors are identified using a new estimate of spacecraft attitude. Typically, a variation of the direct match technique is employed in the fourth step in which stars are identified by their close proximity to their predicted location. This recursive fourth step is usually much faster than the first two steps, and may be repeated in succession for additional observations with an *a priori* attitude estimate (20).

The feature extraction step will be discussed in this paragraph, including a sampling of the many algorithms used, such as the angle method, planar triangle method, and spherical triangle method. The angle method is the simplest algorithm. The inter-star angle between star pairs is determined from the mapped vectors in the star tracker frame. Due to the relatively-infinite distances of stars from Earth, the

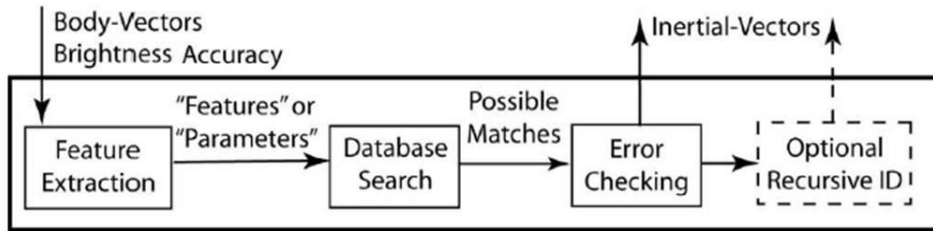


Figure 12: Typical Attitude Determination Algorithm Flowchart (20)

angle between star pairs measured with respect to the ECI frame will be the same as viewed from an Earth-orbiting satellite. While Star-ID using the angle method is simplistic and requires only two stars in the FOV, the inter-star angle is very sensitive to noise. Furthermore, unless star brightness is also considered, the measured angles are the only contributors of uniqueness for the algorithm to match. The algorithm will require stored or readily-computed inter-star angles between catalog vector pairs and suitable matching logic to prevent false identifications (22). Figure 13 shows the angle calculated from a star pair, where the origin is the star tracker reference frame.

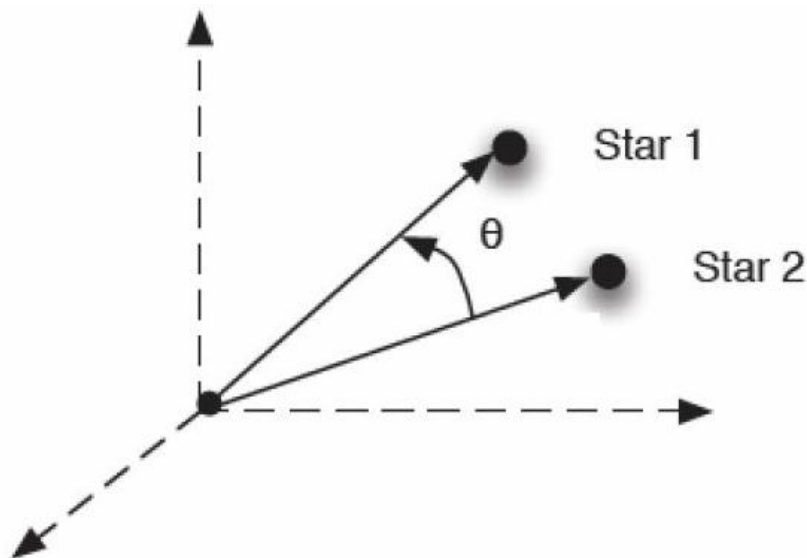


Figure 13: Angle Method (5)

Another Star-ID algorithm is the planar triangles method, as depicted in Fig. 14. In this method, the area and polar moments of triangles formed from three observed stars are calculated, providing more identifying information than a star pair angle alone. As with the angle method, the area and polar moments are invariant with respect to the ECI or star tracker frame. The improved uniqueness reduces the number of false identifications, but with a computational and operational cost. A minimum of three stars is now required in the FOV, additional calculations must be performed, and more memory must be allocated to store the area and polar moments (22). A simplified variation of this method is to calculate the interior angles of the triangle using the Law of Cosines and use these as the Star-ID parameters (5).

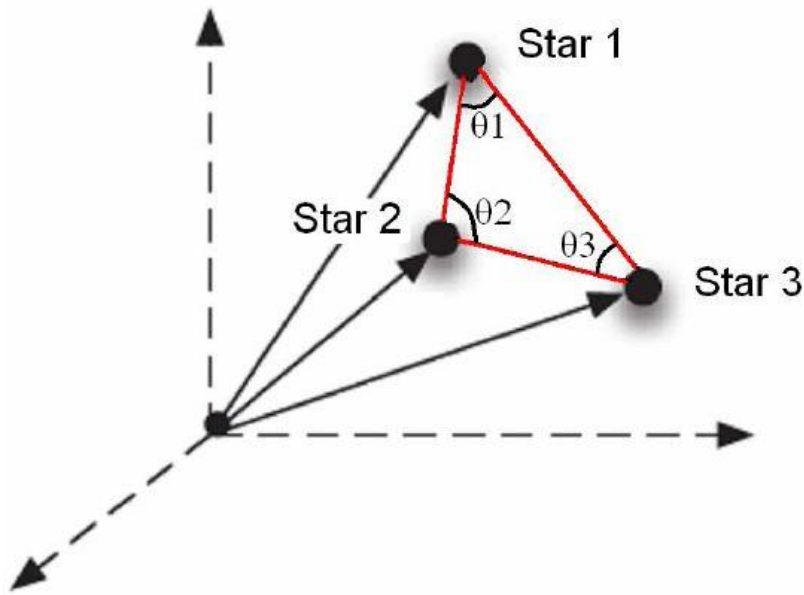


Figure 14: Planar Triangles Method (5)

Similar to the planar triangle method, the area and polar moments of the spherical triangle are calculated, providing even more unique identifiers for each star. Figure 15 illustrates the method. Significant computational complexity is inherent with this method, especially in recursively determining the polar moment of the spherical triangle (22). Such complexities increase the attractiveness of the more straightfor-

ward star pattern recognition methods, specifically the angle method, especially for cases where high accuracies are not required.

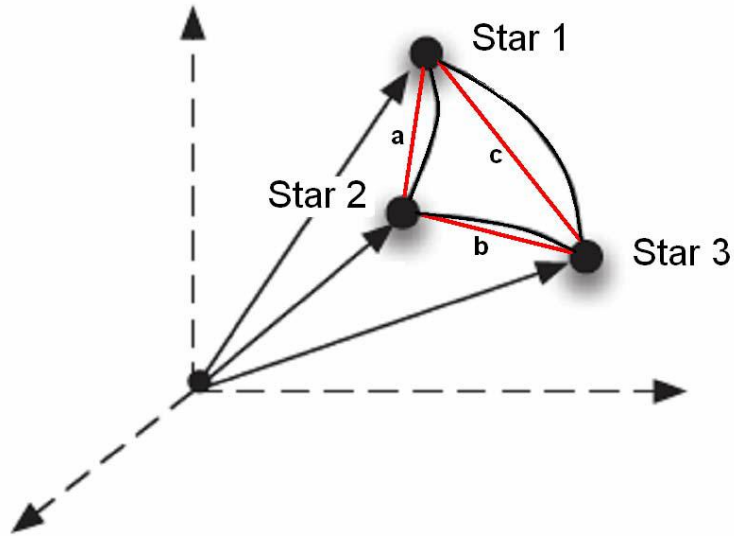


Figure 15: Spherical Triangle Method (5)

2.4.2 Angle Algorithm. After examining various star pattern recognition algorithms based on specific feature extraction methodologies, selecting the most basic of these algorithms facilitates a preliminary study of star pattern recognition and attitude determination. While the star tracker system described in this research is intended for implementation of more advanced algorithms in future research efforts, the star pattern recognition algorithm under investigation in this research is the angle method. Therefore, the LIS “Stellar Attitude Acquisition (SAA)” algorithm presented by Needelman *et al.* (14) was chosen as the basis for the algorithm implemented and analyzed in this research effort. The LIS/SAA algorithm is utilized by Boeing for attitude determination, and fundamentally closest to van Bezooijen’s “Automated Star Pattern Recognition” method (14, 20). Simulations and observatory-based ground testing demonstrated that the algorithm was successful for over 300 tests, with no observed mis-acquisitions (14). This method relies on two catalogs:

- Acquisition Star Catalog (ASC) - This is commonly referred to as the star catalog. Each entry represents a star, containing information on the star's position in the ECI frame and its instrument magnitude. Stars are sorted by their measured real-sky declination.
- Pair Catalog (PC) - Each entry represents a star pair, where each star is represented by ASC entries. The PC is organized into buckets, or contiguous groups of pairs with an angular separation within a specified range. The PC buckets are sorted in order of increasing star pair angular separations.

The generalized Angle algorithm is as follows:

1. *Supply data* - At time t_0 , tracker data (H, V) and magnitudes for all detected stars in the image is acquired and sent to the star tracker processor. A position vector in the tracker frame is generated for each star, as demonstrated in Section 2.3.4 and Eq. (9). Figure 16 illustrates the tracked star data and ASC data at this step. Size represents relative brightness, while colors represent true star correspondence, where correspondence is defined as the relation between a tracked star A and a candidate catalog star C_n . As an example, the five-point yellow star is the largest, and hence the brightest star in the FOV, and in truth corresponds to the large four point yellow star. The small red stars are the dimmest and maintain a similar correspondence. It is assumed that this correspondence has not yet been established for this scenario.
2. *Select primary pair* - A pair of tracked stars, A and B , with corresponding unit vector positions $\hat{a}^{\{t\}}$ and $\hat{b}^{\{t\}}$ are labeled the *primary pair*. The pair is made up of two bright stars with separation angle θ defined as

$$\theta = \arccos(\hat{a}^{\{t\}} \cdot \hat{b}^{\{t\}}) \quad (11)$$

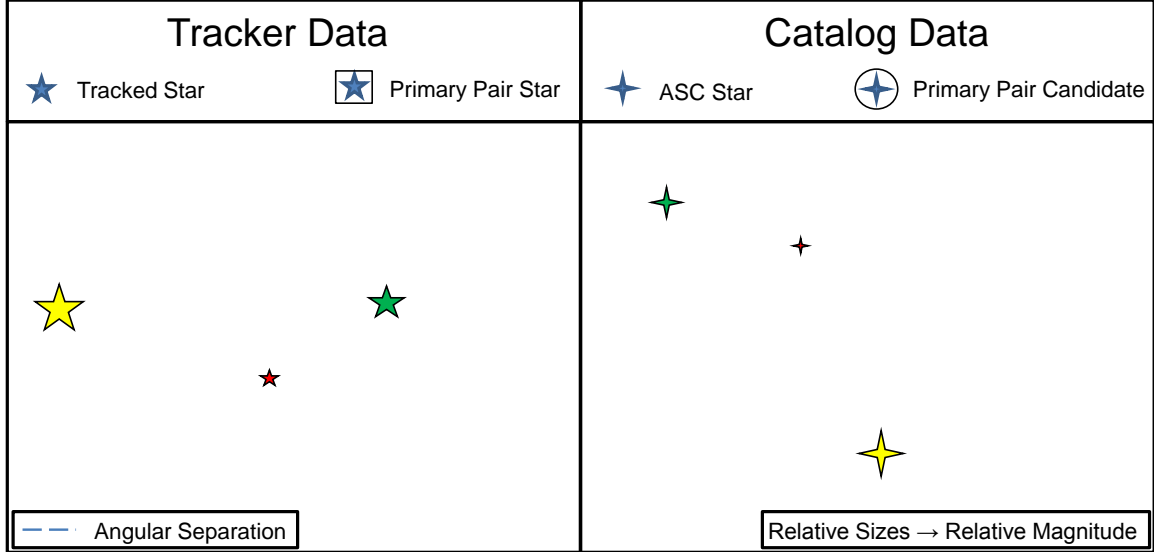


Figure 16: Star Tracker Data

within a specified range. The stars chosen as A and B can have any brightness magnitude, but choosing them to be the brightest stars in the image optimizes the catalog search process (14). A and B will pass the subsequent steps only if they correspond to stars in the ASC, and only if their magnitudes and separation are such that they also correspond to entries in the PC. If these conditions are not met, the $A - B$ pair should fail every test, effectively skipping to Step 8 where A and B are redefined.

3. *Determine primary pair candidates* - Due to measurement error, the actual separation between A and B lies in the range $[\theta - 3\epsilon_{separation}, \theta + 3\epsilon_{separation}]$, where $\epsilon_{separation}$ (discussed in Section 2.4.4) is the 1σ error in the tracked star pair separation measurement. If A and B correspond to stars in the ASC, then, as the PC contains buckets sorted by angular separation, the primary pair will correspond to a PC entry with indices in the range $[j_{min}, j_{max}]$. The PC entries in this range are the *primary pair candidates*. Set the PC index $i \leftarrow j_{min}$, and define primary pair candidates $C_{j1}^{\{i\}}$ and $C_{j2}^{\{i\}}$ as the first and second stars in

the PC entry j . Steps 2 and 3 are demonstrated in Fig. 17, where the hashed straight lines represent the angular separations between the star pairs.

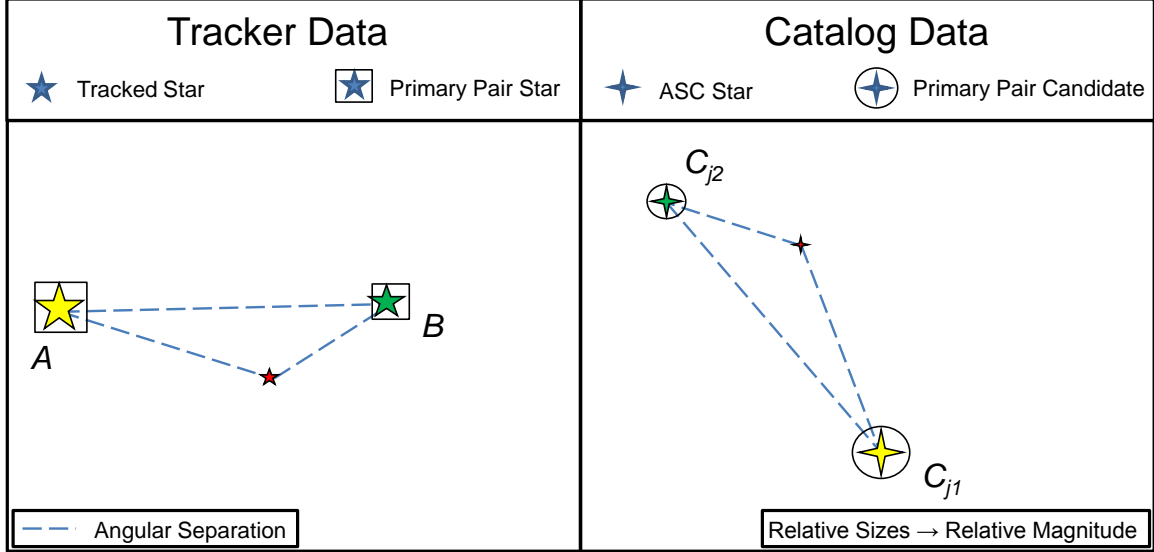


Figure 17: Primary Pair and Candidate Selection

4. *Formulate primary assumption* - Assume that the primary star A corresponds to candidate $C_{j1}^{\{i\}}$, and primary B corresponds to candidate $C_{j2}^{\{i\}}$. This is known as the primary assumption. Reject this assumption and proceed to Step 7 if:
 - (a) The observed magnitude of primary star A or B does not correspond to the cataloged magnitudes of candidate $C_{j1}^{\{i\}}$ or $C_{j2}^{\{i\}}$, to within a specified tolerance, or:
 - (b) (Optionally) If additional attitude information is available (e.g. sun position, rough attitude estimate), and this information is inconsistent with the primary assumption.

This step is depicted in Fig. 18, where the curved lines represent the primary assumption relationships. The erroneous scenario is shown where the wrong star w is chosen as star B and assumed to correspond to candidate $C_{j2}^{\{i\}}$. Since their magnitudes are outside the matching tolerance (they are different sizes in the

figure), Step 4 would discard this relationship and the algorithm would continue at Step 7.

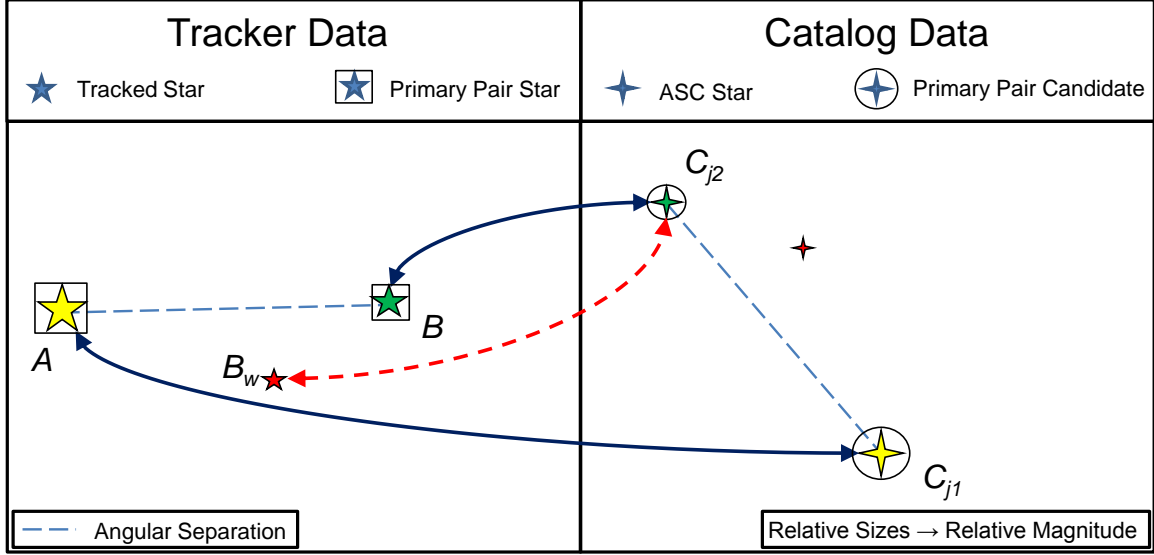


Figure 18: The Primary Assumption

5. *Determine mapping between frames* - Using the corresponding unit vector positions found from Step 1 and an appropriate attitude determination algorithm, find a candidate rotation matrix \mathbf{R}^{it} that maps the primary pair vectors $\hat{a}^{\{\hat{t}\}}$ and $\hat{b}^{\{\hat{t}\}}$ from the tracker frame $\{\hat{t}\}$ into the ECI frame $\{\hat{i}\}$. This should roughly coincide the two candidate star pairs.
6. *Apply Direct Match Test* - Predict which ASC entries represent stars in the tracker FOV at time t_0 given $\mathbf{R}^{\text{it}}(t_0)$. Use the direct match test to evaluate the validity of $\mathbf{R}^{\text{it}}(t_0)$. If $\mathbf{R}^{\text{it}}(t_0)$ is valid, then the algorithm successfully terminates. Otherwise, proceed to the next step.
7. *New Primary Pair Candidate* - Candidate C_{j1} is replaced with the second star in PC entry j , and candidate C_{j2} with the first. Return to Step 4. If the switch has been previously made, then $j \leftarrow j + 1$, and:

- (a) If $j \leq j_{max}$, then candidate C_{j1} becomes the the first star in PC entry j , candidate C_{j2} becomes the second star in that entry, and the algorithm returns to step 4.
 - (b) Otherwise, if $j > j_{max}$, proceed to next step.
8. *New primary pair* - The primary pair candidates list has been exhausted. Select a new primary pair if there exists another pair of tracked stars meeting the angular separation and magnitude criteria. If not, terminate the algorithm unsuccessfully. Otherwise, re-define primary stars A and B , and their corresponding angular separation θ , then return to step 3.

2.4.3 Mapping. Step 5 requires a mapping from the star tracker frame to the ECI frame, which is based on the primary assumption. The primary assumption is that two points in the tracker reference frame, the positions $\hat{a}^{\{t\}}$ and $\hat{b}^{\{t\}}$ at time t_0 of the primary pair stars A and B , approximately correspond to equivalent ECI frame positions of the primary star candidate stars (PC entry j , candidates C_{j1} and C_{j2}). The correspondence will generally not be exact, since the angular separations of the two frame pairs will not be exactly equal due to star tracker position-reporting error.

With the primary assumption established, various methods for spacecraft attitude determination may be used to calculate the estimated mapping from the star tracker frame to the ECI frame, $\mathbf{R}^{it}(t_0)$. Section 2.5 discusses selected attitude determination algorithms.

2.4.4 Error Estimation. Errors in the calculation of spacecraft attitude (Step 5), calculation of tracked star positions via the direct match test (Step 6), and star separations (Steps 3 and 6) will occur due to tracker and star catalog position-reporting error. These errors correspond to approximately 5 arc-sec, 1σ , and $1/3$ arc-sec, 1σ , respectively (14). The tracker-related errors far outweigh the star catalog errors. The

two key scalars $\epsilon_{position}(S)$ and $\epsilon_{separation}$, may be derived from the attitude estimate given by the attitude determination algorithm:

- $(\epsilon_{position}(S))^2$ - The square of the error (1σ) in the estimated ECI-referenced position of a tracked star, S , where the estimate is formulated using $\mathbf{R}^{it}(t_0)$ (14).
- $(\epsilon_{separation})^2$ - The square of the error (1σ) in the estimated separation of a tracked star pair, where the estimate is based on the tracker-reported star positions.

2.4.5 The Direct Match Test. In step 6, the direct match test is applied to validate, or invalidate, the mapping estimate $\mathbf{R}^{it}(t_0)$. If the estimate is valid, there should be a correspondence between the tracked stars and the ASC stars predicted to lie in the tracker FOV. The direct match test determines whether the tracked stars match the ASC stars by comparing the tracked stars' positions and magnitudes with those of specific ASC entries. The test is not applied to primary stars A and B , which is assumed to already match to candidate stars C_{j1} and C_{j2} according to step 4 (14). The primary assumption is confirmed and the algorithm successfully terminates if a threshold number of tracked stars pass the test.

To pass the direct match test, four conditions must be met to establish that tracked star X corresponds to ASC entry n . The first three conditions are depicted in Fig. 19, where the two frames from Fig. 18 are superimposed, and the ASC star vectors were rotated by the inverse of the rotation matrix found in Step 5. The stars from the two sets of data are shown in a single frame for visual comparison in this example.

1. *Magnitude match* - the reported instrument magnitude of X must match the catalog-listed magnitude of n to within a specified value, Δm (14).

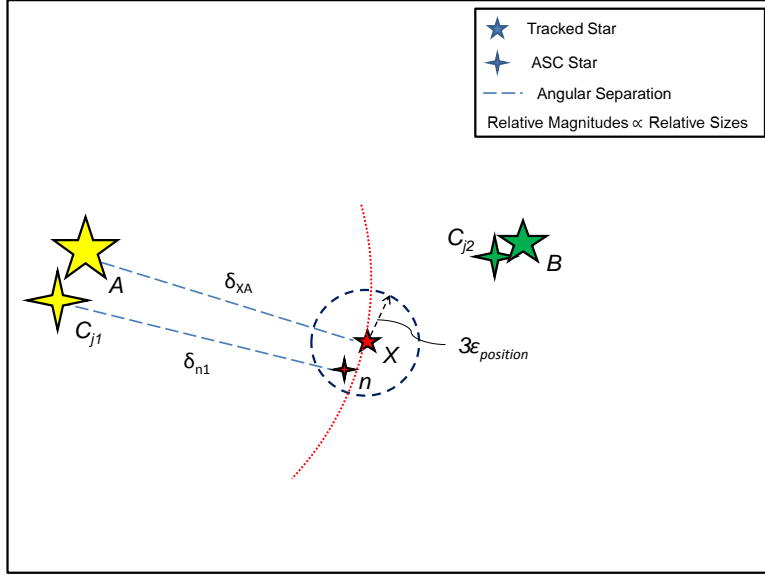


Figure 19: The Direct Match Test - Correct Mapping

2. *Position match* - using the inverse (transpose) of $\mathbf{R}^{\text{it}}(t_0)$, map the position vector of ASC entry n 's with respect to the ECI frame into the star tracker frame. The predicted position of ASC entry n must now match the observed position of tracked star X in the tracker frame to within a specified value, $3\epsilon_{\text{position}}(X)$. The specified threshold is the expected error in (3σ) . This is seen from Fig. 19, where the predicted position must fall within the blue dashed circle.
3. *Separation match (A - C_{j1})* - The observed angular separation between tracked stars X and A , δ_{XA} , must match δ_{n1} , the separation angle derived from the cataloged positions of ASC entries n and candidate C_{j1} to within a specified value, $3\epsilon_{\text{separation}}$. In other words, the predicted position of n in the tracker frame must fall on, or near, the red dotted arc in Figure 19.
4. *Separation match (B - C_{j2})* - Similarly, the observed angular separation between tracked stars X and B , δ_{XB} , must match δ_{n2} , the separation angle derived from the cataloged positions of ASC entries n and candidate C_{j2} to within a specified value, $3\epsilon_{\text{separation}}$.

The overlap between conditions 2 through 4 serves to test the proposed match based on the position of the mapping of ASC entry n in the tracker frame. Conditions 3 and 4 are strong constraints, although given the accuracy of present-day trackers, are difficult requirements to satisfy for stars that fail to correspond. They allow the mistaking of an observed star triangle made up of the primary star pair and a third tracked star, for a completely incorrect triangle that happens to be a mirror image of the desired one (14). A similar case is illustrated in Fig. 20, where an incorrect rotation matrix has mapped the primary pair and primary pair candidates to virtually coinciding positions. Assuming that the magnitudes of the primary pair and primary pair candidates are indistinguishable, and allowing that δ_{XA} is nearly identical to δ_{n1} , star n is still clearly outside the (3ϵ) radius imposed by Condition 2. This result would be rejected by the algorithm, and the algorithm would continue.

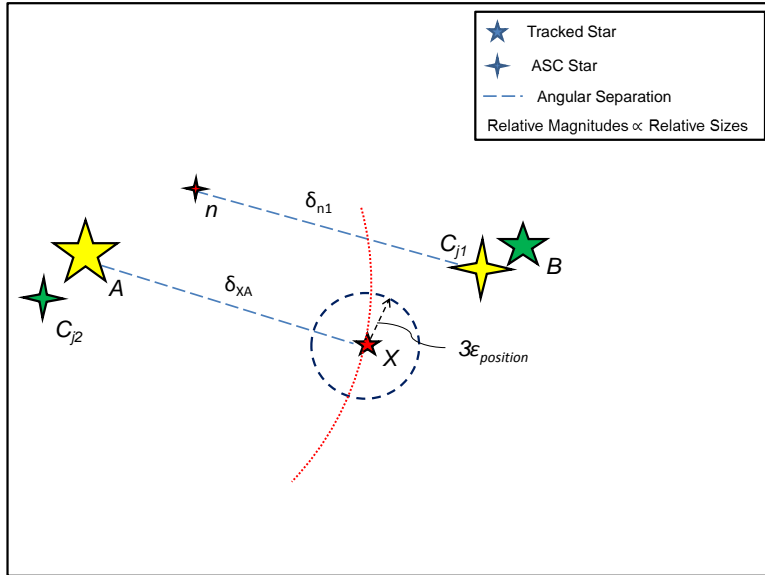


Figure 20: The Direct Match Test - Incorrect Mapping

2.4.6 Star and Pair Catalogs. The primary information stored for each entry in the ASC representing a star is the position vector with respect to the ECI and the instrument magnitude, or star magnitude, as reported by the star tracker (14).

Entries in the ASC are sorted by real-sky declination and only reference stars with magnitude less than (brighter than) m_{min}^{ASC} , where m_{min}^{ASC} is brighter than the dimmest star detectable by the tracker. Each entry in the PC represents a star pair and contains the locations of the two ASC entries of the stars forming the PC pair. The PC entries are grouped according to specified ranges of angular separation, while the pairs within these groups remain unsorted. The PC contains every ASC star pair such that the stars forming the pair have a separation in a specified range, and both of the stars forming the pair have an instrument magnitude in a specified range (14). The Boeing star catalog architecture is shown in Fig. 21.

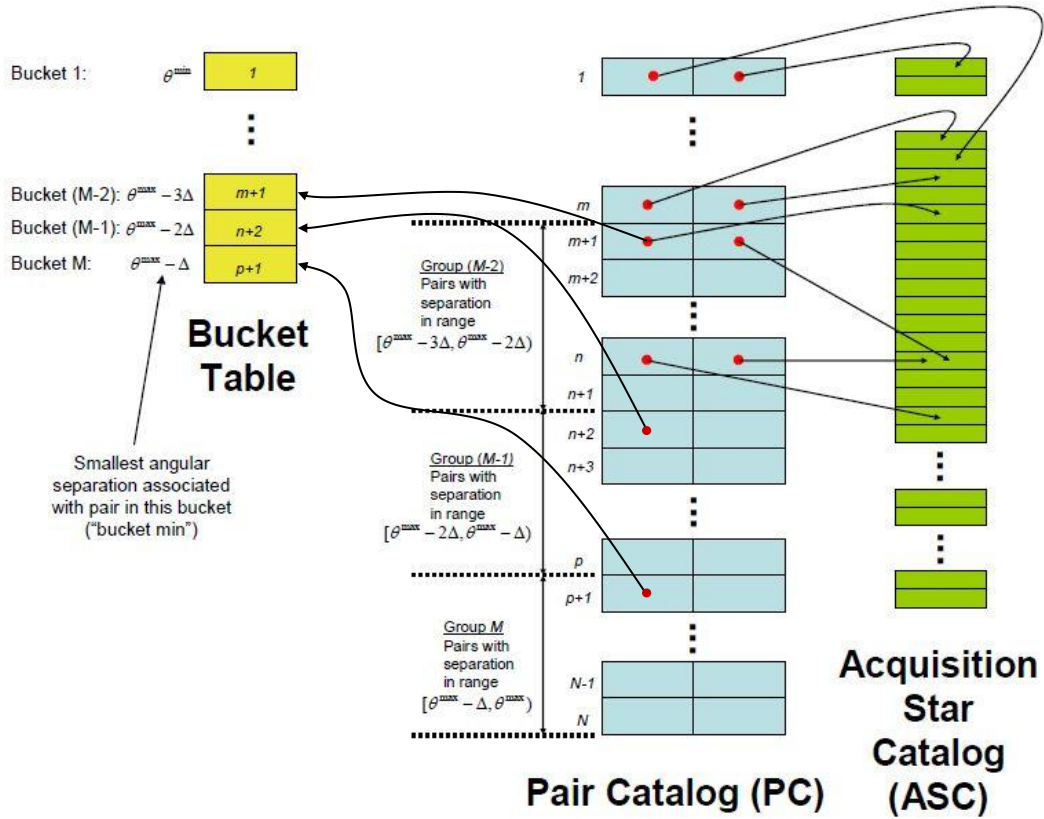


Figure 21: Boeing Star Catalog Architecture (14)

It is critical to note that the ASC stores all star-pattern related features. The PC is simply a lookup table of locations in the ASC that correspond to the candidate catalog matches to the observed stars, effectively paring down the total number of searches within the ASC, and therefore cutting search time. The PC is divided into entry groups, or buckets, with each bucket containing one or more entries addressing star pairs with angular separation in a specified range $[bucket_{min}, bucket_{max}]$. The PC is backward-indexed, since it is constructed with respect to the largest angular separation in the ASC. The buckets are sorted in order of increasing angular separation, such that the first bucket contains the ASC locations of the star pairs with the smallest angular separations. Conversely, the last bucket contains the ASC locations of the star pairs with the largest angular separations.

The bucket table provides the bucket locations in the PC to specific star pairs, where the i^{th} entry in the bucket table represents the start location of the i^{th} bucket in the PC. For an ASC with N star pairs, the N^{th} star pair is addressed to the last star pair entry in the last PC bucket, which also corresponds to the star pair with the largest separation angle in the attitude control system (ACS). Bucket sizes Δ , or the number of star pairs addressed in each bucket, may vary, and are effectively the PC's resolution; a larger Δ will result in less candidate pairs to process through, while the inverse is true for a smaller Δ . The system depicted in Fig. 21 assumes a constant bucket size Δ , where Δ is in arcseconds (14).

Determining the primary pair candidates corresponding to a primary pair (Step 3) should be straightforward with this architecture. In this step, the primary pair candidates with angular separation in the range $[\theta - 3\epsilon_{separation}, \theta + 3\epsilon_{separation}]$ are found. An example to illustrate the use of the architecture is summarized from Needelman *et al.* below:

Let the maximum separation angle in the PC be represented as θ_{max} , and assume that the angle in question is exactly $\theta = (\theta_{max} - 1.7\Delta)$ where θ can be defined by constant bucket size Δ for illustration purposes. Also, let the calculated separation angle error $\epsilon_{separation} = 0.2\Delta$. For this case, pair candidates will lie in the range $[(\theta_{max} - 1.7\Delta) - 3(0.2\Delta), (\theta_{max} - 1.7\Delta) + 3(0.2\Delta)]$, or

$$PC_{Range} = [\theta_{max} - 2.3\Delta, \theta_{max} - 1.1\Delta] \quad (12)$$

Referring to the bucket table on the left side of Fig. 21:

- The bucket with the largest $bucket_{min}$ smaller than $(\theta_{max} - 2.3\Delta)$; this is bucket (M-2), with a bucket min of $(\theta_{max} - 3\Delta)$.
- The bucket with the smallest $bucket_{min}$ larger than $(\theta_{max} - 1.1\Delta)$; this is bucket (M), with a bucket min of $(\theta_{max} - \Delta)$.

The viable pair candidates will therefore be in the contiguous region beginning with the first entry in group (M-2), and ending immediately before the first entry in group M. Looking at the bucket table, group (M-2) begins at PC location (m+1), and group M begins at PC location (p+1). Therefore, the pair candidates of interest correspond to PC entries (m+1) through (p).

There is some wasted effort in checking pair candidates, since PC entries with angular separations outside the desired range are checked. In the example just given, time was wasted when looking at candidates with angular separations in the ranges $[\theta_{max} - 3\Delta, \theta_{max} - 2.3\Delta]$ and $[\theta_{max} - 1.1\Delta, \theta_{max} - \Delta]$. However, if $\Delta \ll 3\epsilon_{separation}$, the waste is trivial. For example, given a PC with $[\theta_{min}, \theta_{max}] = [1.5^\circ, 8^\circ]$, and a $3\epsilon_{separation}$ of 20 arcseconds, a choice of $\Delta = 5$ arc-sec results in checking about 12.5% extra candidates. The bucket table will contain 4680 integer entries, versus the approxi-

mately 26,000 angles that would have otherwise have been listed in the PC without this architecture (14).

2.4.7 Star Pattern Recognition Algorithm Summary. Numerous star pattern recognition algorithms have been developed since the 1970s, each with various methods and degrees of feature extraction, star database search, and utilization of independent star pattern features (20). While various improvements to pattern recognition effectiveness and efficiency have resulted from these efforts, once the LIS case became solvable from a single real-time image, further efforts turned towards improving the robustness to errors in star detection and feature measurement (20). The angle method represents the most fundamental star pattern recognition algorithm in terms of feature/parameter utilization. The advantages to the Boeing catalog architecture is that it avoids requiring the angular separation to be stored in the PC, slashing memory required for the PC in half, and it avoids the need for a binary search to find pair candidates with the correct angular separation when the LIS is executed (14). An intermediate step in the algorithm is the computation of a suitable rotation matrix using an attitude determination algorithm, which is discussed in the next section.

2.5 Attitude Determination Algorithm

2.5.1 Overview. In Section 2.4, features such as magnitude and separation angle were extracted from vector observations of stars in the tracker frame and compared to those in a reference star catalog. All comparisons were made with respect to the star tracker and ECI frames. However, to set up the spacecraft attitude problem illustrated in Fig. 2, knowledge of the observed star positions with respect to the body-fixed frame $\hat{v}^{\{b\}}$ is necessary. This can be addressed with a rotation matrix, \mathbf{R}^{bt} , composed of the known Euler Angles representing the orientation of the star tracker frame with respect to the body-fixed frame, similar to the demonstration seen

in Section 2.2.2. Star tracker frames may be aligned with the spacecraft body frame, in which case assuming no rotation matrix simplifies the analysis. This case is not assumed here.

Once $\hat{v}^{\{b\}}$ is determined, the attitude determination problem can then be stated in its simplest terms as

$$\mathbf{A}\hat{V}_i = \hat{W}_i \quad (i = 1, \dots, n) \quad (13)$$

where \mathbf{A} is the orthogonal rotation matrix which maps the inertial frame into the body-fixed frame. $\hat{V}_1, \dots, \hat{V}_n$ are the set of reference unit vectors in the ECI frame and $\hat{W}_1, \dots, \hat{W}_n$ are the set of observed unit vectors in the spacecraft body frame. Because of error in both observed and reference unit vectors, an exact solution of A does not generally exist, not even for the case of n equals two (17). Note the change in notation, specific to the attitude determination algorithm, where previous $\hat{v}^{\{b\}} \rightarrow \hat{W}_i$ and $\hat{v}^{\{i\}} \rightarrow \hat{V}_i$. In 1965, Wahba proposed the problem of determining the rotation matrix A that brings the reference vectors \hat{V} into the best least squares coincidence with observed vectors in the satellite body-fixed frame, \hat{W} (24). This is to say, find \mathbf{A} that minimizes

$$\sum_{i=1}^n \|\hat{W}_i - \mathbf{A}\hat{V}_i\|^2 \quad (14)$$

\mathbf{A} then represents the least square estimate, or attitude matrix, of the rotation matrix which maps the inertial frame into the body-fixed frame.

Wahba's problem has been explored and solved through various methods to varying degrees of success, and these methods can generally be classified into two categories: deterministic and optimal. Since measurement errors will guarantee that this minimization will never truly approach zero, a deterministic approach, for example

the TRIAD algorithm, discards part of the measurements so that a solution exists (16). The problem becomes largely simplified and computationally fast, thus leading to its popularity since its creation in the 1970s. The drawbacks of TRIAD, however, are in the complex computation of its covariance matrix and its limit of accommodating only two vectors observations at a time. More than two vectors may be utilized only by clumsily combining attitude solutions for different observation-vector pairs. Furthermore, the initial discarding of information at the start of the algorithm causes a loss of accuracy, while the order at which the algorithm handles the vectors affects the resulting attitude solution (16, 2).

2.5.2 QUEST Algorithm. Optimal algorithms, on the other hand, compute a best estimate of the spacecraft attitude based on a quadratic loss function, taking into account all n measurements. The loss function $L(\mathbf{A})$ is derived from Eq. (14) and may be of the form

$$L(\mathbf{A}) = \frac{1}{2} \sum_{i=1}^n a_i |\hat{W}_i - \mathbf{A} \hat{V}_i|^2 \quad (15)$$

where $a_i, i = 1, \dots, n$ are a set of nonnegative weights. Equation (15) is the loss function for the Quaternion Estimation (QUEST) algorithm. The primary disadvantage to optimal algorithms is that they are typically slower than deterministic algorithms. However, with the QUEST algorithm, not only is the problem simplified by utilizing the four elements of the quaternion \bar{q} (explained below) instead of the nine elements of \mathbf{A} , but the inherent approximation scheme allows for results with the speed of a deterministic algorithm and the accuracy of an optimal result (16).

Returning to Eq. (15), it can be noted that since the loss function $L(\mathbf{A})$ can be scaled without affecting the determination of the optimal attitude matrix \mathbf{A}_{opt} , it is

possible to set

$$\sum_{i=1}^n a_i = 1 \quad (16)$$

Then the gain function $g(\mathbf{A})$ is defined by

$$g(\mathbf{A}) = 1 - L(\mathbf{A}) = \sum_{i=1}^n a_i \hat{W}_i^T \mathbf{A} \hat{V}_i \quad (17)$$

To maximize the gain function $g(\mathbf{A})$, the loss function $L(\mathbf{A})$ must be minimized through application of the optimal attitude matrix \mathbf{A}_{opt} . The gain function $g(\mathbf{A})$ can be written in terms of the trace (16) which results in

$$g(\mathbf{A}) = \sum_{i=1}^n a_i \text{tr}[\hat{W}_i^T \mathbf{A} \hat{V}_i] = \text{tr}[\mathbf{A} \mathbf{B}^T] \quad (18)$$

where tr denotes the trace operation, and \mathbf{B} is the attitude profile matrix, given by

$$\mathbf{B} = \sum_{i=1}^n a_i \hat{W}_i \hat{V}_i^T \quad (19)$$

Since it is more convenient to express \mathbf{A} in terms of quaternions, the attitude matrix \mathbf{A} is expressed as

$$\mathbf{A}(\tilde{q}) = (q_4^2 - \vec{q} \cdot \vec{q}) \mathbf{I} + 2 \vec{q} \vec{q}^T + 2q_4 \mathbf{Q} \quad (20)$$

where \mathbf{I} is the (3×3) identity matrix and \mathbf{Q} is termed the antisymmetric matrix

$$\mathbf{Q} = \begin{bmatrix} 0 & q_3 & -q_2 \\ -q_3 & 0 & q_1 \\ q_2 & -q_1 & 0 \end{bmatrix} \quad (21)$$

The use of quaternions subjects the optimal solution to a single constraint, which can be written as

$$\tilde{q}^T \tilde{q} = |\vec{q}|^2 + q_4^2 = 1 \quad (22)$$

where \mathbf{K} is a (4×4) matrix defined as

$$\mathbf{K} = \begin{pmatrix} \mathbf{S} - \sigma \mathbf{I} & Z \\ Z^T & \sigma \end{pmatrix} \quad (23)$$

and $\mathbf{S} - \sigma \mathbf{I}$ is a (3×3) matrix, Z is a (3×1) vector, Z^T is a (1×3) vector, and σ is a scalar. These quantities are defined as

$$\sigma = \text{tr} \mathbf{B} = \sum_{i=1}^n a_i \hat{W}_i \cdot \hat{V}_i^T \quad (24)$$

$$\mathbf{S} = \mathbf{B} + \mathbf{B}^T = \text{tr} \mathbf{B} = \sum_{i=1}^n a_i (\hat{W}_i \hat{V}_i^T + \hat{V}_i \hat{W}_i^T) \quad (25)$$

$$Z = \sum_{i=1}^n a_i (\hat{W}_i \times \hat{V}_i^T) \quad (26)$$

Through the substitution of Eq. (20) into Eq. (17), the gain function $g(\mathbf{A})$ may be written as

$$g(\tilde{q}) = (q_4^2 - \vec{q} \cdot \vec{q}) \text{tr} \mathbf{B}^T + 2 \text{tr} [\vec{q} \vec{q}^T \mathbf{B}^T] + 2q_4 \text{tr} [\mathbf{Q} \mathbf{B}^T] \quad (27)$$

or into the bilinear form

$$g(\tilde{q}) = \tilde{q}^T \mathbf{K} \tilde{q} \quad (28)$$

It is now clear through Eq. (28) that finding the optimal attitude expression is reduced to finding the quaternion that maximizes $g(\tilde{q})$. The quaternion constraint from Eq. (22) can be implemented into the computation by using Lagrange multipliers (16). Thus, a new gain function $g'(\tilde{q})$ that includes the quaternion constraint can be introduced as

$$g'(\tilde{q}) = \tilde{q}^T \mathbf{K} \tilde{q} - \lambda \tilde{q}^T \tilde{q} \quad (29)$$

where λ is chosen to satisfy the constraint. Differentiation of Eq. (29) attains a maximum or minimum value if

$$\mathbf{K} \tilde{q} = \lambda \tilde{q} \quad (30)$$

Thus, the optimal quaternion \tilde{q}_{opt} must be an eigenvector of \mathbf{K} . Since Eq. (30) is independent of the normalization of \tilde{q} , the constraint condition does not determine the eigenvalue λ . However, since λ must be an eigenvalue of \mathbf{K} for each eigenvector of \mathbf{K}

$$g(\tilde{q}) = \tilde{q}^T \mathbf{K} \tilde{q} = \lambda \tilde{q}^T \tilde{q} = \lambda \quad (31)$$

The optimal quaternion \tilde{q}_{opt} is then the eigenvector of \mathbf{K} that corresponds to the largest eigenvalue of \mathbf{K} , resulting in the maximization of $g(\tilde{q})$ (16). This relationship

can be expressed as

$$\mathbf{K}\tilde{\mathbf{q}}_{opt} = \lambda_{max}\tilde{\mathbf{q}}_{opt} \quad (32)$$

2.5.3 Attitude Determination Algorithm Summary. While the choice of attitude determination algorithms is many, each one is better suited for different requirements. The deterministic TRIAD algorithm, through its speed and simplicity, is appropriately suited for medium-accuracy missions (2). The optimal QUEST algorithm has shown to be the most popular attitude determination method in high-accuracy missions, where the additional computational burden is worthwhile(16). Indeed, it can be shown that the QUEST attitude solution for a problem given only two observation vectors is the TRIAD attitude matrix (16). The QUEST algorithm is, however, an estimation method, necessary in order to balance its application of optimization combined with its relatively moderate speed of calculation. QUEST, therefore, can represent somewhat of a compromise between a purely deterministic and purely optimal approach.

2.6 Laboratory Testing

As with any component of a spacecraft, star trackers are rigorously ground tested. While Liebe describes a method to test star trackers using the real sky (10), several examples of star tracker laboratory setups exist. These typically center around the type of optical simulator used for testing. Some testbeds have optical simulators that remain in a completely fixed position in the testbed. Figure 22 shows an example of this type of “bench” test method, where the star tracker is placed on the test bed opposite an imaging screen, with an optical collimator in between. The optical collimator corrects the finite conjugate image geometry projected on the screen to

simulate star images from infinity, while the imaging computer is able to stream dynamic images to the star tracker. This simulates star tracker relative motion, and facilitates testing of the star tracker hardware using star catalog imagery (23).

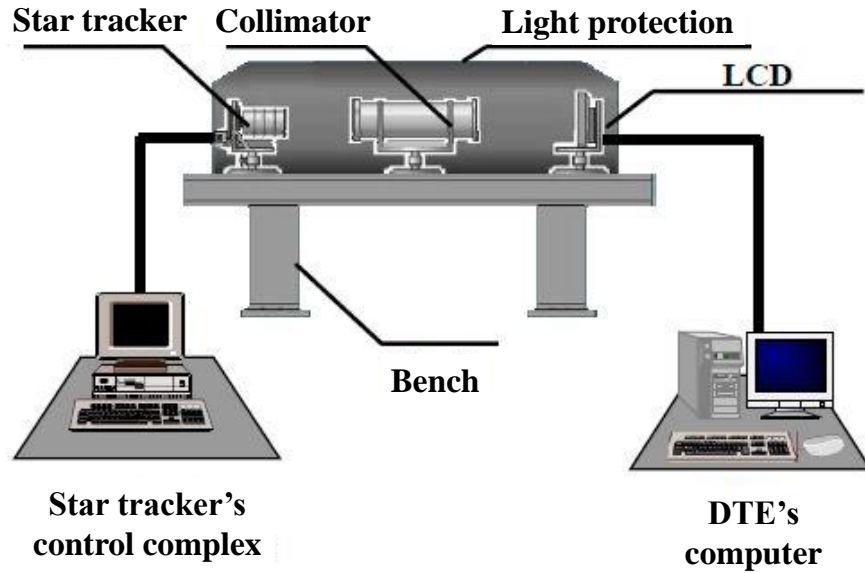


Figure 22: Fixed Star Tracker Testbed (23)

Other optical simulators, on the other hand, are made for testing applications where fixed bench-style testing may not be desired. These may involve a testbed that exhibits a given free range of motion for the star tracker, more closely simulating the dynamics involved in spaceflight. Figure 23 depicts such a test setup from ASTRIUM. In this case, the optical simulator is directly mounted to a star tracker, providing the ability to mount directly on a dynamic platform. The optical simulator is composed of a microdisplay element, optical collimator, and imaging software. It is capable of displaying star catalog or customized star images via a pre-programmed sequence, or through remote or close-loop control using feedback sensors for attitude information into the imaging system (1).

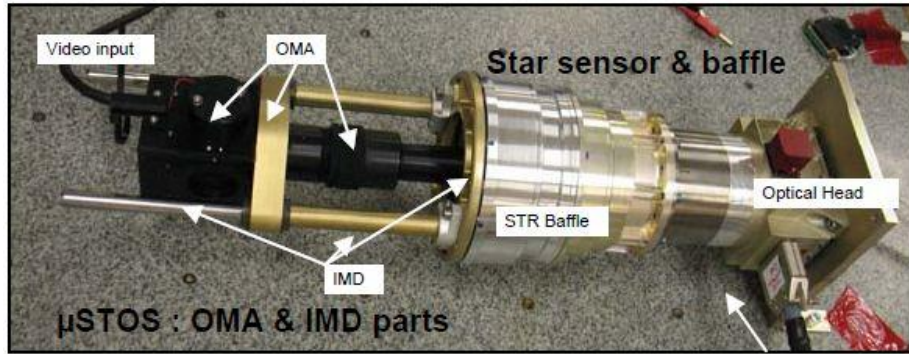


Figure 23: Minituarized Optical Simulator (1)

Another optical simulator currently in use is John Hopkins University(JHU)/Applied Physics Laboratories(JHU) Optical Simulator and Testbed. The objective of the research was to design and build a controlled laboratory testbed to realistically test basic star tracker functions, including different sensors and algorithms, while avoiding the background and star twinkle noise sources inherent to ground-based open sky testing (3). In this setup, a 4-ft radius hemispherical dome is placed over the tested star tracker mounted on a two-axis actuated mount. The dome holds 100 fiber optic patch cords connected to banks of white light emitting diode (LEDs). This simulates 100 of the brightest stars in the northern hemisphere. Figure 24 is a photograph of the device.

The dome was precision surveyed after manufacturing to ensure a minimal variation in radius. After stretching, the variation in radius was found to be as low as 0.4%. The star pattern was constructed by mounting a laser emitter coupled with a collimating lens on the star tracker base, and positioning the laser to the exact position of the star. A drill was then used to make a small hole for the fiber optic chord. The LEDs were biased and calibrated prior to testing. Preliminary testing with a representative star tracker revealed that the concept has merit, although some correctable angular discrepancies were reported (3).



Figure 24: JHU/APL Optical Simulator (3)

2.7 *Satellite Simulators*

There are several satellite simulators used for educational and commercial research purposes across the globe(15, 13, 12, 19). With respect to the scope of this research effort, only AFIT's SimSat and the Naval Postgraduate School NPS's) Second-Generation Three-Axis Spacecraft (TAS-2) simulator will be discussed.

2.7.1 AFIT SimSat. AFIT's SimSat is a tabletop configuration satellite dynamics simulator mounted atop a spherical air bearing, capable of $\pm 30^\circ$ rotation about its X- and Y-axis and full rotation about its Z-axis, and controlled remotely via a ground station PC. Figure 25 shows SimSat in its most recent form prior to the installation of the star tracker used in this research. It has three methods of actuation: three fan/thruster pairs, three reaction wheels and four single gimbal control moment gyroscope (CMGs) in a pyramid configuration. Control is executed via the dSpace MicroAutoBox, a programmable real-time data acquisition and processor. Software,

programming, and interfacing is facilitated via an onboard Mini-Box PC, which hosts the MATLAB[®]/SIMLINK control programs, as well as the dSpace ControlDesk real-time interface. Attitude information is supplied via a Northrop Grumman LN-200 Fiber Optic Gyroscope Inertial Measurement Unit (IMU). The LN-200 is configured with three orthogonal fiber-optic gyroscopes to provide angular rates, and three orthogonally mounted accelerometers to provide angular accelerations and measure the gravity vector (12, 15, 19). The research presented here represents one of several incremental changes to its configuration and capabilities over the past several years. See McChesney (12), Roach *et al.* (15), and Snider (19) for more information.

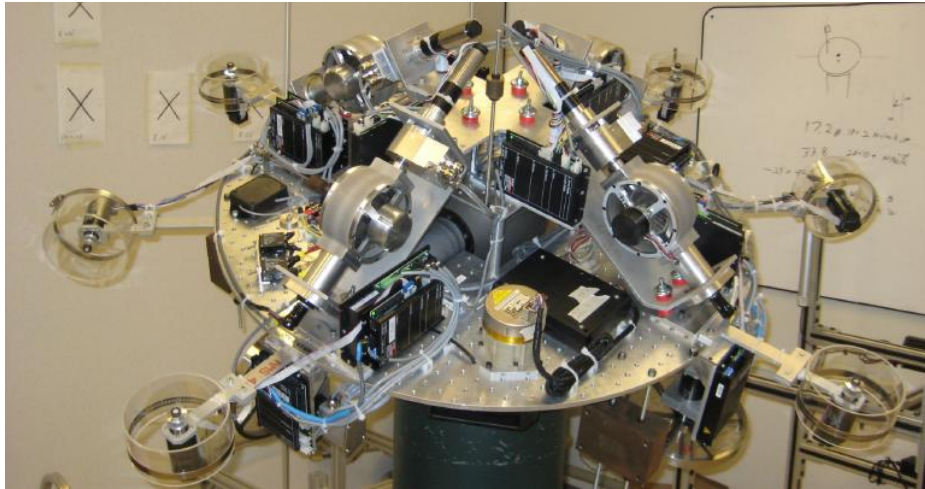


Figure 25: SimSat Previous Configuration (12)

Before completing this research effort, initializing SimSat’s initial attitude involved visually aligning SimSat with a predetermined inertial coordinate frame in the laboratory and reinitializing its IMU data. In other words, the initialized orientation of SimSat which sets its current Euler Angles to the ideal “home” position $[0, 0, 0]^T$, is completely based on the user’s setting of the initial orientation, which is somewhat arbitrary in terms of a few degrees. This effectively biases the vehicle attitude, and

has become a normal step in day-to-day operation of the simulator. Furthermore, the IMU regularly precesses over time and after a few relatively large maneuvers, adding further bias to the attitude measurements supplied to the SimSat controller. This requires regularly “resetting” SimSat, by commanding it to its last known “home” position, deactivating the actuators, manually repositioning SimSat to the “home” position, and reinitializing the attitude.

2.7.2 NPS TAS-2. In 2009, the NPS researched the addition of a star tracker reference system on a laboratory-scale spacecraft simulator, the TAS-2 (22). The TAS-2 is a tabletop configuration spacecraft dynamics simulator designed as a research test bed for acquisition, pointing, and tracking techniques (22). The TAS-2 is maneuvered atop a spherical air-bearing, actuated by an array of three variable-speed CMGs. The attitude determination devices used on the TAS-2 include IMUs with integrated rate gyroscopes, two inclinometers, a two-axis analog sun sensor, and a camera functioning as the optics and CCD sensor of a star tracker. Two simulated, gimballed space telescopes are used to represent the spacecraft payload. Several on-board computers process the sensor and controller information for the vehicle (22). Figure 26 shows the latest TAS-2 configuration.

The star tracker camera is a WAT-902H2 SUPREME CCD camera with a Pan-tex wide FOV lens. The lens system has an 8.5 mm focal length to allow for view of the entire star field for a small range of motions (22). A specialized platform was made to mount the camera closer to the screen, at a distance of approximately 1 meter from the screen. The camera’s position relative to the vehicle’s center of rotation can be seen Fig. 26. Calibration is performed by removing any “hot” pixels upon the CCD device prior to experimentation. A star field was projected on a flat panel LCD monitor placed over the test bed, and the lab lighting was dimmed.

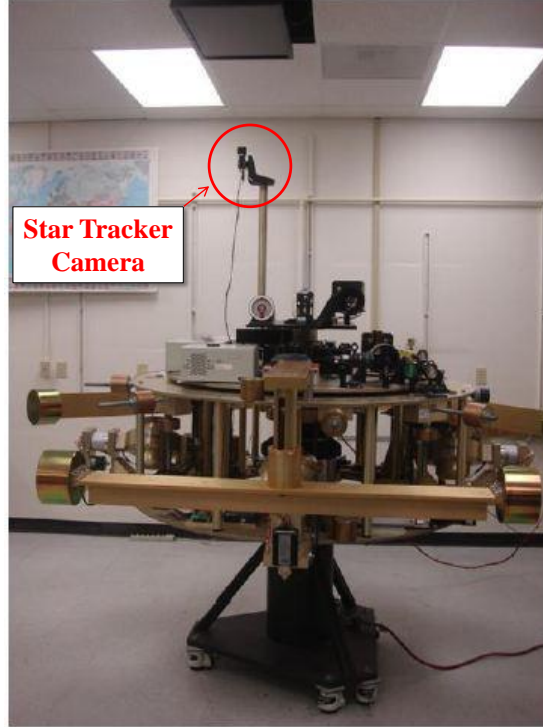


Figure 26: NPS TAS-2 with monitor (22)

The star tracker was mounted over the TAS-2, aligned with the inertial axis, and offset from the axis of rotation. This relationship was illustrated by Tappe (22) through vector representations of the star field and the two coordinate frames. Figure 27 shows this relationship, where I is the inertial frame, B is the star tracker frame origin, I' is the inertial frame translated to the star tracker frame, and B' is the star tracker frame translated to the inertial frame origin. The inertial frame is fixed and centered at the center of the TAS-2's spherical air bearing. R_O is the position vector that describes the star tracker frame's position with respect to the inertial frame.

From Fig. 27, it can be seen that the angle between the inertial vectors r_1 and r_2 to stars s_1 and s_2 is not the same as the angle between the corresponding star tracker vectors b_1 and b_2 . According to Tappe (22), the generalized relationship can

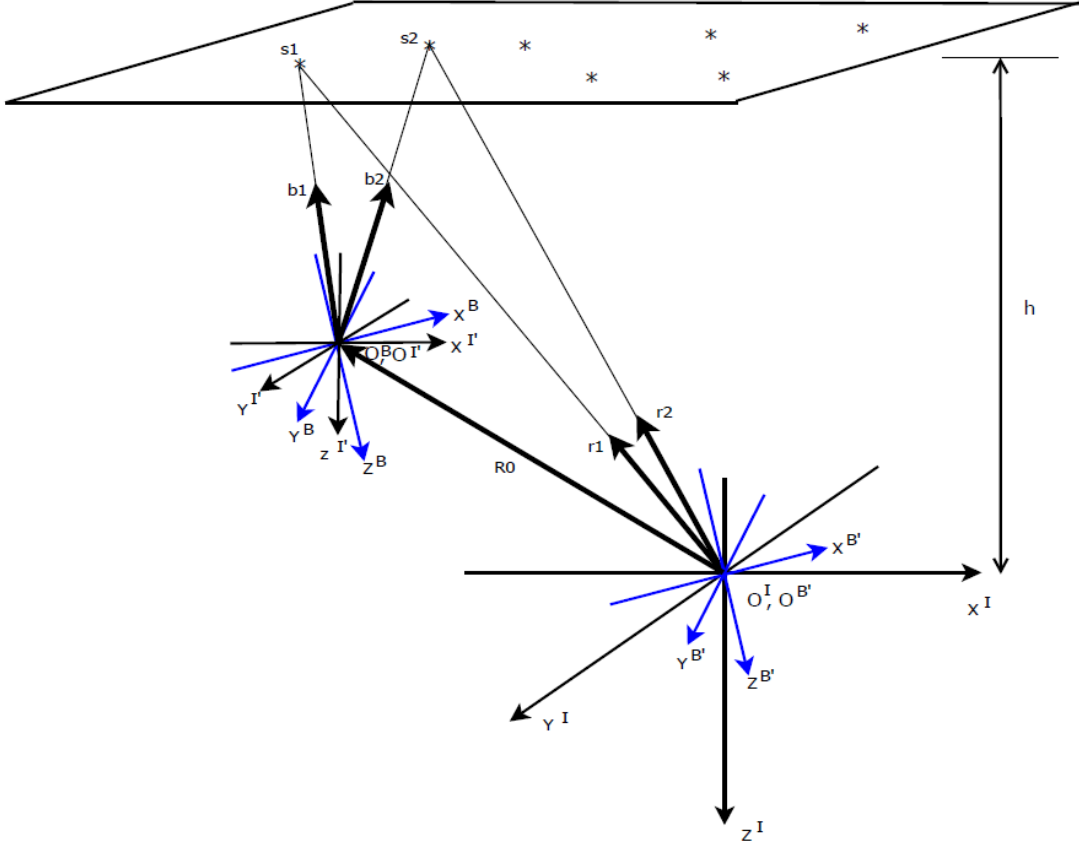


Figure 27: Vector Representation of Flat Star Field and Reference Frames (22)

be defined as

$$R_0^{B'} + \alpha_i b_i^B = \mathbf{A} \beta_i r_i^I \quad (33)$$

for all i vectors, where α_i is the distance between the i^{th} star and the star tracker frame origin, and β_i is the distance between the i^{th} star and the inertial frame origin. Equation (33) is a nonlinear equation, since α_i is dependent on \mathbf{A} (22).

The nonlinearity of Eq. (33) required a different approach to implementing the system for testing. With the spacecraft at zero attitude, \mathbf{A} equals the identity matrix, thus α_i is known and building a star catalog by using Eq. (33) to map the star tracker vectors to the inertial frame is straightforward. However, once \mathbf{A} becomes uncertain, α_i

cannot be solved for without a complex optimization problem (22). Therefore, Tappe made use of an initial attitude estimate with which to solve for α_i . This allows for the left side of equation Eq. (33) to be determined, where then the angles between the star tracker and catalog vectors may be compared and matched. Finally, the refined attitude matrix \mathbf{A} can be determined using the attitude determination algorithm.

The research objective for the NPS project was to integrate and evaluate three star pattern recognition (Angle, Triangle and Spherical Triangle) and attitude determination (Least Squares, TRIAD and QUEST) algorithms on a simulated spacecraft. The algorithms chosen for formal testing were the Angle method and the QUEST algorithm. First, the the star tracker built a catalog of the nine stars on the LCD screen with the TAS-2 completely level. Six trials were executed, with five tests each trial, and each test consisting of 50 averaged runs. All tests were executed with the TAS-2 at zero attitude in order to test the validity of the initial attitude estimation approach.

Initial attitude estimates from other sensors were simulated by inputting an initial \mathbf{A} “error matrix” at the start of each trial. The first five trials tested the algorithms with initial \mathbf{A} estimates with errors of 0, 3, 6, -3, -6 degrees, respectively. The sixth trial had an initial \mathbf{A} estimate of two degrees of error, but utilized five iterative attitude updates. All trials were executed five times, and each test produced fifty solutions, which were averaged and the standard deviation calculated. The accuracy criteria used in this testing was a star pair angular separation error of ± 500 arcseconds (22).

Dynamic testing of the Angle method and the QUEST algorithm yielded mixed results. On average, the algorithm matched about six stars out of the total nine stars over the course of testing. Additionally, the algorithm was able to approximate the vehicle’s attitude with initial estimate errors within -6 degrees to 3 degrees. Beyond

this range, the errors were too great to allow for star matching and attitude determination. The iterative approach showed marked improvements in the results, with the Euler Angles at near zero.

2.8 Summary

Chapter II covered the background information on spacecraft attitude determination and spacecraft dynamics. Next, star tracker operation was explored to emphasize the basic parameters that must be considered prior to efforts in developing, operating, and analyzing a star tracker system. Then, star pattern recognition and attitude determination algorithms were examined. Finally, existing star tracker testbeds were surveyed.

III. Methodology

3.1 Introduction

Chapter III covers the analysis of the problem introduced in Chapter I and the development, integration, and validation of the star tracker reference system concept for SimSat. The first section introduces the key requirements for a viable solution to the stated problem. The second section covers the hardware specifications of the system optics. The third section discusses the development of the LED concept beginning from preliminary output and physical configuration studies, to the analysis of the voltage control source, and finally to the introduction of the final LED sub-system concept. The next section details the analysis, specification, and installation of the selected star field surface. The fifth section covers the implementation of the angle and QUEST algorithms into the SimSat system. The final section of Chapter III presents the tests performed to validate the concept.

3.2 Key Requirements

Chapter II presented several aspects of the problem that required further consideration. Before implementing any possible hardware and software solutions, it is critical that key requirements related to the problem are analyzed and understood. If the task was to integrate a star tracker for use on a satellite testbed with direct sight of the real sky, then the approach to solving the problem is more closely related to a conventional satellite build-up case. Much knowledge of the relationship between the star tracker sensor, satellite interfaces, the celestial sky, and all associated error sources has accumulated over the span of 40+ years, as evident from the literature examined in Chapter II. However, for the case of an indoor laboratory testbed, few analogous cases exist, especially for a dynamic satellite simulation testbed. There-

fore, while analysis of the problem here may occur in a manner analogous to that of space-rated star trackers, specialized considerations must be made.

The research work done by NPS on the subject provides the most insight into the problem regarding the implementation of star trackers on dynamic testbeds (22). This configuration was chosen as the initial basis for this research effort since it is a completely external, space-representative method for attitude determination as compared to a setup such as ASTRIUM's (see Section 2.6). First, the system exhibited errors affecting the star matching portion of the algorithm under zero degree error testing, or in other words, a purely static test. While not directly assessed in the work, these errors can be attributed in a general sense to camera errors, LCD projection screen errors, algorithmic errors, or any combination of the three. The camera used was of the CCD sensor type, and while it is not known specifically which inherent noises may have been contributed here, it is likely that camera noise negatively affected the star brightness measurements.

Furthermore, the star pattern was projected on an LCD screen. The projected stars on the screen are not afocal point sources, as stars are treated, but rather they are a collection of LCD pixels that, when imaged, are transformed into a different collection of pixels many times smaller on the CCD sensor. This can lead to errors in centroiding calculations. Because the camera used is not highly-sensitive, error contribution from nonsystemic pixel noise from the LCD screen can be assumed to be small. However, if the camera exposure timing is short relative to the LCD screen refresh rate, resulting periodic fluxuations in measured star brightnesses are likely. Finally, the algorithm used a simplified filtering scheme where star separation angles were measured only with respect to the brightest star in the image, or the "master star" (22). When cataloged measurements were compared to the tracked measurements, star matches were made based solely on the most commonly reoccurring angle

matches associated with the master stars from the cataloged and tracked images. In other words, the master star of each image is the only star associated with a brightness value. If several stars have nearly the same brightness value as measured by the camera, this would allow the algorithm to pick different master stars across multiple images.

Second, dynamic testing, in which the TAS-2 was held at zero attitude while receiving various attitude matrices with given error angles, yielded important results (22). It was shown that the chosen test bed/star field configuration required a reliable initial attitude estimation from another sensor, otherwise accurate attitude determination would not be possible. Afterwards, with continuous attitude updates, testing demonstrated that corrections to erroneous initial attitude estimates could be made, resulting in far more accurate attitude solutions (22). This was necessary due to the geometric relationship between the star field, the star tracker frame, and the inertial frame used in the setup, as pictured in Fig. 27 and defined by Eq. (33).

For attitude determination in space, such a relationship is not applicable for a star tracker operating largely within the pinhole camera model. The celestial sphere is assumed to have a radius of infinity, so all star position vectors may be given the same unit length, and angular measurements become consistent across the celestial sphere. More importantly, the angles between two stars, as observed from two different locations at relatively finite distances away, may be approximated as nearly equal. This is the key to the comparison of vector observations from an Earth-based observatory to those made by a star tracker mounted on a satellite floating many miles above the Earth. Figure 28 is a close-up view of the two observation points operating within the pinhole camera model (see Fig. 9), where the vectors r_1 and r_2 point to the same pair of stars at a near-infinite distance. r_p is then the finite distance between the reference frames, and the separation angles θ are equal in this case.

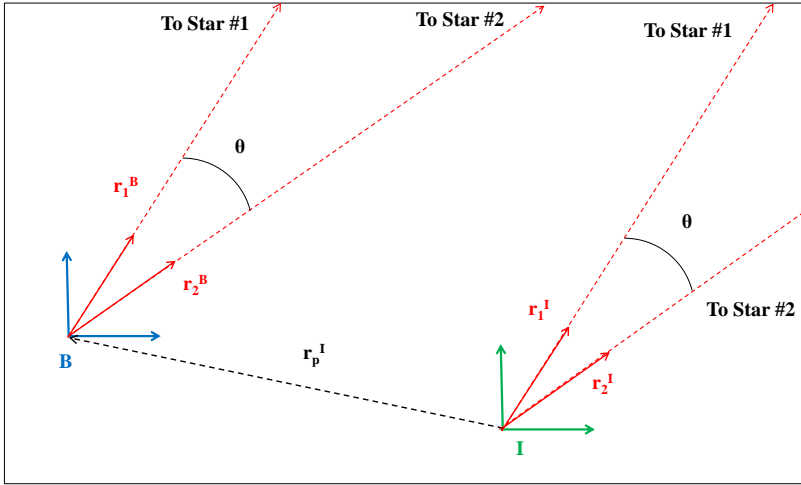


Figure 28: Equal Separation Angles from Two Observation Points

Using knowledge of the pinhole camera model and the insight gained from the NPS’s previous research, various approaches could be implemented to solve the problem presented in this research. For this initial stage of research, an exploratory approach that focused on the extraction of the key parameters of star brightness and angular separation, as well as correctly mapping the position vectors to each star, was used. This allows for the choice of the Angle algorithm for star pattern determination. Other parameters can be extracted and utilized by future algorithms. Ultimately, the solution to the problem addressed by this research will require consistent feature measurements from all possible vehicle orientations, subject to the precision and accuracy requirements of the given spacecraft simulator. For space-rated star trackers, the pinhole camera model and expensive (greater than \$500,000), highly-accurate sensors provide most of this.

3.3 *SimSat Star Camera and Lens System*

The camera sensor is the measurement instrument for the star tracker, and therefore the foundation for the performance of the entire system. For this research

effort, it was unnecessary to procure a space-rated star tracker. Such star trackers' optics are calibrated for use in space and otherwise very expensive. No accuracy requirements were stated regarding attitude for this baseline research. One requirement, however, was that the camera had to be integrated onto SimSat, thus it needed to be easily mountable and interface with the SimSat Mini-Box. Since the IMU is the primary attitude measurement sensor, SimSat did not require a high attitude update rate from the star tracker, thus selecting a camera based on a minimum frame rate of 1 fps was acceptable. Finally, although image resolution was rarely addressed in the background literature, higher resolutions allow for improved centroiding in lieu of more complex algorithms that determine the centroid at the sub-pixel level. There was an associated cost in terms of increased noise propensity due to the increased number of pixels, as well as higher data and computational requirements necessary to process the larger image data.

The camera chosen was a Lumenera Lu205c 2.0 Megapixel USB 2.0 camera with a 35mm multi-Megapixel CCTV lens. The camera is capable of 10 fps at full 1600x1200 resolution and on-board image processing. Coupled with the lens, the newly-built star tracker attained a FOV of approximately 10 degrees in the horizontal. Since the FOV, discussed in Section 2.3.1, affects the angular resolution of the image and the extent of star field coverage per image frame, this FOV balances the need to acquire detailed star field images containing the requisite number of stars versus keeping the later task of populating the star field practical. Figure 29 is a photograph of the camera mounted on the newly installed camera deck, which locates and centers the camera sensor approximately 15 inches from the SimSat air bearing.

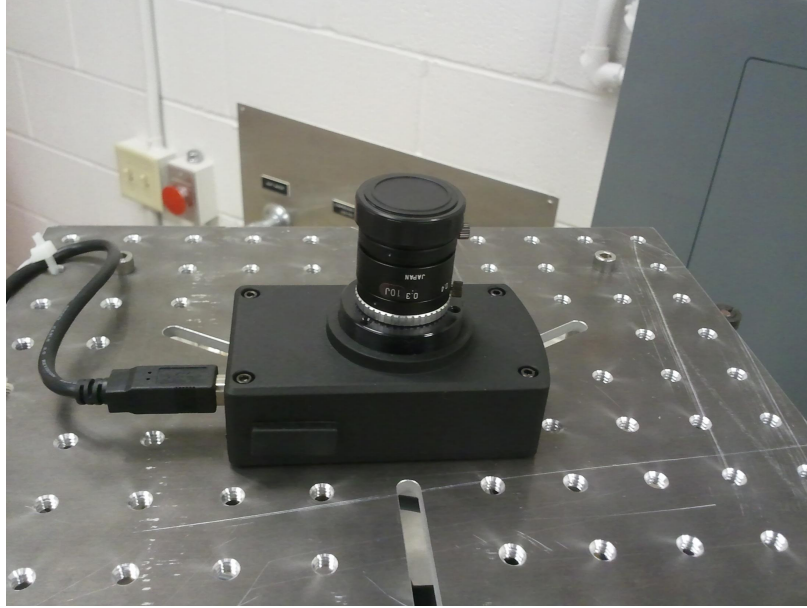


Figure 29: Lumenera Lu205c Camera

3.4 LED Development

With the camera and optics selected, the next step involved deciding on the type of light source to represent the stars. The use of an LCD screen by Tappe was an obvious first step, since its projective nature makes it the most versatile method. But as discussed in Section 3.2, any light source mounting on a flat surface is unacceptable. The success of the test bed developed by Boone would suggest that a similar setup would be optimal for this research. However, this methodology involves hard-mounting a complex and costly LED/fiber optic system. To have proceeded directly in this manner would have been premature without first understanding the many test bed and algorithmic uncertainties addressed in this research. Thus, inexpensive LEDs, which cost on the order of \$0.25 to \$0.50 each were chosen as acceptable star representations.

3.4.1 LED Preliminary Studies.

3.4.1.1 Output Considerations. In order to choose the correct LED, several considerations had to be carefully weighed. First, LEDs are made in several

sizes, but are not ideal point sources at larger sizes. Very small LEDs, while promising substitutes for point sources, are difficult to handle during developmental research and testing. Thus, a small LED size which could be reasonably manipulated during this research effort would be chosen. Second, the color of the LEDs had to be selected. Although some data existed regarding the light sensitivity of the camera sensor, it was unclear how well it would work with a particular color LED. Thus, three colors, red, green, and blue were initially chosen for analysis. The use of different colors also adds a second level of variation to the overall LED intensities when coupled to different resistors.

The third consideration, LED light output, was the most critical. The “brightness” of an LED is most directly controlled by the amount of current flowing through an LED. Ohm’s law stating that

$$V = I/R \tag{34}$$

requires that a resistor of some resistance value be placed in-line with any LED, and that the necessary resistance will be a function of the voltage source, the LED’s forward voltage and forward current properties. Therefore, the limiting variables of the light output of the LED will be the minimum current at which it can effectively output light, and the maximum current rated by the manufacturer.

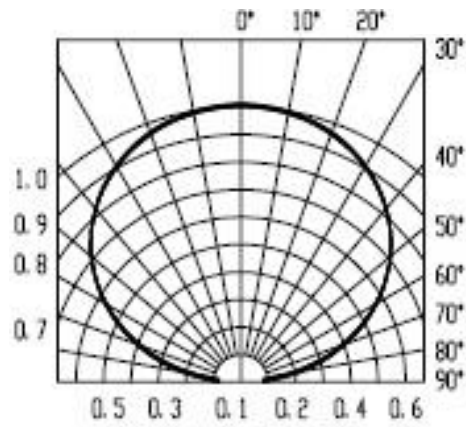
The luminance of an LED describes the LED’s light output over a given area and is the parameter most directly related to the amount of light detected over the camera sensor’s pixels. An LED whose output is relatively uniform, regardless of viewing angle, is said to be Lambertian, where the the luminance is isotropic. This property is key to simulating a point source of light since the measured brightness of the LED must be the same regardless of the viewing angle. Figure 30 shows the

manufacturer-supplied radiation pattern plots for the preliminary LEDs selected. Note that a wider curve typically gives an LED a Lambertian light output.

Noting the above considerations, red, green, and blue Lumex 1209 LEDs were selected for preliminary analysis. These LEDs would have to be coupled with appropriate resistors. Resistors determined to be in the safe operating range for these LEDs were between 100 and 10,000 ohms. Thus, selecting and pairing appropriately-sized resistors to yield a specific current would determine the light output of the LED. For the 5 V DC supply voltage and mentioned resistor values, the currents through these LEDs ranged between 3 mA to 0.15 mA. The physical characteristics of the selected preliminary LEDs is shown in Fig. 31.

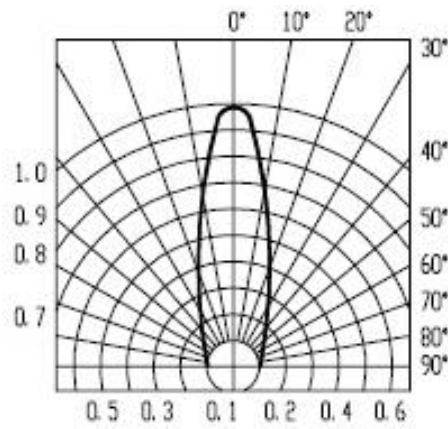
3.4.1.2 Physical Considerations. Physically constructing useful star patterns out of the selected LEDs onto the star field surface using materials and methods compatible with an experimental methodology required a simplifying, but versatile approach. It was already decided that the LEDs would be “soft-mounted”, or simply glued or adhered, to the star field surface to facilitate an experimental approach. Instead of wiring and placing individual LEDs onto the surface, a multitude of LEDs/resistor combinations were mounted on “patch boards” and wired to the power source. This arrangement greatly simplified multiple placements of LED on the star field surface, and also simplified the construction and wiring process of the LED support electronics.

The selected arrangement was based on a 3×3 square pattern for a total of nine LED per patch board. Figure 32 is a conceptual layout of the pattern arrangement. The colored line segments in Fig. 32 represent the distinct angular separations between the lit LEDs that the star tracker would detect. Assuming that only one star pair is lit on the patch boards such that a minimum of two stars are maintained in view for all



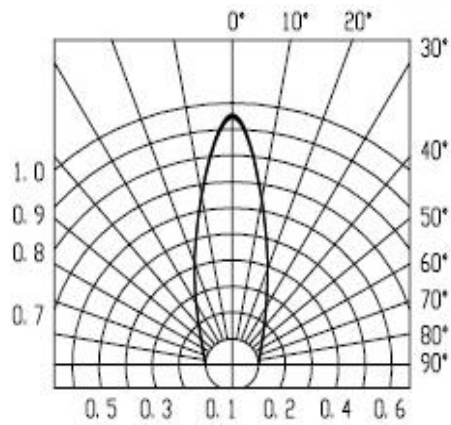
(11)

(a) Red LED



(11)

(b) Green LED



(11)

(c) Blue LED

Figure 30: Preliminary LED Radiation Pattern Plots

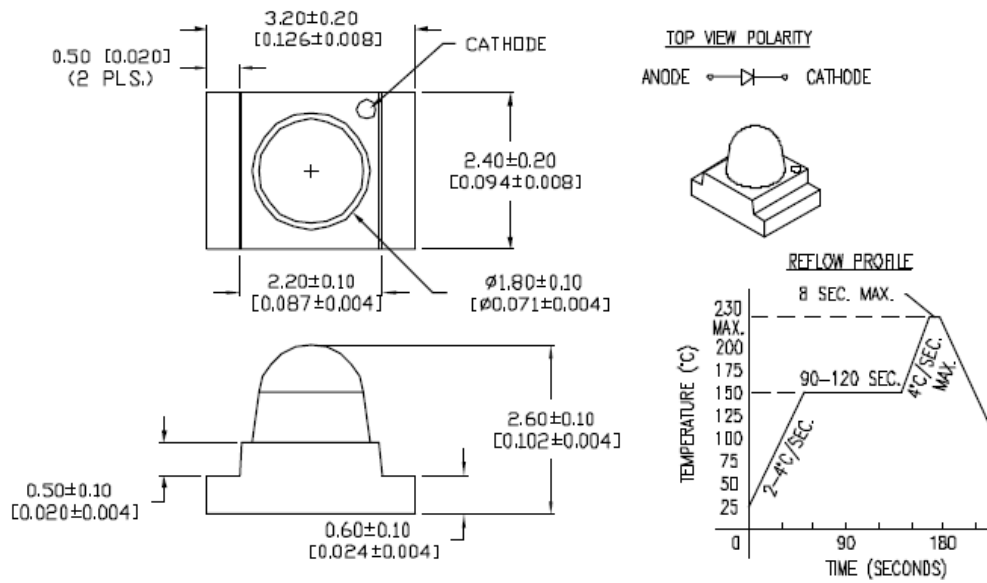


Figure 31: Preliminary LED Physical Characteristics
(11)

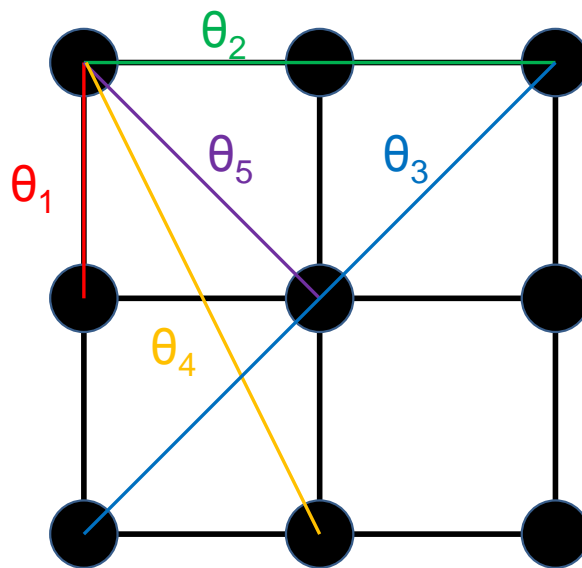


Figure 32: Patch Board Pattern

possible positions of the star field, and that the vehicle maneuvers into a region where the star tracker has only one patch board in view, this arrangement then guarantees a maximum of five unique angular separations for any combination of LED pairs.

Having created the patch board pattern, the physical arrangement of the associated electronics was developed. For the three-color LED arrangement, the preliminary patch board to be used for testing was fitted with three LEDs of each color, with each color receiving a 1,000, 5,000, and 10,000 ohm resistor. These resistors represent the range of desirable resistance values. The patch board had to be as small as possible for this configuration in order to best conform to the star field surface. Therefore, a 1 inch \times 1 inch square for the patch board was selected, with a uniform 8 mm spacing between LED centers. Figure 33 is schematic of the patch board layout, and Fig. 34 shows photographs of the actual patch board prototype. Note that resistors were not yet fully installed in this example. After a few of these boards were built, the next step was to perform preliminary testing and analysis.

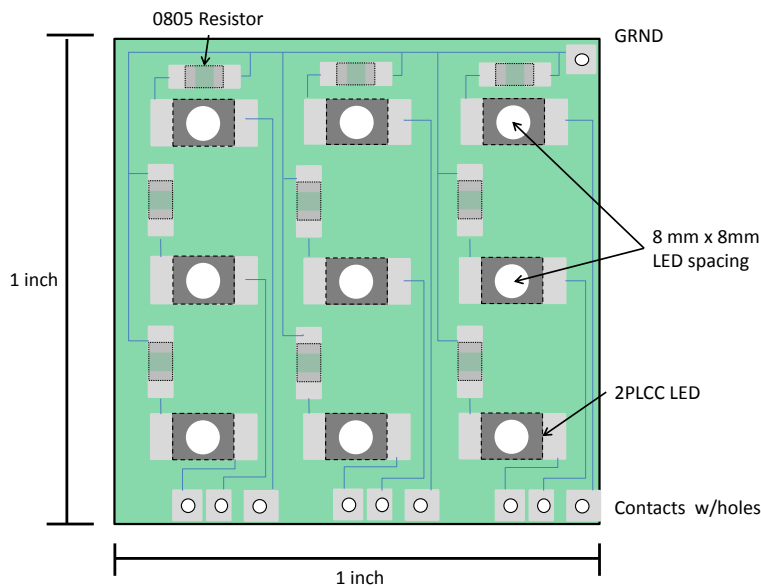
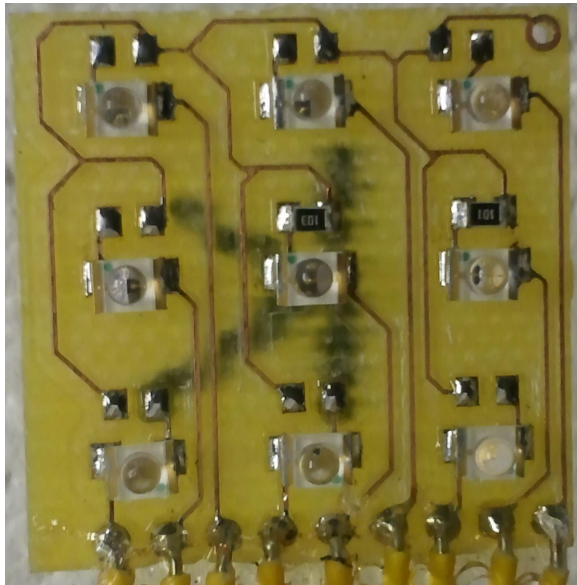
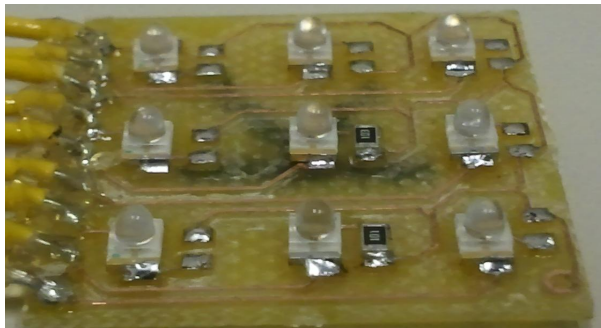


Figure 33: Patch Board Schematic
(11)



(a) View from Top



(b) View from Angle



(c) Mounted with Black Masking

Figure 34: Patch Board

3.4.1.3 Preliminary Analysis. The purpose of preliminary testing of the selected LED configuration was to gain knowledge of the relationship between the star tracker, SimSat, and the LEDs, specifically the controllable factors that influence the measurement of LED brightness magnitude. For this testing, a simple test stand was constructed, where a single patch board was mounted on a beam suspended 3 ft above SimSat resting on the air bearing pedestal, shown in Fig. 35 with the laboratory lights dimmed.



Figure 35: SimSat with Preliminary LED Test Stand

For multi-positional measurements, SimSat was set at various static positions and images were sampled with the patch board still within the FOV. This quasi-dynamic testing was to measure any variations of LED magnitude resulting from different viewing angles of the LED. Throughout initial testing, numerous factors were found to contribute to the final magnitude measurement of each LED for use in the star pattern recognition algorithm. What was found is qualitatively described as:

- Focus and aperture settings on the camera lens

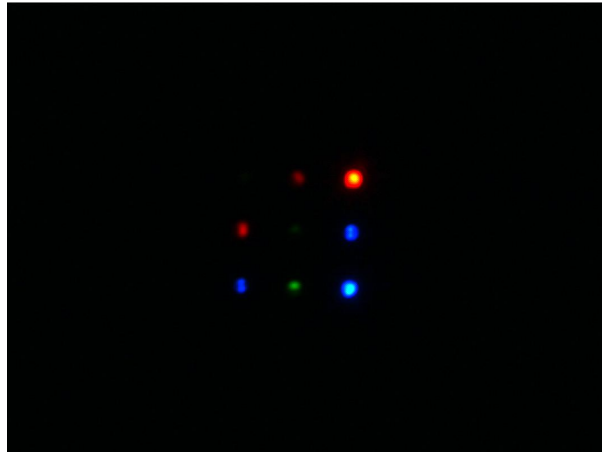
- Camera exposure and algorithmic settings for star detection
- LED overall light output

The high resolution of the star tracker camera allows it to sense minute details exhibited by the LEDs. This often meant that the camera was capable of resolving the diode and other internal features of the LED lens itself, which was too much detail for a point source simulation. Since defocussing the optics is a typical practice in space applications, slightly defocussing on this lab camera lens in order to eliminate excessive detail proved beneficial. A related setting was the aperture of the lens, which controls the amount of non-collimated, or indirect, light passing through the lens. The primary effect of decreasing the aperture was that the contrast between direct light sources (such as the more directional light from the LEDs) and indirect light (such as the ambient and reflective light from the surrounding laboratory) was increased so that only the light from the LED would be sensed by the star tracker. A secondary effect of reducing the aperture is that it increased the effective focal range of the camera, thereby making the image appear “sharper” for a given focus setting. The images in Fig. 36 illustrate this process. Note that the laboratory lights were dimmed to minimize the sensing of extraneous objects.

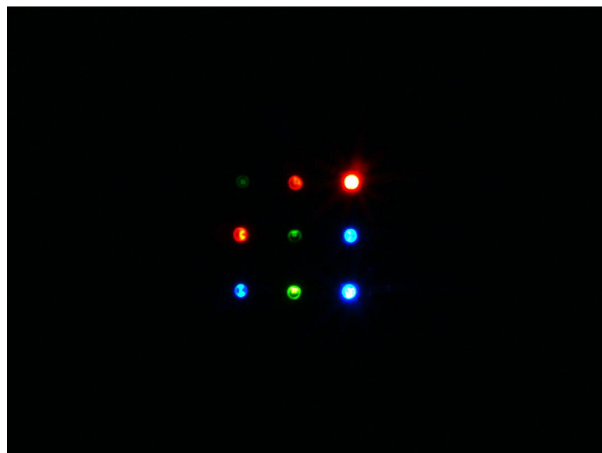
Figure 36 (a) shows all nine LEDs were sensed by the camera. Too much light was being emitted by the brightest red LEDs, resulting in glaring and reduced color saturation of the LED images. Furthermore, the dimmest green LED’s (at the top left) light emission resulted in a discontinuous shape. The next step was to reduce the aperture and focus, shown in Fig. 36 (b), which resulted in improving the features of the brighter LEDs at the cost of decreasing reception of the dimmer LEDs. Subsequent adjustments showed that with even just a slightly wider aperture, too much blur distorted the shape and the integrity of the light from the LEDs. Thus, the two settings were adjusted simultaneously, resulting in an image with a dark background,



(a) Focused and Wide Aperture



(b) Less Focus and Narrow Aperture



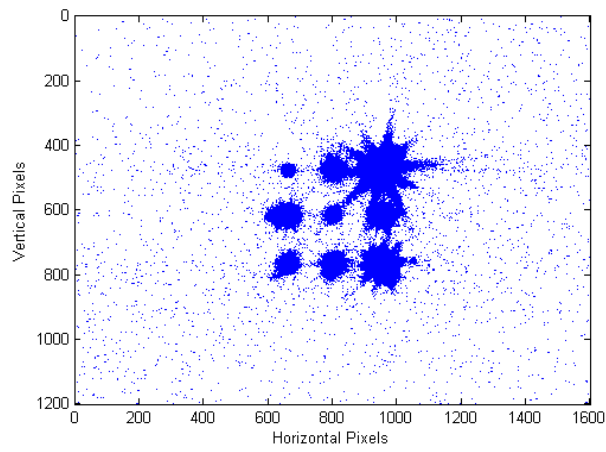
(c) Balanced Focus and Aperture

Figure 36: Patch Board Image Focus and Aperture Adjustments

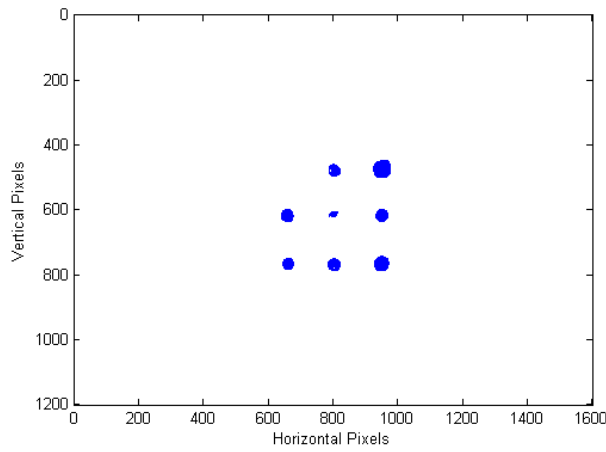
relatively-consistent internal features, and circular LED shape profiles, as seen in Fig. 36 (c).

The camera exposure and algorithm threshold settings are controlled via software associated with each component. The exposure, along with the aperture, controls the total amount of light impinging on the sensor. The time duration of light collection on the sensor is the exposure time of the image, and directly affects the overall image brightness. Short exposures result in dimmer images, but are sensitive to fluctuations in brightnesses. For long exposures, more light is collected, therefore the resulting images are brighter, and any brightness variations over the course of the exposure duration are steadied. However, long exposure times are also sensitive to motions which may result in smearing of the LEDs across the image. Shorter exposures can address this issue.

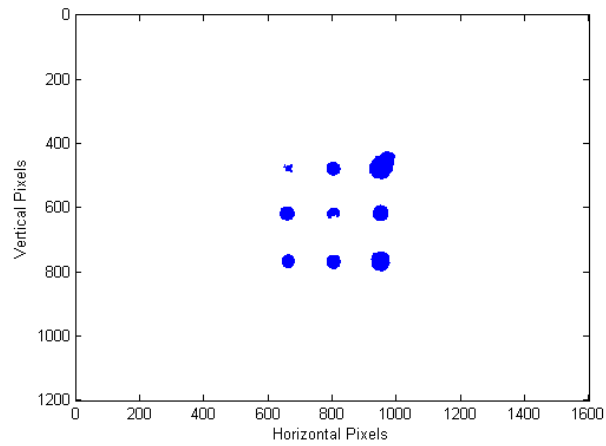
Once the images were collected with the appropriate focus, aperture, and exposure settings, the algorithm must then process the images and detect the LED. Two threshold settings within the algorithm determine detection of an LED: pixel intensity and area. The pixel intensity threshold tells MATLAB[®] which pixels are bright enough to possibly comprise a star. The algorithm first converts all color images to gray scale, or the average of the red, green, and blue channel values, therefore reducing the image into its basic luminosity values. With the image background black, any pixels above a set percentage of total luminosity were identified for processing. Next, to sort against noisy pixels, a “blob” analysis was performed, where the groupings of pixels above the luminosity threshold were identified. The total pixel areas of these groupings must then be above a certain area threshold to be considered an LED. The resulting image from Fig. 36 (c) was analyzed in this manner, as depicted in Fig. 37. Figure 37 shows the sparsity matrices of the resulting image analysis, holding exposure constant. Only the pixels above the intensity threshold are plotted in blue.



(a) 2% Intensity Threshold



(b) 25% Intensity Threshold



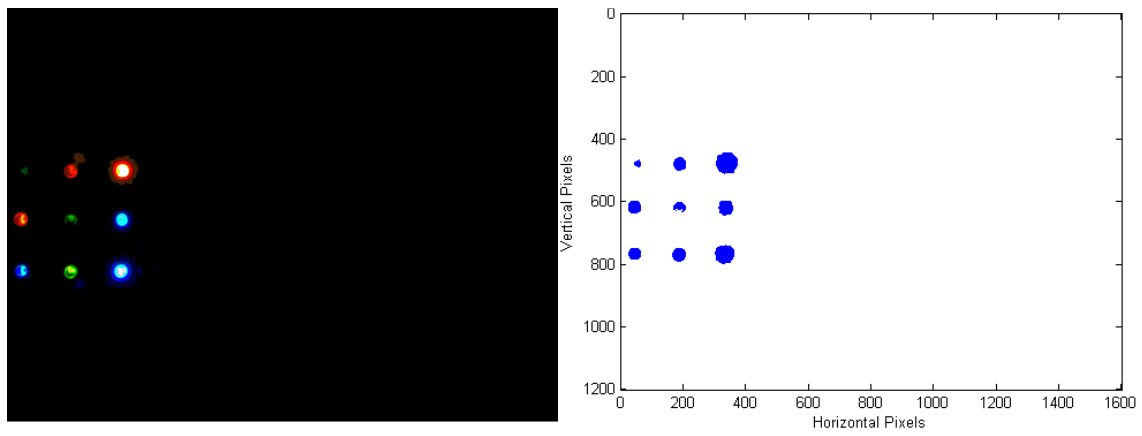
(c) 10% Intensity Threshold

Figure 37: Star Recognition Thresholding

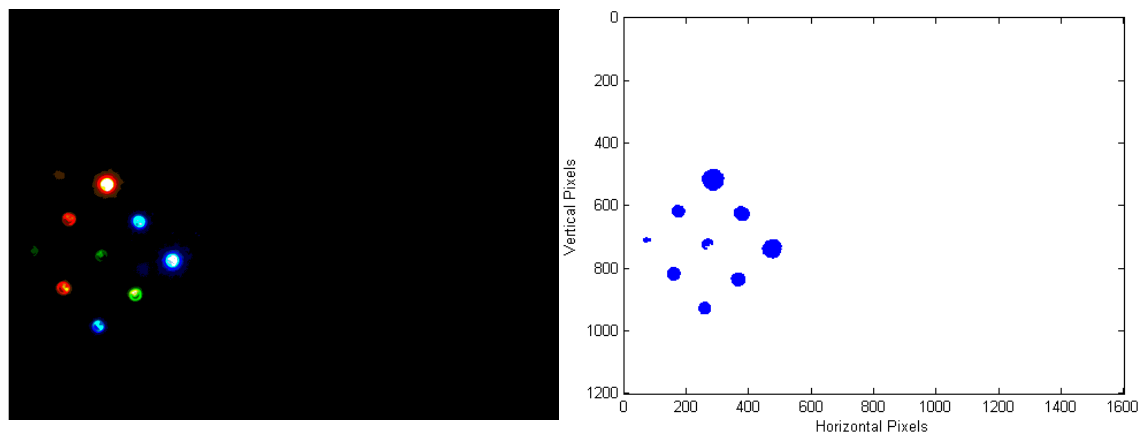
Figure 37 (a) shows the results of a 2% intensity threshold. Sensor noise and glare are clearly visible here. With an intensity threshold value increased to 25%, the sparsity matrix is noticeably cleaner, as shown in Fig. 37 (b). However, the dimmest LED failed to meet threshold requirements, and dimmer discernable features from other LEDs were removed, thus giving dimmer LEDs a non-circular shape. With a 10% intensity threshold, the majority of the noise was cleared up in Fig. 37 (c), and most of the characteristic roundness of the LEDs was maintained. If the area threshold filter of 50 pixels was subsequently applied to this image, the remaining discontinuous portions of the LEDs that were not larger than 50 pixels in area would be removed. Overall, these settings resulted a balance between noise filtering and feature preservation.

After the camera and algorithm settings were refined, multi-positional imagery was recorded to determine any LED brightness variations as a function of the star tracker's viewing angle relative to the patch board. Recalling that Position 1 is pictured in Fig. 36 (a) and Fig. 37 (c), analysis for three other positions proceeded in a similar manner. Figure {fig:MultiPosColor presents a simplified analysis.

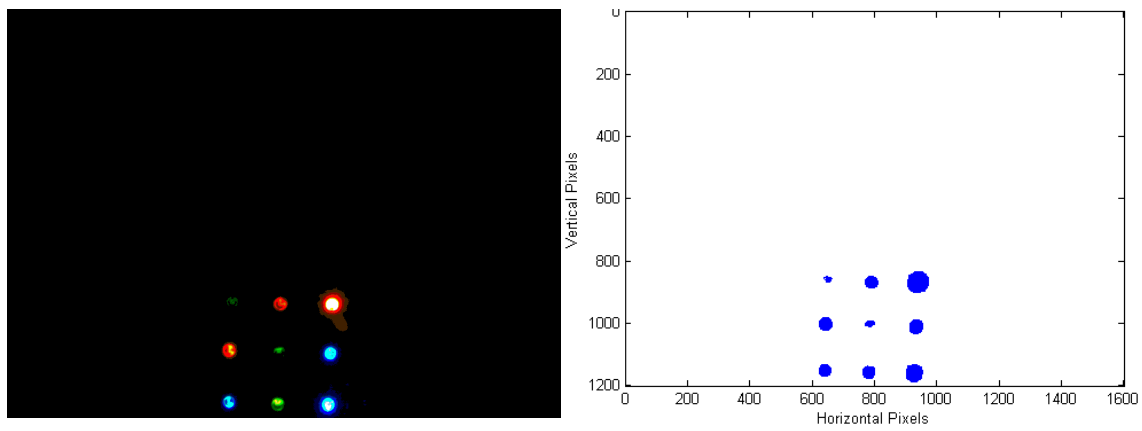
From Fig. 38, there is a marked difference in pixels passing the intensity threshold for the dimmer LEDs. The directional nature of these LEDs is evident from Fig. 34 (a), where the internal features of the LED are clearly visible when looking straight down the epoxy LED lens. However, when the viewing angle to an individual LED is offset from the axis of the LED lens, direct view into the LED is reduced. Therefore, the clear, raised-dome LED lens produces far too directional of a light emission with dimmer LEDs, which would place a limit on the lower end of the range of usable brightness values. For this research, it was desirable to operate the LEDs in as dim of a mode as can be accurately discerned by the star tracker. Therefore, more diffuse LEDs were preferred.



(a) Position 2



(b) Position 3



(c) Position 4

Figure 38: Multi-Positional LED Brightness Variations

Instead of immediately sourcing new LEDs, the Lumex LEDs that were already mounted on the patch board were lightly hand-sanded with fine-grit sand paper in order to produce a more diffuse LED lens. Figure 39 is a photograph of the resulting patch board.

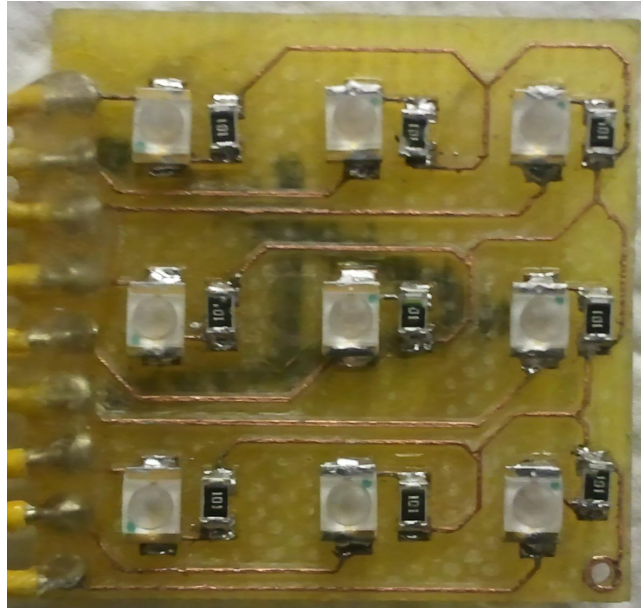
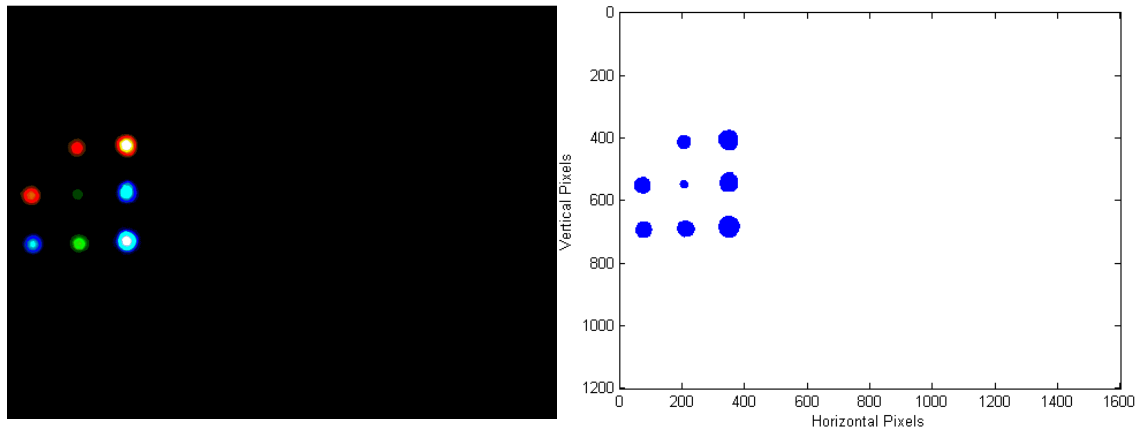


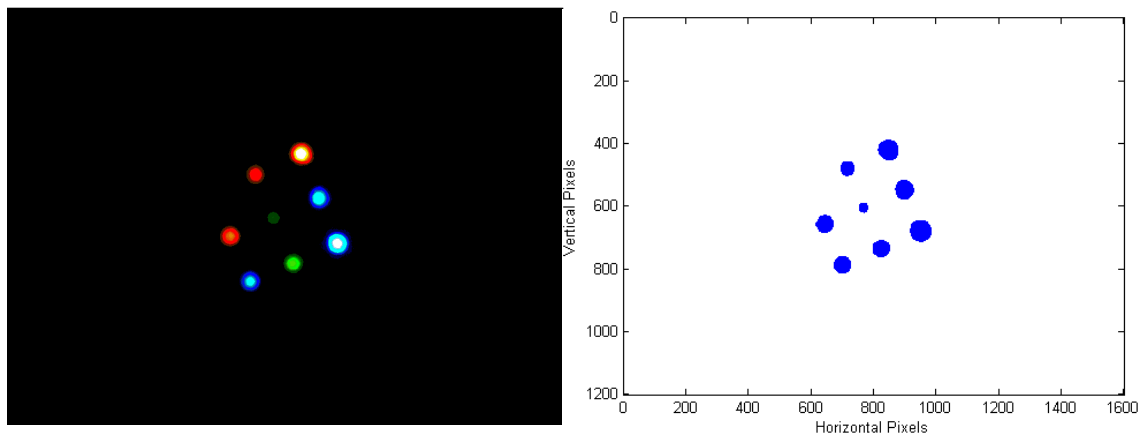
Figure 39: Patch Board with Sanded LEDs

With the LEDs sanded, the patch board was replaced on the test stand for further analysis. Prior to multi-positional imaging, it was determined that the diffuse light emitted from the dimmest LED was too dim at the current aperture and exposure settings. After a slight increase in camera aperture and exposure to collect more light, the remaining dimness characteristics required a reduced intensity threshold value of 4% to be used. With these settings, a new set of images were taken from different viewing angles. The images were finally passed through the intensity threshold filter as shown in Fig. 40.

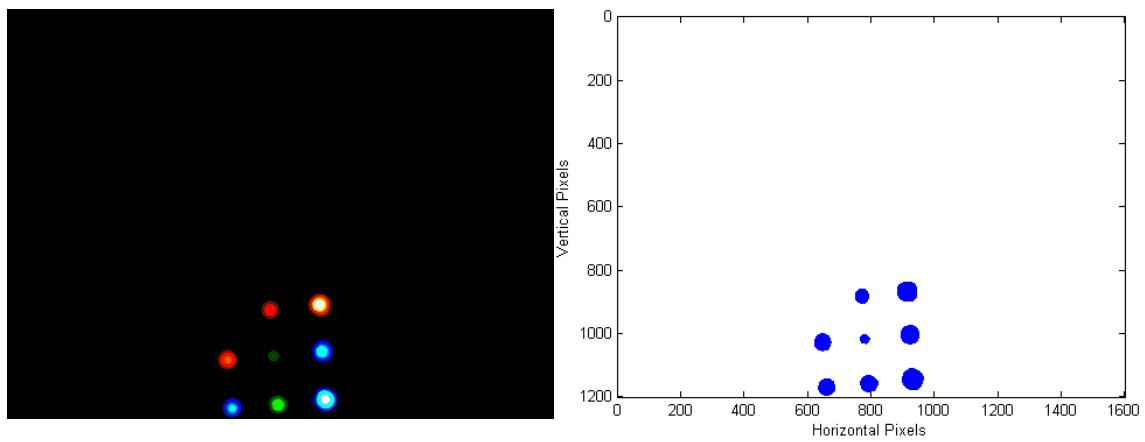
From examining Fig. 40, two key results are noted. First, the diffuse LED lens coupled with the camera and algorithm settings resulted in reasonably consistent LED pixel areas for all viewing positions, with very little noise. Second, the brighter



(a) Position 1



(b) Position 2



(c) Position 3

Figure 40: Multi-Positional Brightness Variations of Diffuse LEDs

LEDs show increased internal color saturation. When an LED exhibits more color information, it translates into more intensity information for that particular LED, which is critical since the goal is for each LED to have a distinct, consistent, and recognizable measure of magnitude. However, none of these early tests indicate that the camera sensor is more sensitive or noise-prone to any specific LED color. Thus, the critical parameter is therefore the overall intensity of the LED, which can be exhibited by any color LED. With this knowledge gained, attention was then focused on a suitable method to power the LEDs.

3.4.2 LED Controller. The voltage source for the LEDs used during the previous analysis was an Arduino Mega 2560 microcontroller board, outputting 5 V DC and a maximum of 50mA of current to each LED. It has a total of 54 digital input/output pins, and is interfaced to a personal computer via USB 2.0 connection. The Arduino Mega was chosen to power and control the LEDs because of its C-based open-source programming software and the large number of digital pins. By selecting the appropriate pins via the programming software, the desired LEDs from the patch boards may be selectively powered. A photograph of an Arduino Mega is shown in Fig. 41.



Figure 41: Arduino Mega 2560

The major drawback to this method of powering the LEDs is that the voltage signals are digital, thus fixing an LED's light output to depend only on its inherent light emission characteristics and the resistor to which it is paired. This system is highly inflexible and thus a software-controllable method was desirable. The Arduino Mega is capable of digital pulse-width modulation (PWM). PWM of a digital source voltage would enable analog-like control of the current passing through the LEDs by controlling the proportion of ON time to the cyclic period, or duty cycle, of voltage through the LEDs. In other words, the proportion of the duty cycle to the total cycle time is what determines the average voltage. Figure 42 illustrates this principle.

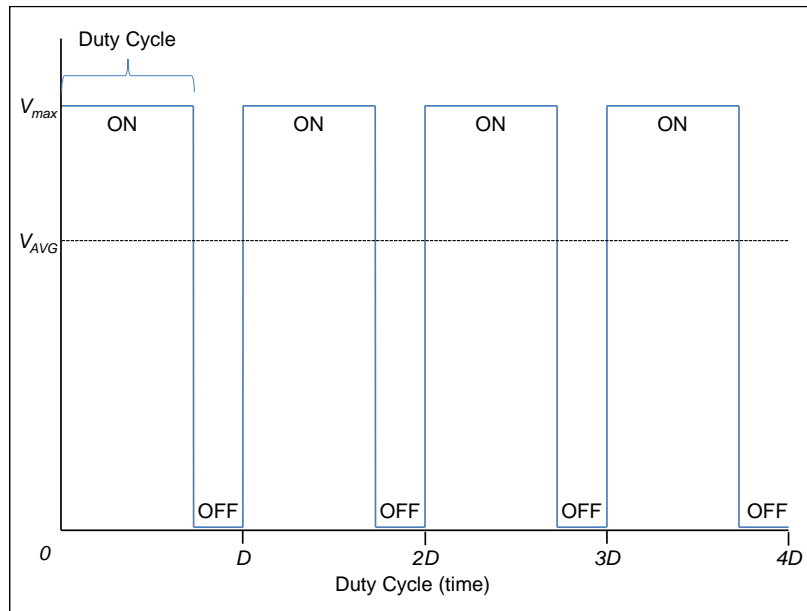


Figure 42: Simplified PWM Graph

For a PWM-driven rectangular pulse wave with a duty cycle D , period T , and digital voltage V_{max} , the average voltage V_{AVG} is defined by

$$V_{AVG} = DV_{max} \quad (35)$$

where D is defined as

$$D = \frac{t_{on}}{T} \quad (36)$$

Implementing PWM using the Arduino board produces a challenge; only fourteen of the Arduino Mega's digital output pins are true PWM-capable. The star field above SimSat would require far more than 14 LEDs. However, the Arduino Board's 54 digital pins can be manually programmed to perform under PWM by including the appropriate ON and OFF delays in the programming code. Each programmed action performed by the microcontroller is represented by a line of code, therefore each action performed on each LED is sequential, resulting in a new *effective period* governing the LEDs' ON/OFF cycle. Each LED is then activated, delayed, deactivated, and delayed, one LED after the other, effectively shortening the duty cycle since the OFF time is now a function of the number of LEDs being utilized within the code. Thus, assuming no additional delays from the microcontroller, the effective duty cycle for the i^{th} LED, $D_{eff,i}$, is now defined as

$$D_{eff,i} = \frac{t_{on,i}}{\sum T_n} \quad (37)$$

where $t_{on,i}$ is the ON duration for the i^{th} LED and $\sum T_n$ is the sum of the periods of all n LEDs. A critical consideration using this method of PWM then becomes an issue of timing. If the camera exposure setting is set too short, flicker may be noticeable depending on the effective duty cycle of the LED. Additionally, more LEDs being controlled by the microcontroller decreases the effective duty cycle by increasing the effective period. After some initial checks of the concept on the patch board with all the resistors changed to 100 ohm resistance values, it was found that a 1,000 microsecond period for each LED was acceptable. Using a multimeter, the average input current

values produced ranged between 0.05 mA to 2 mA. While some flicker effect was noticed in this early analysis, the effect was negligible and will be analyzed in greater detail in later experiments. The check proceeded after a slight increase in the camera aperture and an intensity threshold setting of 12%. The results are shown in Fig. 43, where the $t_{on,i}$ for each LEDs (1 ms, 500 ms, and 1,000 ms), is displayed next to the corresponding LED in the image.

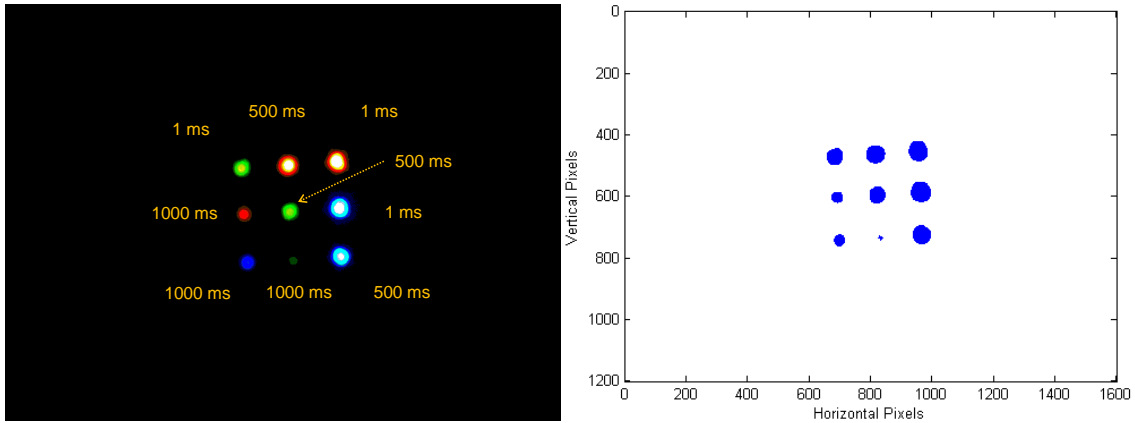


Figure 43: PWM Analysis on Color LEDs with Duty Cycles Displayed

After preliminary studies of the LED configurations and the method to control them, critical insight was gained. The aperture and focus settings, adjusted in tandem, worked to filter and smooth out much of the light producing unwanted noise prior to entering the sensor. The camera's exposure setting allowed for control of the overall image brightness, while the intensity and pixel area threshold settings within the algorithm acted as the first step in star identification logic, as well as a second filter against noise. Finally, the LED lens properties were found to be a consideration for the LEDs.

3.4.3 Final LED Sub-System Concept. Using the knowledge gained from Sections 3.4.1 and 3.4.2, it was determined that the next step would be to utilize a more star-like LED that behaves more like a point source of light. Several LEDs

on the market exhibit Lambertian light emissions without the need to sand the lens. Furthermore, it was determined that the camera sensor did not favor a specific color LED to a large enough degree for the purposes of this research effort. With the use of PWM, the additional utility of using different LED colors to add a second degree of intensity variation was no longer applicable.

The LEDs selected for the formal portion of this research effort were Everlight 67-21/XK2C PLCC2 White 5075K LEDs. While slightly larger than the previously studied LEDs and with a lens that is mostly flat, their light output is considerably more Lambertian. The radiative pattern of these LEDs is shown in Fig. 44.

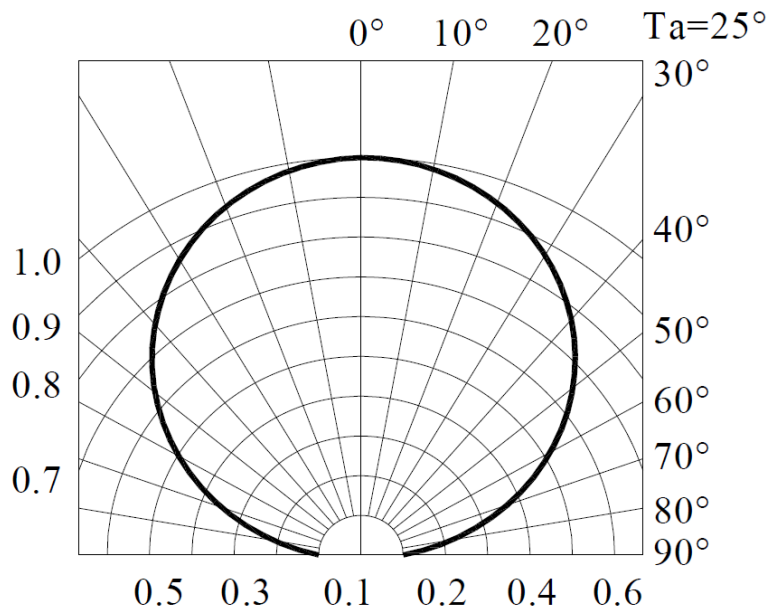


Figure 44: Final LED Radiation Pattern Plot

Since different LEDs were utilized, new patch boards were constructed. The new boards maintain the spacing and general configuration of the previous patch boards, with the major difference being their 1.25 inch×1.25 inch square dimensions. With the new LEDs in combination with PWM control, 390 ohm resistors were coupled to all LEDs. With the electronics installed, the patch boards were painted a flat black. Additionally, because the LED lenses are larger in diameter than the previous

LEDs, the lenses were masked to reduce the effective diameter of the lenses with the intention of producing smaller point source-like light sources. Figure 45 is a snapshot taken during final preparation of one of the patch boards.

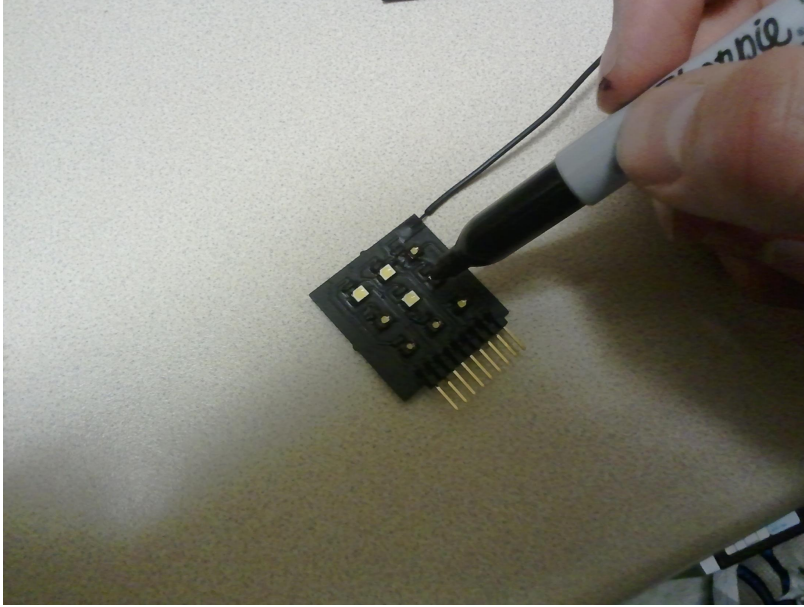


Figure 45: Final Patch Board Preparation

After the new patch boards prepared, one was mounted and given a preliminary test to verify the concept. By this point, the star field surface, discussed in detail in the next Section, was installed over the SimSat air bearing pedestal, so that the patch board was located 48 inches over the SimSat pedestal, or approximately 33 inches from the camera sensor. The preliminary test of the patch board LEDs was performed using the same PWM values and camera lens settings as in the previous analysis. However, the camera exposure was set to a moderately shorter setting, while the intensity threshold was set at 4% in order for the algorithm to pick up the dimmer pixels. Figure 46 depicts the results from this preliminary analysis. With the LED concept verified, the next focus of discussion is the star field surface to which the LEDs will mount to.

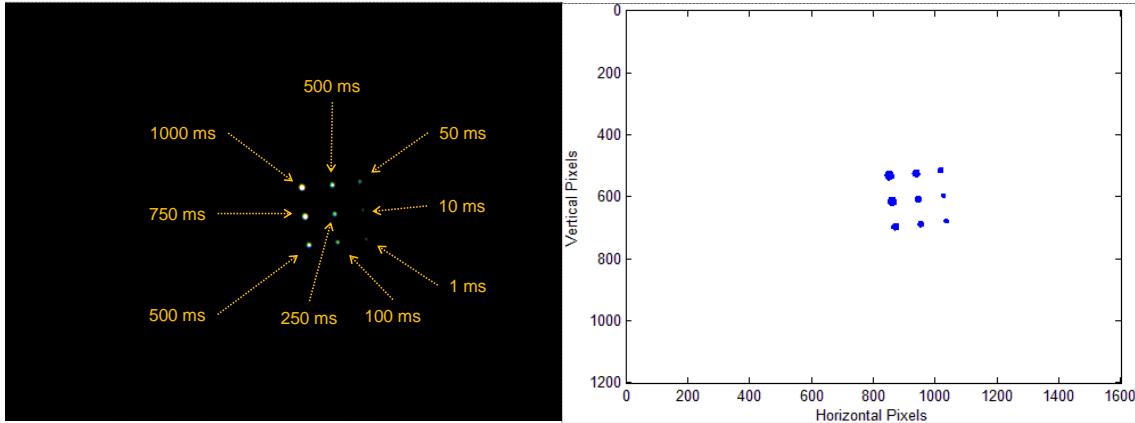


Figure 46: PWM Analysis on White LEDs with Duty Cycles Displayed

3.5 *Star Field Surface Development*

Since the decision to use LEDs occurred early on in this research, efforts had to be made in determining the proper surface to mount the star-representative LEDs. In Section 3.2, analysis showed that a flat surface has definite limitations. These limitations will be analyzed before examining the spherical surface approach adopted in this research effort. With the desired surface determined, this section will conclude with the discussion of the specification, production, and installation methodology for the chosen surface.

3.5.1 Flat Surface Analysis. The critical aspect of using a flat surface mounted at some fixed distance from the vehicle is that the distance between the camera and the observed portion of the star field within the FOV is constantly changing with respect to the vehicle’s attitude. With these changing distances, the apparent distances between the imaged objects will appear to vary from different orientations, even if the actual linear distances on the star field are the same. This scenario is illustrated for the simple “top-down”, two-dimensional case in Fig. 47, where the camera is mounted at some fixed position M away from the vehicle’s center of rotation, with the bore-sight orthogonal to the rotational axis and the star field located a distance R from the

center of rotation. The camera has a constant FOV ϕ , and the vehicle's orientation (typically unknown in the attitude determination case) is defined by a generic Euler Angle Ψ . The star groupings on the star field are set up such that the red and blue stars, separated by a linear distance c , are at the edges of the camera's FOV when Ψ equals zero. The distance c thus represents the length of the image frame projected at the star field surface. Finally, the green star is placed at some distance e external to the FOV occupied by the red and blue stars.

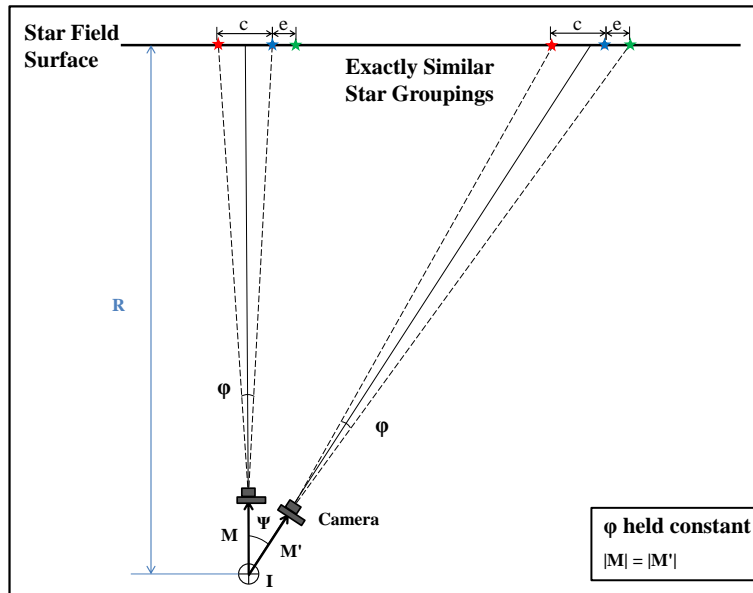


Figure 47: Flat Surface Geometric Analysis

If the same grouping of stars is simply slid down the surface of the surface, maintaining the same relative distances c and e , and the vehicle is rotated some angle Ψ in order to capture the stars, it would find that all three stars now fit in the FOV. Thus, if the red and blue stars at the first position were defined with an angular separation of ϕ with respect to the camera frame, they no longer have that angular separation when viewed from a different relative position.

This places a detrimental effect on using the camera frame's preset (H, V) coordinates to build unit vectors for measuring and comparing the angular separations

between star pairs, as discussed in Section 2.3.4. Figure 48 depicts a close-up view of this effect at the second position described in Fig. 47, where the hashed red line represents the image plane, normal to the boresight and projected at the intersection of the inner-most FOV vector and the star field (the location of the red star). The vectors representing the projection rays of the objects on the star field to the focal point are represented, as well as the projected objects on the image plane. The red dots represent generic points in the image, while the stars represent the same star mentioned in the previous paragraph and their projections on the image plane.

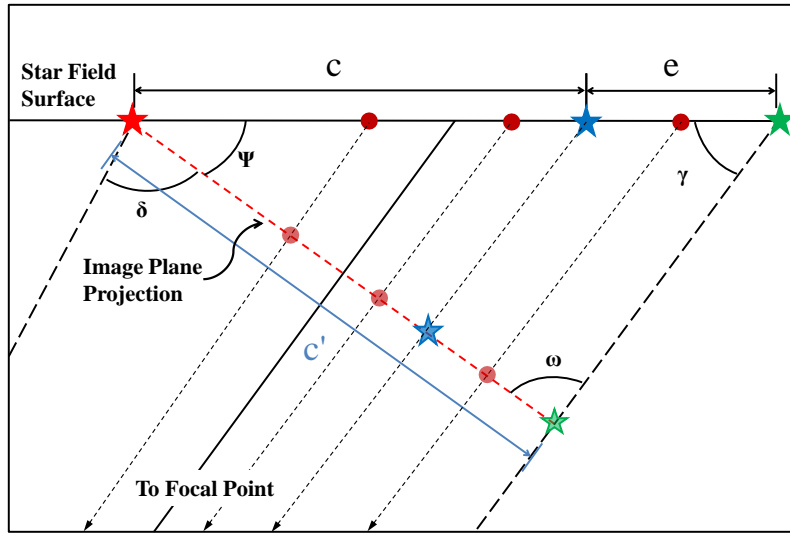


Figure 48: Flat Surface Image Plane Analysis

Examining the image plane, we see that it is the base of the triangle defined in part by the angle Ψ and the sum of the lengths c and e . The width of the image plane c' is then clearly dependent on Ψ , and can be expressed using the geometry from Fig. 47 as

$$c' = 2 \left(\frac{R - M \cos(\Psi)}{\cos(\Psi - \frac{\phi}{2})} \sin \frac{\phi}{2} \right) \quad (38)$$

and the angles γ , δ , and ω can be defined as

$$\gamma = \left(\frac{\pi}{2} - \frac{\phi}{2} - \Psi \right) \quad (39)$$

$$\delta = \left(\frac{\pi}{2} + \frac{\phi}{2} \right) \quad (40)$$

$$\omega = \left(\frac{\pi}{2} - \Psi \right) \quad (41)$$

Thus, the image plane coordinates are seen to depend on the Euler Angle Ψ . To examine this effect, we let R equal 48 in, M equal 14 in, and ϕ equal 10.45° and we imagine a scenario where the vehicle will track the star group as it slides across the star field surface. If the scenario begins at Ψ equal to zero and we begin to slide the star group to the right, the vehicle will rotate such that the red star is maintained at the leftmost part of the camera's FOV. Once the Euler Angle Ψ equals 30° , the stars stop sliding and the scenario ends. During the scenario, the following data was recorded in Table 1.

Table 1: Image Plane Dimension vs. Vehicle Orientation - Flat Star Field

Ψ (deg)	c' (in)	% Diff c, c'
0	5.94	0
10	5.98	0.65
15	6.1	2.63
20	6.3	5.78
25	6.57	10.02
30	6.94	15.4

Table 1 presents the length of the image plane as a function of Ψ , as well as the percent difference between the original length of the image frame at the first position

c versus that of the projected image frame c' . It shows that the image dimension has effectively stretched, introducing vector mapping errors. Therefore, a different approach was needed that removed any dependency on Ψ .

3.5.2 Spherical Surface Analysis. With an understanding of the limitations of the flat surface approach, as well as knowledge of the pinhole camera model, the next obvious surface shape to analyze was the spherical shape. If the previous example were reset, this time with a curved star field surface with center of curvature coincident at the vehicle's center of rotation, it would look as shown in Fig. 49, where R is the fixed radius of the curved surface, M is fixed camera mount position, the red and green stars lie at the outermost points of the camera's FOV ϕ , and S is the arc-length of the curve enclosed by them.

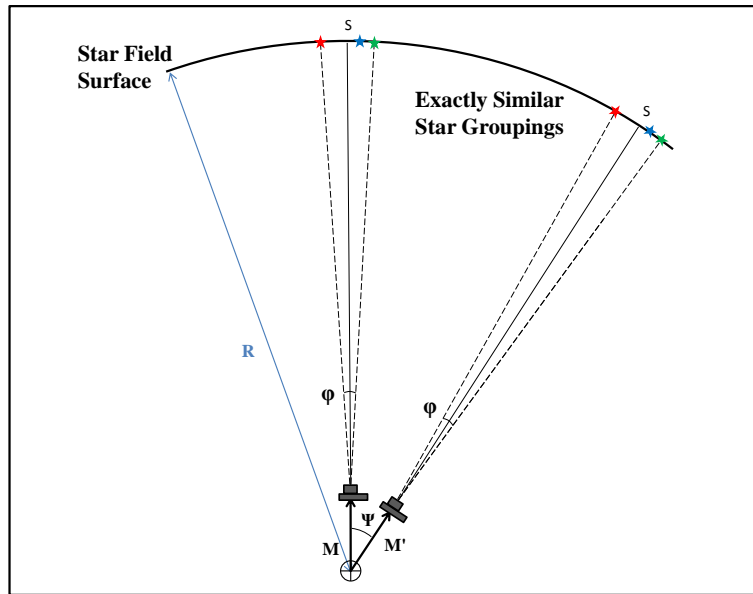


Figure 49: SphericalSurface Geometric Analysis

If the same tracking scenario were repeated by sliding the stars across the curved surface together, it would be seen that the length of the projected image plane c

would not change, since the chord c is defined for a curved surface by

$$c = 2R \sin \frac{\theta}{2} \quad (42)$$

where θ is the effective FOV angle measured from the center of curvature, depicted by the green hashed lines in Fig. 50.

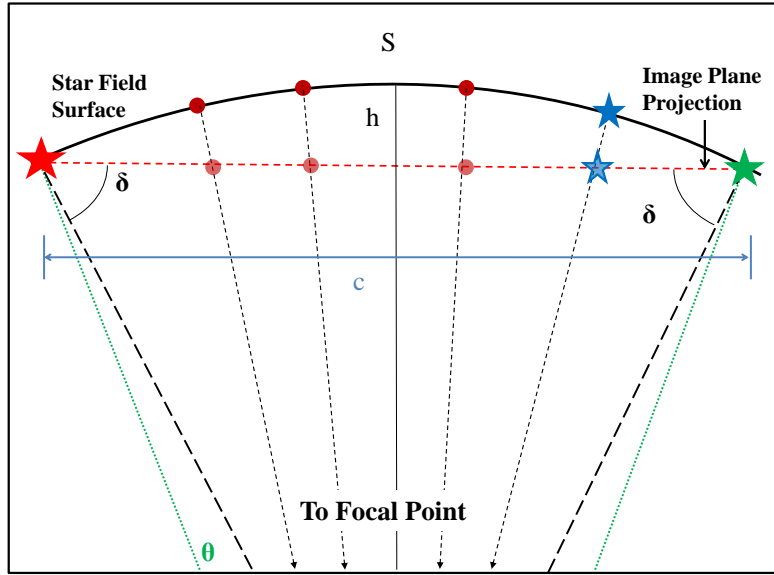


Figure 50: Spherical Surface Image Plane Analysis

Thus, for a spherical surface with a constant radius and mounted with its center of curvature set at SimSat’s center of rotation, the projected image plane dimensions remain consistent for all orientations. With a large enough radius relative to the FOV, the height h of the arc S is kept sufficiently small to allow for an approximation that all imaged LEDs correspond to inertial frame vectors having a unit length equal to the radius of the spherical surface. With the analysis of the desired spherical surface complete, the next step was to specify and produce the surface.

3.5.3 Dome Specification and Production. To provide a complete star field surface that encompassed all possible SimSat orientations, a hemispherical dome con-

cept was adopted. Hemispherical domes are widely available on the market, with most made of acrylic. These acrylic domes are manufactured via vacuum forming, where a heated sheet of acrylic is placed over a vacuum chamber. When vacuum is formed, the heated acrylic will be drawn into the chamber and shape itself into the contours of a dome. Some methods utilize a precision-made mold in the vacuum chamber to shape the dome to exact specifications. Domes formed without a tailor-made mold are known as free-vacuum formed.

Due to the exploratory nature of this research, a costly mold-formed dome was not desired. Instead, a cost-effective acrylic free-vacuum formed dome was sourced from the market. The critical dimensions given to the manufacturer were the diameter and height of the dome, which were specified at 62 in and 11.50 in, respectively. The height specification had a manufacturer's tolerance of ± 0.25 in due to the free-vacuum forming process. Another production trait of all vacuum-formed domes is that the dome thickness varies from the outer diameter of the dome to the inner portions of the dome due to the material stretching unevenly to form the dome shape. For shallow domes, such as the specified dome, the variation is small.

The dome specifications communicated to the manufacturer and the associated expected dimensional variations resulted in a dome design with the following characteristics (in British Standard units):

- Outer Diameter: 62 in
- Dome Height: 11.50 in (± 0.25 in)
- Spherical Radius: 48.135 in (nominal)
- Angular Coverage: 80°
- Outer Flange Length: 1.5 in
- Dome Material Thickness at Base: 0.25 in

- Dome Material Thickness at Apex: 0.2036 in (approximately 80% difference)
- Interior Surface Area: 3384.41 in²
- Weight: 37 lbs
- Volume: 854 in³

Figure 51 illustrates the dome design using SolidWorks. The thickness variation results in a small variation of the inner surface radius from the apex to the edge. The expected shape of the interior surface of the dome is therefore not perfectly spherical but a prolate spheroid, with a semi-minor axis x_{minor} equal to 47.98 in in the horizontal and a semi-major axis x_{major} equal to 48.03 in in the vertical, also shown in Figure 51. Since the dome's angular coverage is 80° total, the radii only varies from 48.033 in to 48.010 in, or less than 0.05% difference.

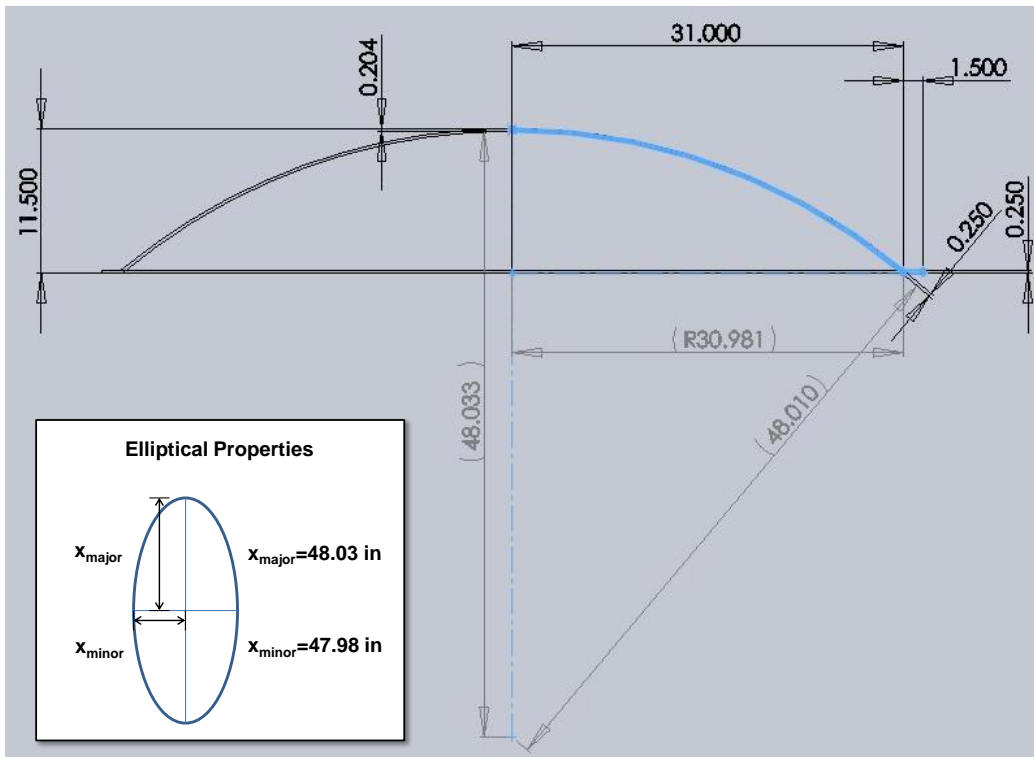


Figure 51: Hemispherical Dome Design Sketch

After the dome was received from the manufacturer, the inside surface was sanded and painted flat black in order to mask out the overhead lighting of the surrounding laboratory, as well as to provide a not-reflective background for the LEDs. During the installation process, discussed in the next section, the dome was precision measured to determine its conformity to the design specifications. While some radial variation was expected, too much surface variation could introduce image projection inconsistency, albeit to a smaller degree than with the flat surface case. Figure 52 depicts the resulting measurement of the interior dome surface as compared to the design specification.

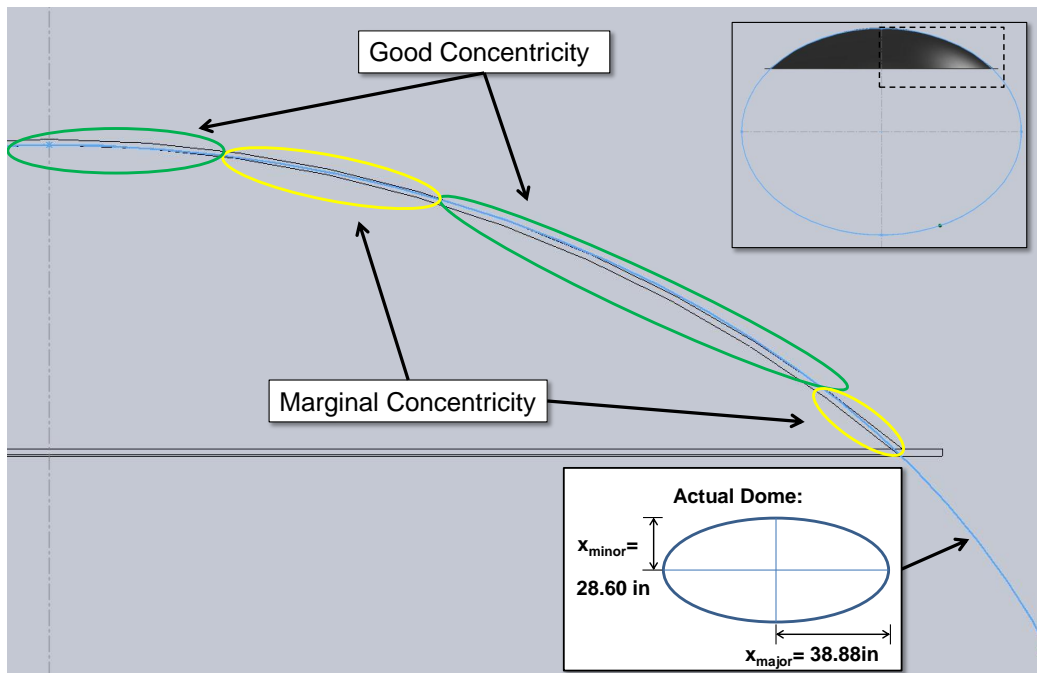


Figure 52: Dome Sketch with Actual Contour Measurement Overlayed

The results of the preliminary measurements showed that the actual surface did not completely conform to the design dimensions for the interior surface, evidenced by the blue line beginning at the apex point of the inner dome surface. Tracing the

blue line from this point, it soon crosses through the thickness of the designed dome, turns back downward in concentricity with the design dome outer surface, before again crossing through the design dome notional surface. The approximate elliptical dimensions describing the actual dome inner surface contour are a semi-minor axis x_{minor} equal to 28.60 in in the vertical and a semi-major axis x_{major} equal to 38.88 in in the horizontal. This corresponds to percent differences of d_v of 50.71% and d_h of 20.95%, where d_v and d_h are percent differences corresponding to the values of the vertical and horizontal semi-major axes, respectively. Section 3.7.2 discusses the methodology used in this research to evaluate the dome surface.

3.5.4 Dome Installation and Measurement. Mounting the dome required precision measurements of the dome's finished dimensions to insure the apex of the dome was closely centered over the air bearing pedestal. Once the dome and the support frame were roughly mounted over the desired location, a FARO Arm precision measurement tool was utilized to precisely locate the dome. The first component that was measured was the air bearing cup, since the center of the cup is defined as the center of the SimSat inertial frame. Once the center of the spherical cup was found in three-dimensional space, the coordinate reference system within the measurement program was set at this point. All subsequent measurements were then made with respect to this inertial origin. The cup was found to have a radius of approximately 4.33 in, which matched the known specifications of the air bearing. Figure 53 shows the cup being measured with the FARO Arm probe.

With the inertial coordinate system set, the next step was to position the dome's radial center as close as coincident with the inertial reference frame as possible. This was done by measuring the inner surface of the dome, at which point the software computes a central point to the approximated sphere being measured. Figure 54 shows a photograph of the dome surface being measured.

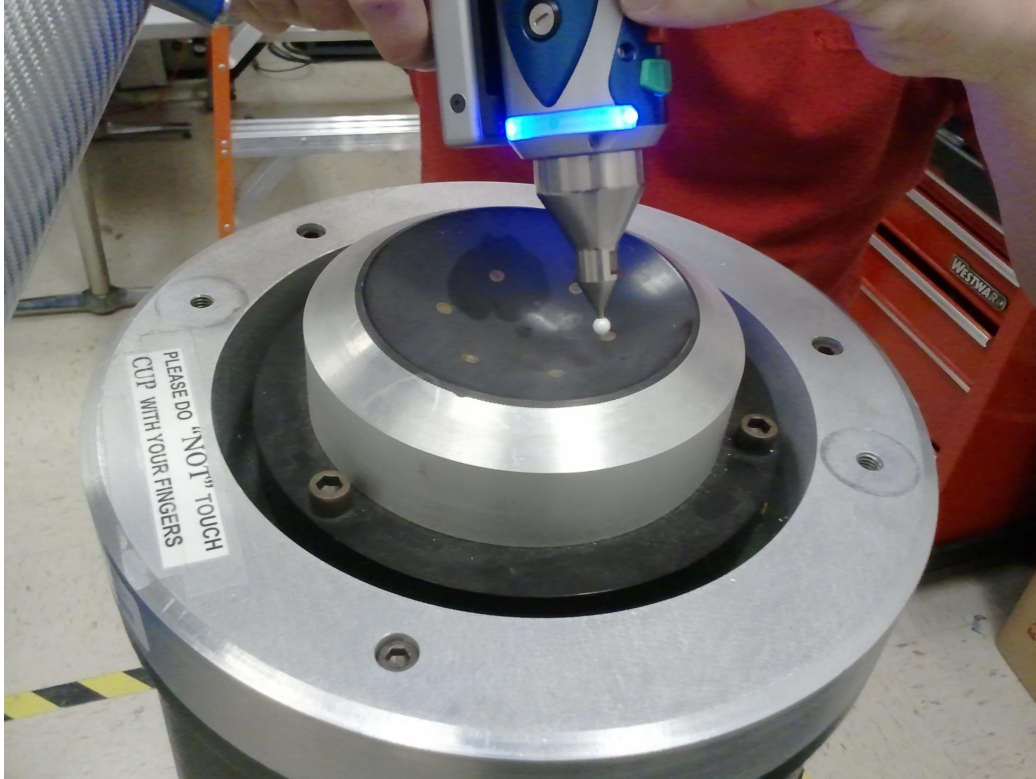


Figure 53: Spherical Air Bearing Cup Measurement

The differences between this central point and the inertial origin previously measured are the remaining adjustments to be done in the x and y directions. Once these slight adjustments were complete, the dome's position was measured one final time. It is important to note that even with the differences between the design and actual dome radii, such difference was judged to be minor since the overall shape of the actual dome conformed well enough to the design specifications. Therefore, the apex of the inner surface of the dome was placed within 0.125 in centered and approximately 48 in above the inertial origin.

In order to center any of the patch boards onto the dome, a visual indicator was necessary to locate the apex of the dome. To aid in this, a 3-axis laser level was placed over the cup so that the negative z-axis laser indicator was located over the lowest point of the cup. This centered the laser level and allowed the positive z-axis



Figure 54: Dome FARO Arm Probing

laser to indicate the intersection of the inertial z-axis and the the dome. The laser level is shown resting on a clear acrylic plate and indicating the apex of the dome in Fig. 55.

With the dome mounted, measured, and precision located, the star field is ready for mounting and wiring the LED patch boards. However, the next discussion will focus on the development of the star pattern recognition and attitude determination algorithm that will rely on the configuration of the patch boards and their placements on the dome.

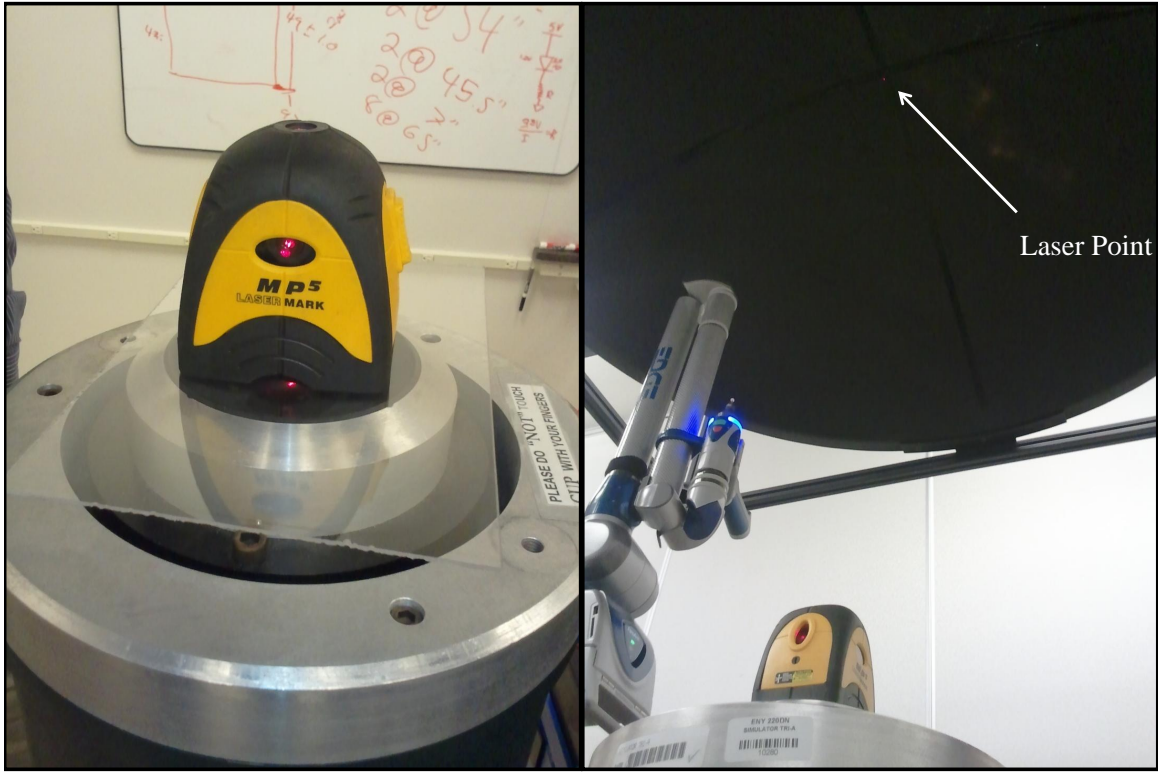


Figure 55: Laser Level Alignment and Apex Location

3.6 Matlab[®] Algorithm

The algorithm described in this section is based largely on the Boeing SAA algorithm discussed in Section 2.4.2 by Needelman (14). The following are the variations implemented for this research effort.

3.6.1 Configuration. The first step involves setting key configuration parameters used by the other portions of the algorithm. These include camera settings, star detection settings, star catalog size Δ , and physical configurations such as the dome radius and LED spacing. The position in meters and the orientation of the star tracker reference frame with respect to SimSat body frame in Euler Angles is also set.

3.6.2 Common Functions.

3.6.2.1 Star Detection. The first portion of star detection was mentioned in Section 3.4.1.3, where pixel values were passed through intensity and area threshold values. The second portion of the star detection function is centroiding, in which a basic MATLAB[®] function is used for centroiding the pixel areas that passed the threshold test. The third portion assigns an instrument magnitude to each LED. MATLAB[®] readily reports an intensity value between 0 and 255 for each pixel in the converted gray scale image. However, with multi-pixel areas containing many pixels with varying intensity values, the average intensity of the pixels within the pixel area of the LED is computed, giving each LED a statistically smoother, characteristic magnitude. The magnitude is then normalized against the median LED area in the image to improve the spread of LED-specific instrument magnitudes.

3.6.2.2 Vector Mapping. Using the known values for the image frame dimensions and the 48 in radius of the dome, mapping the vectors to the LEDs in the camera frame can be done in a straightforward fashion. First, the LED pixel coordinates are transformed into camera frame spatial coordinates using the MATLAB[®] *cpt2tform* function. Then, using a variation of Eq. (9), the vectors in the star tracker frame can be mapped as follows:

$$\hat{v}_s = [x_s \ y_s \ z_s] \quad (43)$$

where x_s is a function of the set dome radius R and the camera mounting distance M , and is defined by

$$x_s = \sqrt{(R - M)^2 - y_s^2 - z_s^2} \quad (44)$$

From Eq. (44), the advantage of the spherical dome is demonstrated. With a known radius R and set mounting position M , closely approximating the observed LED

positions to lie on the surface of the sphere is facilitated. Additionally, converting the vectors in the star tracker frame to the body frame involves two steps: rotate the vectors using the known Euler Angle orientation of the star tracker frame, then add the position vector of the star tracker frame to the LED vectors. The resulting body frame vectors are used to compute the angular separations. This process is illustrated from left to right in Fig 56.

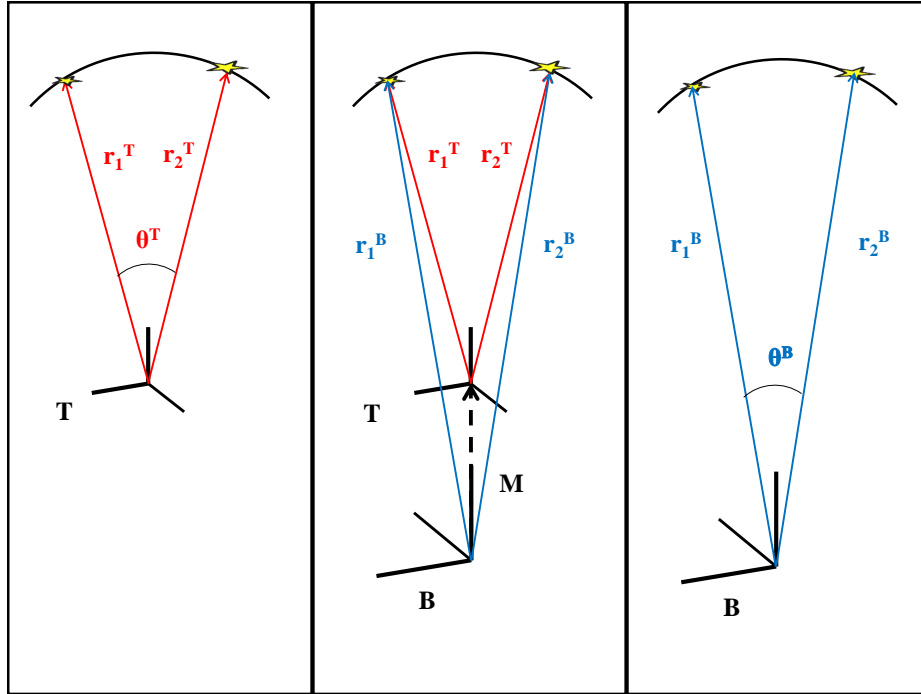


Figure 56: Algorithmic Vector Frame Transformation Illustration

3.6.2.3 Angle Calculation. Because the vectors now used are no longer unit vectors, the original equation to calculate the angular separation θ between two vectors, Eq (11), is now rewritten to apply to the non-unit vectors in the body frame as

$$\theta^B = \arccos \left(\frac{a^{\{\hat{b}\}} \cdot b^{\{\hat{b}\}}}{|a^{\{\hat{b}\}}| |b^{\{\hat{b}\}}|} \right) \quad (45)$$

It may be noted that using the angular separations between the tracker frame vectors would also suffice, as long as all angular measurements and comparisons are made with respect to the vectors in the same frame.

3.6.3 Calibration. Prior to taking measurements for star cataloging and tracking purposes, the algorithm must have reasonable error data with which to implement in the pattern recognition algorithm, as discussed in Section 2.4.5. Specifically, these are the Δm , $\epsilon_{separation}$, and $\epsilon_{position}$ values. However, instead of utilizing the covariance matrices from the QUEST algorithm to derive these values for ϵ , a basic statistical approach was instead implemented in the algorithm which assumes that the 1σ errors in measured LED separation and position are due to non-systematic, or random, noise which is approximately Gaussian. This assumption is critical, since errors caused by noise or distortions due to the camera optics, the imperfect spherical shape of the dome, or algorithm malfunctions should be systematic, and therefore may be distinguished from the random noise during analysis.

Similarly, the Δm , or threshold range of individually LED instrument magnitudes, was also assumed Gaussian; thus, the maximum of the calculated 1σ values of error for the LEDs is designated $\epsilon_{magnitude}$ in the algorithm. Also, from Fig. 32, it is expected that the distribution of angular measurements fall within a maximum of five separate ranges, since the 3×3 grid of LEDs is only capable of producing pair combinations having 5 distinct, measurable angular separations. Thus, the maximum of the 1σ values for the measured angles is the $\epsilon_{separation}$. $\epsilon_{position}$ is similarly determined for each coordinate component of the LED position vector. However, knowing that the physical configuration of the pattern board maintains an approximately 8 mm spacing between LEDs, any 1σ value greater than approximately 1.3 mm could confuse the algorithm if the direct match test fails, since $\pm 3\epsilon_{position}$ would place it within the error range of neighboring LEDs.

The calibration algorithm begins with inputting the current SimSat orientation read from the IMU in Euler Angles. If the position is the home position, the IMU is zeroed to establish a zero-orientation state in the inertial frame. The algorithm then records the LED magnitudes and maps the vectors in the body frame. Next, the body frame vectors are transformed into the inertial frame using the initial Euler Angles. The calibration algorithm will capture multiple images for the desired number of positions to determine the statistical values of the LED magnitude, LED position coordinates, and pair angular separations across the total number of recorded observations. Additionally, the first image recorded is used to calibrate the spatial (y, z) coordinates of the image frame to facilitate the transformation from pixel coordinates to the star tracker reference frame coordinates. Using a specified LED pattern with known LED spacing, the algorithm queries the user to pick the locations of the detected centroids of the appropriately spaced LEDs. An example is shown in Fig. 57.



Figure 57: Image Frame Calibration Screen

Since the horizontal and vertical spacing of the LEDs is known, the algorithm performs a linear projective transformation based on the relationship between the pixel coordinates of the centroids and the LED spacing. Four measurements are taken and averaged on this step. With the correct coordinate transformation information, calibration produces the standard deviation information for the three parameters, and concludes with the output and storage of the σ error data. Histogram plots for the numerous measurements are produced as well.

3.6.4 Cataloging. Cataloging the vectors begins with inputting the known SimSat orientation at the moment the image is taken, similar to the first step of Calibration. The major differences are the long-term storage of vector and magnitude information, as well as the creation of the PC discussed in Section 2.4.6. Since the system concept used in this research involves relatively few LED as compared to the space-representative versions, stars are sorted in the star catalog according to instrument magnitude, not declination.

3.6.5 Pattern Recognition. Other than applicable changes previously discussed, the pattern recognition algorithm proceeds as outlined in Sections 2.4.2, 2.4.3, and 2.4.5.

3.6.6 Attitude Determination. The QUEST algorithm is unchanged with respect to the description in Sec. 2.5.2 except that the estimated optimal quaternion is converted into a rotation matrix in order to perform the requisite vector transformations. However, it is noted that the current pattern recognition algorithm only utilizes two vector observations pairs, versus the full set of vector pairs it is capable of analyzing. Since the angle algorithm only analyzes two pairs of stars at a time, this utilization of the QUEST algorithm is appropriate.

3.7 System Validation

Three tests were conducted at the conclusion of this research effort in order to validate the concepts explored throughout the research. The camera lens and exposure settings were left unchanged from the settings used in the preliminary analysis discussed in Section 3.4.3; as a consequence, the laboratory lights were not dimmed. Similarly, the intensity threshold and pixel area threshold were held at 4% and 50 pixels, respectively.

3.7.1 LED Testing. Without consistent LED magnitude measurements, the algorithm logic would have a difficult time correctly matching the corresponding LEDs. Furthermore, since magnitude is the primary criteria for LED comparison in the angle algorithm, the efficiency by which the algorithm processes through the star catalog depends largely on the consistency of the stored magnitude information. Therefore, a test was necessary to determine the measurement consistency of the LED magnitudes. The test utilized a fixed pattern of 9 LEDs all controlled with PWM set at the maximum duty cycle of 1,000 microseconds. The patch board was kept at the apex location of the dome while images were recorded at five different SimSat orientations, or positions. Fifty images were recorded at each position for a total of 250 observations. Each of the 250 images were passed through the calibration algorithm, concluding with statistically analyzed data to determine the measurement distributions of magnitude, as well as position and angular separations. Figure 58 shows the setup for this test at position 1.

3.7.2 Dome Surface Testing. The utility of the complete system under investigation in this research effort wouldn't be fully realized unless the dome's physical characteristics allow for consistent magnitude and angular separation measurements. The quality of the measurements in this respect will depend on the consistency of

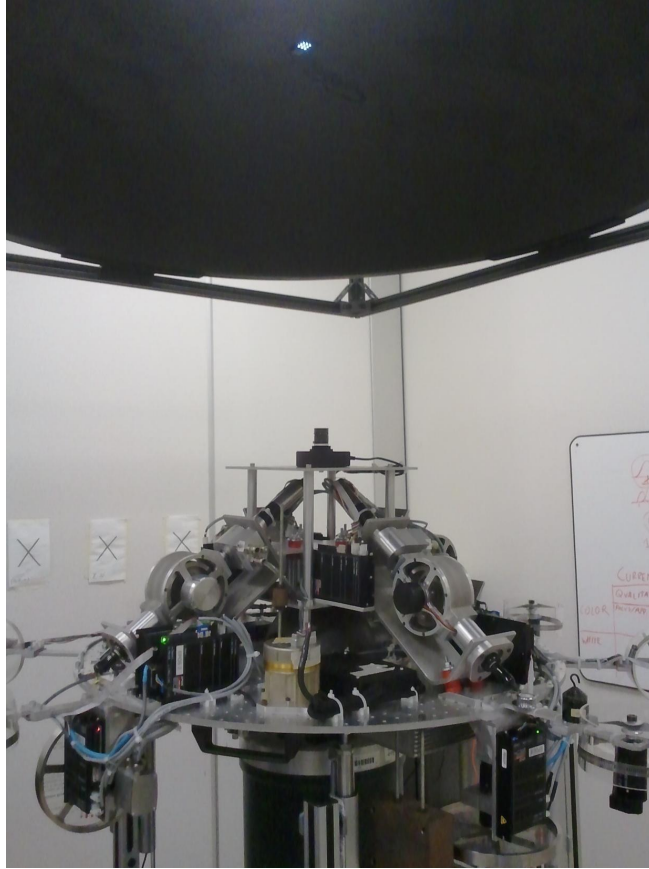


Figure 58: LED Test SimSat Position 1

measurement across the surface of the dome. To test this aspect, two LEDs were activated on a single patch board representing the maximum and minimum PWM settings of 1,000 microseconds and 1 microsecond. The same LEDs were imaged 50 times at three different locations on the dome, with each position's Euler Angles reported by the IMU inputted into the algorithm. For each position, the same patch board is imaged near the boresight to ensure that the true LED brightness and angular separations are maintained. Any systematic variations in the recorded LED magnitudes and/or the angular separations could then be attributed to the slightly ellipsoidal shape of the dome. Figure 59 depicts SimSat at Position 1 of this test, under the LED pair at the apex of the dome.



Figure 59: Dome Test SimSat Position 1

Similarly, Figure 60 depicts SimSat at Positions 2 and 3 of this test, under the LED pair repositioned at two points within the dome.

3.7.3 Algorithm Testing. In order to determine whether the measurements of the LED magnitudes, position vectors, and angular separations are usable for accurate star pattern recognition and attitude determination, a simple test of the algorithm was performed on a pattern of 5 LEDs with PWM settings of 1,000, 500, 400, 200, and 1 microseconds, respectfully. In this test, the objective was to measure and catalog the LED pattern from SimSat's home position, and verify that the algorithm was capable of matching the star data from different angular orientations and estimating an optimal quaternion to describe the orientation of the vehicle. A catalog size Δ of

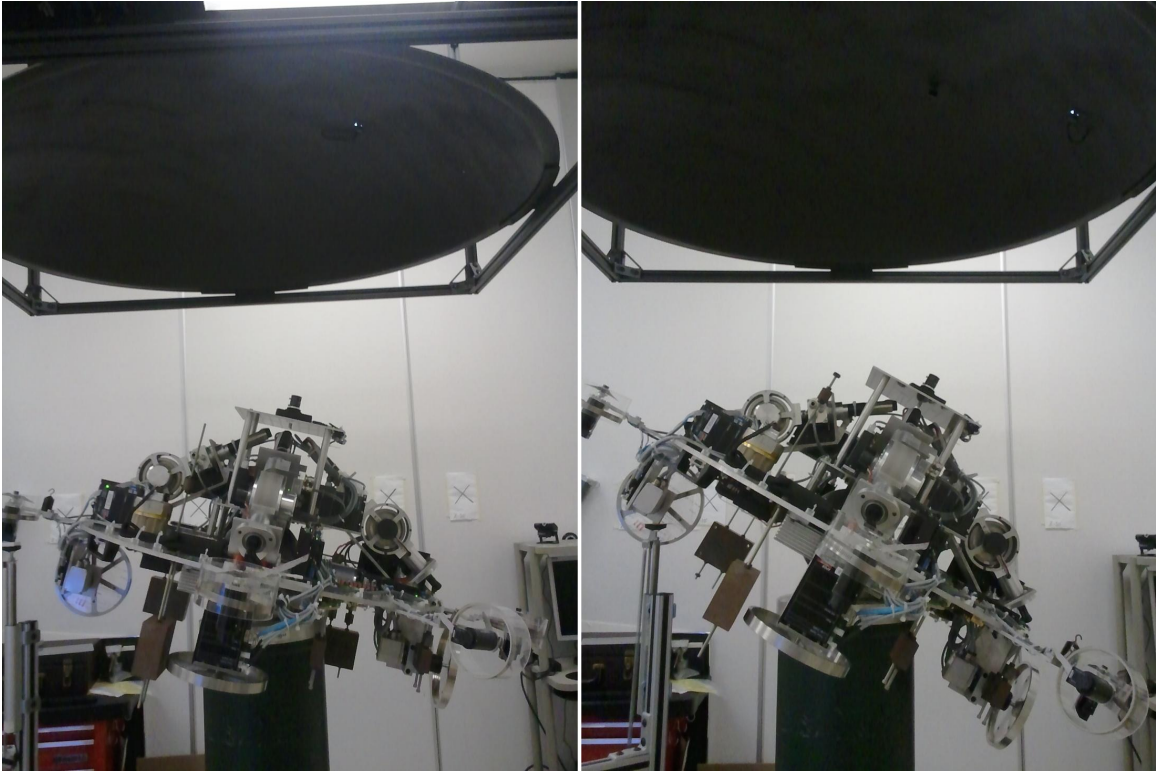


Figure 60: Dome Test SimSat Positions 2 (left) and 3 (right)

100 arcseconds was chosen for this test. The test was performed across 5 positions. Prior to the algorithm test, a similar procedure for calibrating the measurement system as detailed in Section 3.6.3 was implemented. No changes to the camera optics or star detection parameters were made. The test can then be described by the following procedure:

1. Configure the algorithm parameters, and specify a catalog size Δ
2. Calibrate the image across five positions to determine the $\epsilon_{magnitude}$, $\epsilon_{position}$, and $\epsilon_{separation}$
3. Set SimSat at the desired position and run algorithm to determine **A**
4. Set SimSat at new position and repeat Step three for all remaining positions.

5. Compare the estimated attitude to the IMU data previously recorded at each position.

Figure 61 shows SimSat at Position 1 for this test.

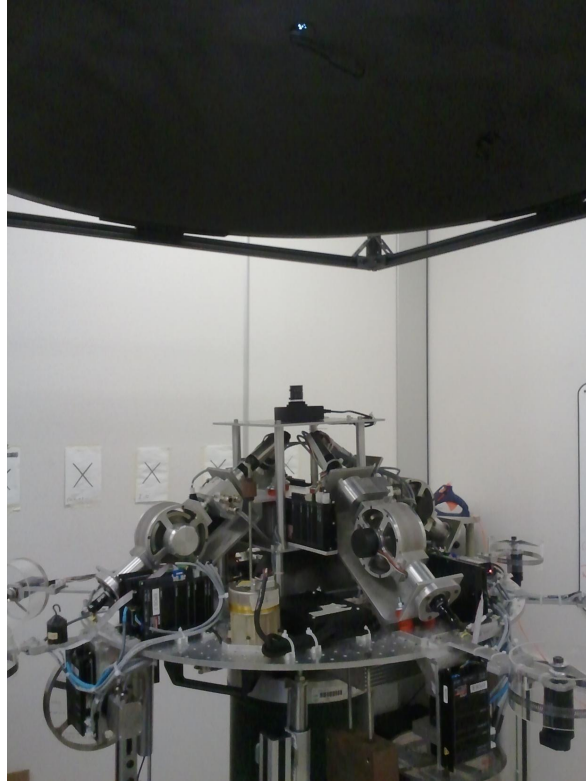


Figure 61: Algorithm Test SimSat Position 1

3.8 Summary

Chapter III presented the methodology used in the development, integration, and validation of the star tracker reference system concept for SimSat. The critical hardware and algorithmic considerations made were discussed in detail. Lastly, the testing procedures used to validate SimSat's newest external reference system concept was described.

IV. Results and Analysis

4.1 Introduction

Chapter IV presents the results and analyses of the concept validation tests described in Section 3.7, specifically:

1. LED Configuration Test (Test 1)
2. Dome Surface Test (Test 2)
3. Star Pattern Recognition and Attitude Determination Algorithm Test (Test 3)

The data was captured on the Mini-Box PC using MATLAB[®] scripts for experiment execution. This chapter presents a portion of the results of these tests, along with the accompanying analyses of the complete data collected. Additional results figures are provided in Appendix A.

4.2 Test 1 Results

This section presents the results of the LED magnitude consistency tests described in Section 3.7.1. The goal of Test 1 was to determine and characterize the variation in recorded multi-positional normalized instrument magnitudes of a representative sample of the LEDs used in the final system concept. Figure 62 depicts the recorded image at Position 1, while Fig. 63 shows the recorded images from the four remaining SimSat positions. The distribution of magnitude measurements assigned to each LED over the course of 250 total image collections is illustrated in Fig. 65; this data is then plotted on a single histogram in Fig. 65 to illustrate the overlapping measurements. Table 2 lists the averaged values for the LED mean magnitudes and standard deviations across all five positions. Additional histogram figures showing distribution data at each position can be found in Appendix A.1.

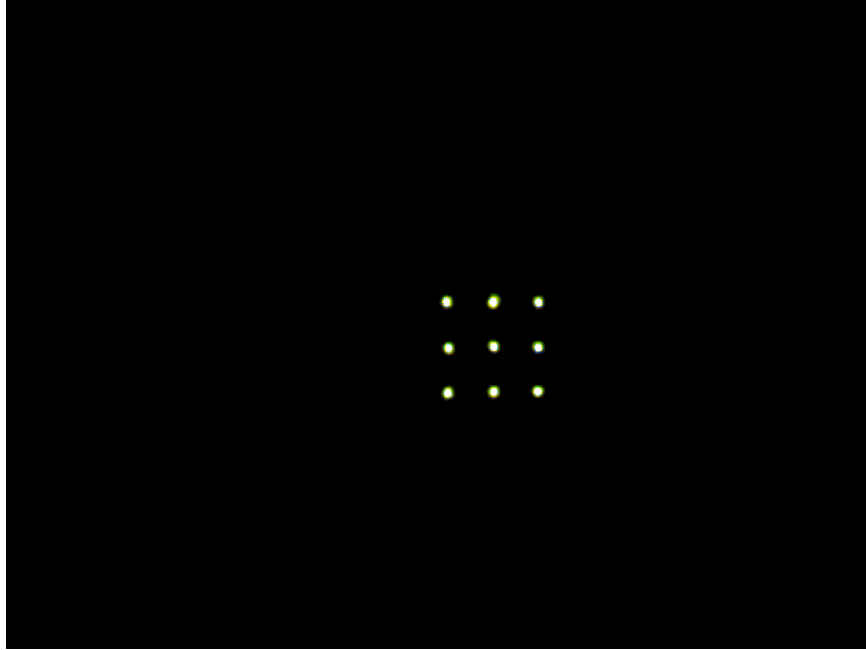


Figure 62: Test 1 Snapshot, Position 1

In this test, all of the LEDs were set at the same PWM duty cycle setting. It is important to note that the algorithm ranks the nine LEDs in each image depending on the recorded magnitudes, with LED #1 being the brightest. Since the LEDs' outputs were extremely close to each other, there was considerable variation in the ranking order of the LEDs from one image to the next. Thus, the LED associations applied in this test do not physically pertain to any specific LED, but instead illustrates the algorithmic sensitivity to overlapping magnitude values. Additionally, a general trend is seen from Fig. 64 in that magnitude values from Position 4 tended to be the smallest of the recorded values, and that measurements from Position 2 tended to be the largest. Furthermore, the data presented in Fig. 65 indicates that while the LEDs may have the same in-line resistor values and PWM duty cycle, there is a non-uniform distribution of recorded magnitude measurements, likely due to small-scale variations in actual resistance values for the resistors, as well as varying light output characteristics of the individual LEDs. Additionally, each LED was masked

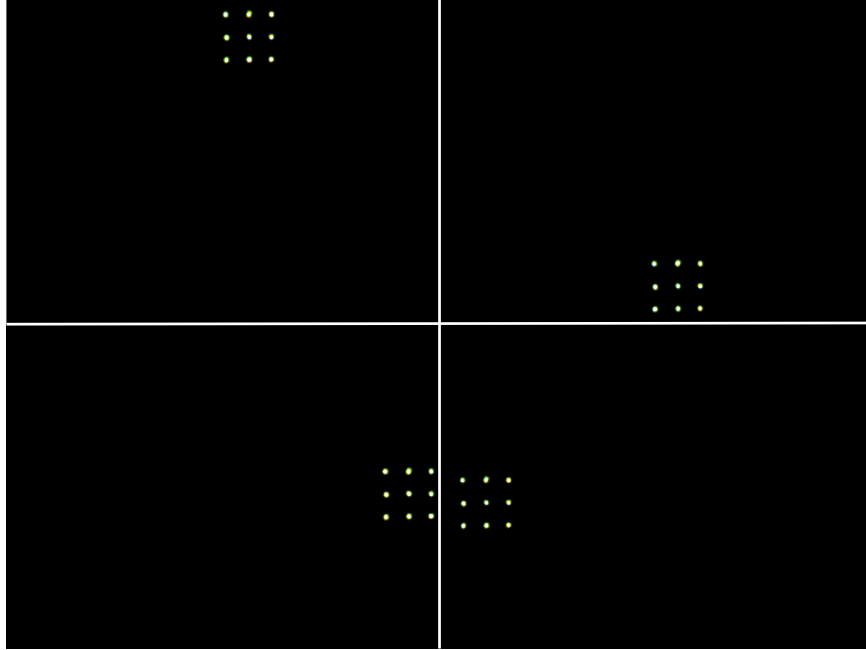


Figure 63: Test 1 Snapshots, Positions (clockwise from top left): 2, 3, 4, and 5

by hand with black ink which could cause each LED to exhibit unique light outputs. Overall, it is seen that there is some sensitivity to the viewing angle of the LED from the camera, overlapping magnitudes can hinder the algorithm's ability to rank specific LED brightness values, and that each LED/resistor pair exhibits a characteristic light output. However, judicious choice of PWM values should allow each LED to reside within its own unique range of magnitude measurements.

Additional secondary insight was gained from this test, depicted in Figure 66. The distribution of angular separation measurements clearly show the five distinct angular measurements coinciding with the expected five distinct angular measurements discussed in Section 3.4.1.2. However, it should be noted that obvious overlap of the angular separation measurements results from the reduction of the 36 pair angles into only five measurably-distinct angles.

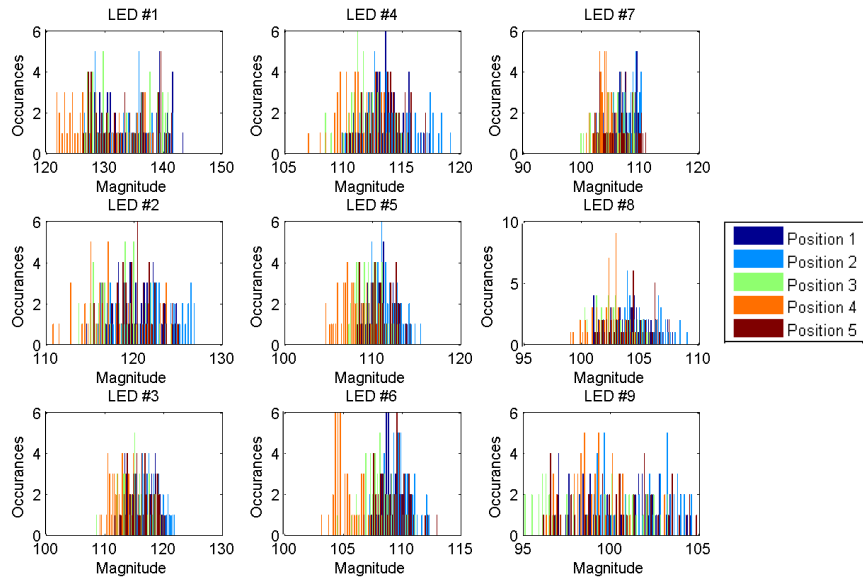


Figure 64: Test 1 Magnitude Distribution Across Positions, by LED

4.3 Test 2 Results

The results of the star field surface validation tests discussed in Section 3.7.2 are presented in this section. The objective of this testing is to demonstrate the consistency of measurements across the surface of the dome, specifically of measurements of the same patch board LED pair placed at three different locations within the dome represented in Figures 59 and 60. The corresponding images from this test are shown (enhanced to display the dimmer LED) in Figs. 67 and 68. Note the second star is very dim, but detectable by the system, and that the patch board is maintained relatively close to the bore sight of the camera to isolate any viewing angle affects. Similar to the previous section, the distribution of magnitude measurements assigned to each LED over the course of 150 total image collections is first illustrated in Fig. 70. Next, this data is plotted on the same histogram in Fig. 70. Tables 3 and 4 lists the mean values for the LED magnitudes and standard deviations across all three positions.

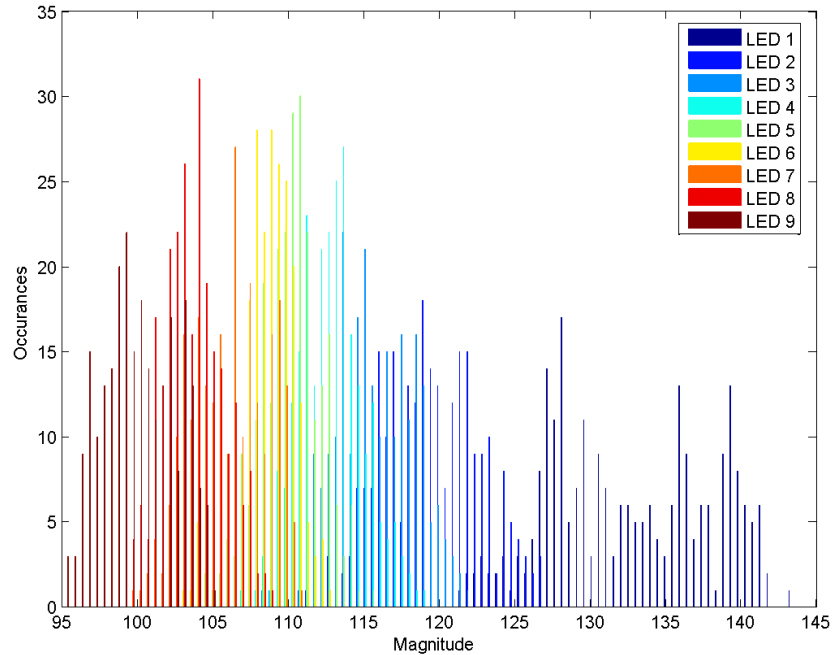


Figure 65: Test 1 Magnitude Distribution Across Positions, Combined

Additional histogram figures showing distribution data at each position can be found in Appendix A.2.

From Figures 69 and 70, distinct magnitude measurements are seen for each LED. A trend is noted from Fig. 69 in that the mean recorded magnitude for LED #1 is highest at Position 3, while LED is the least brightest at Position 3. This trend suggests a slight variation of the magnitude measurements across the dome, and most likely indicates that the relative viewing angle to the LEDs changed slightly as a result of the varying surface contour of the dome. It is also noted from Fig. 70 that the two LEDs occupy distinct bins on histogram, and that a large separation of values exists between the two distributions as a result of choosing the maximum and minimum PWM settings for each LED. Additionally, it is observed that the distribution for LED #1 is wider than that of LED #2, due most likely to the higher fluctuations in magnitude as a result of the larger duty cycle setting for the LED.

Table 2: Test 1 Mean Instrument Magnitude Data Across All Positions

LED	Mean	Std. Dev
1	132.67	5.3192
2	119.61	3.2753
3	115.58	2.0250
4	112.92	2.1444
5	110.17	2.0205
6	108.30	1.9913
7	106.05	2.5085
8	103.61	1.9879
9	100.05	2.3919

Table 3: Test 2 Mean Positional Instrument Magnitude Values (Non-Dimensional)

Position	LED	
	1	2
1	192.10	7.1434
2	192.25	7.1925
3	195.79	6.8189
Avg	193.38	7.0516

In addition to the information gained from analysis of the magnitude measurements discussed above, the key result from this test pertains to the measured angular separations between the LED pair at each position. Shown in Fig. 71, it can be seen that the pair angle decreases as the location of the patch board changes from the apex (Position 1) to the edge of the dome (Position 3), which indicates that the varying

Table 4: Test 2 Standard Deviation Values of Mean Positional Instrument Magnitudes

Position	LED	
	1	2
1	6.7943	0.9862
2	6.0911	0.9360
3	6.2370	0.9041
Avg	6.6590	0.9510

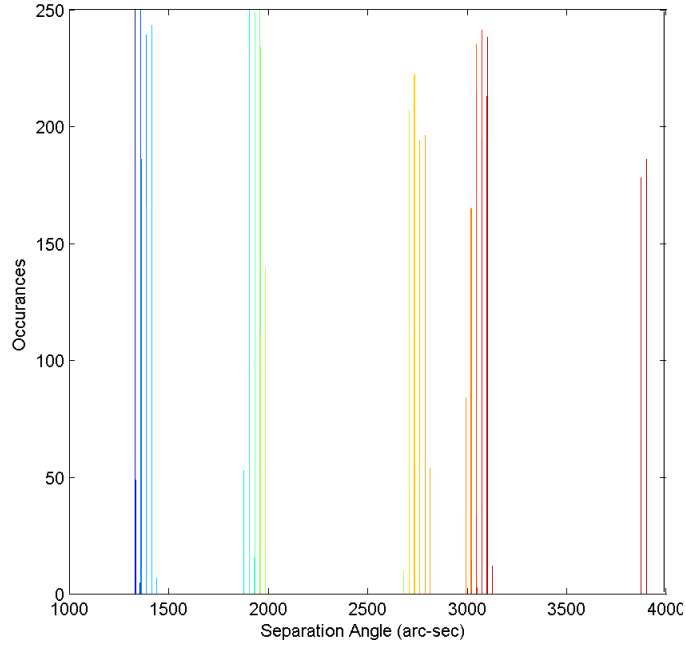


Figure 66: Test 1 Angular Separation Distribution Across Positions, Combined



Figure 67: Test 2 Snapshot Position 1

surface contour contributes an off-centered viewing angle on the LED pair. Table 5 contains the mean angular measurement data across all observations.



Figure 68: Test 2 Snapshot, Positions 2 (top) and 3 (bottom)

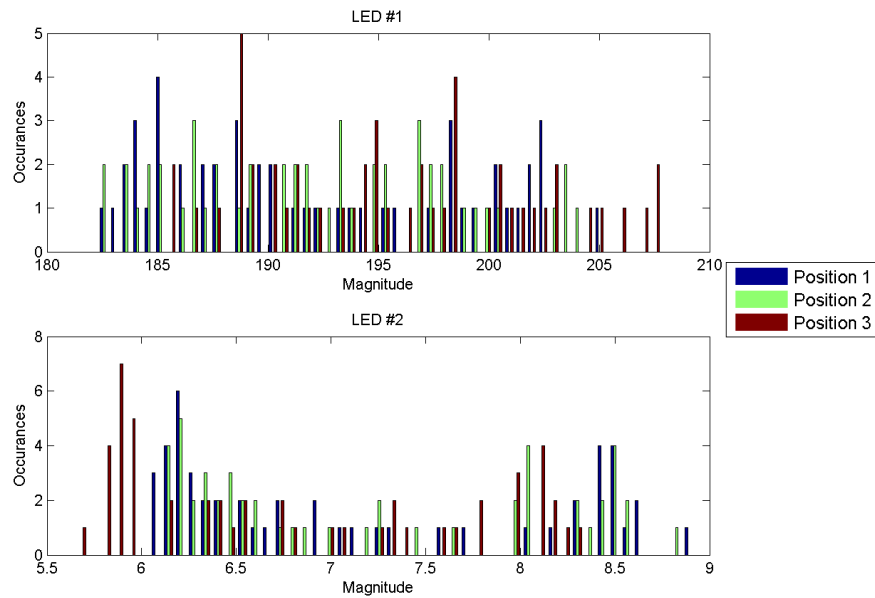


Figure 69: Test 2 Magnitude Distribution Across Positions, by LED

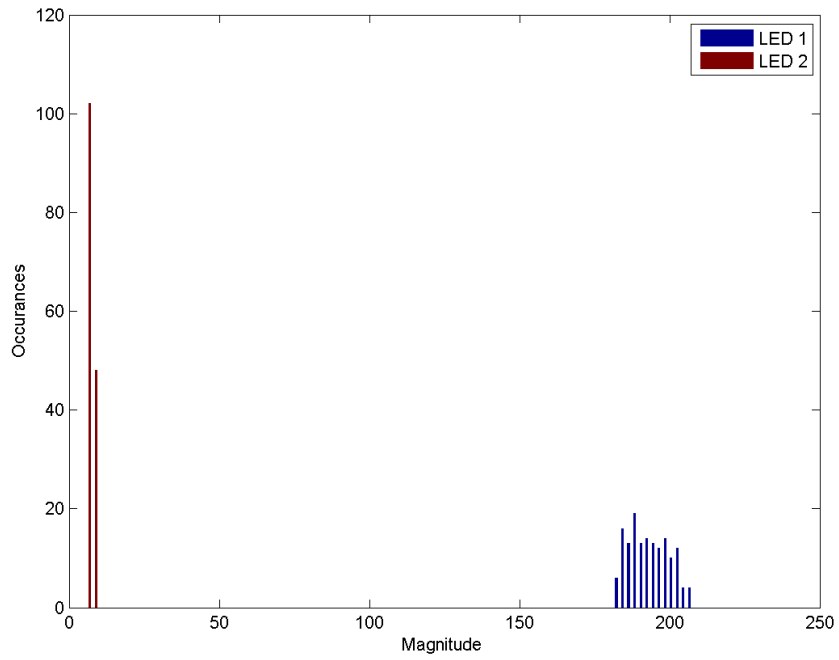


Figure 70: Test 2 Magnitude Distribution Across Positions, Combined

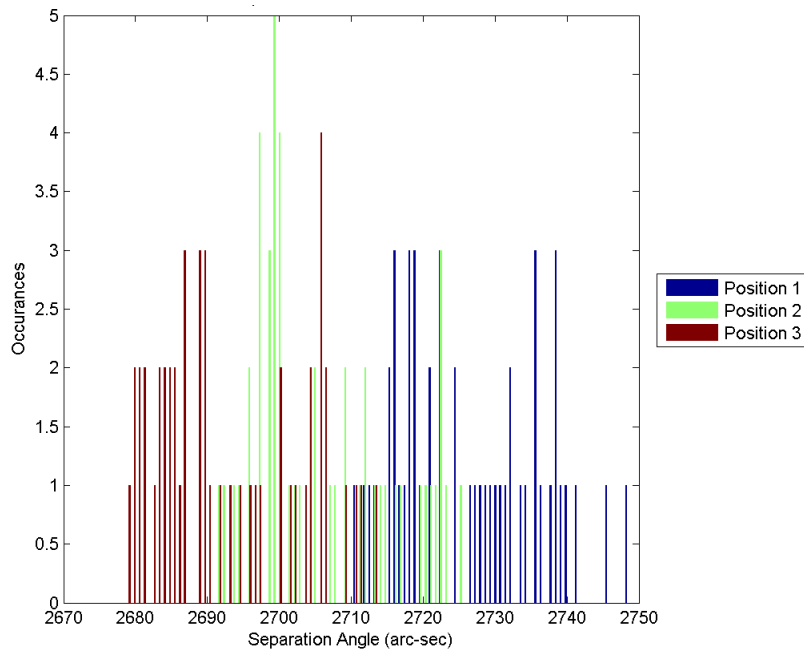


Figure 71: Test 2 Angular Separation Distribution Across Positions, Combined

Table 5: Test 2 Mean Angular Separation Data Across by Position

Position	Mean (arc-sec)	Std. Dev (arc-sec)
1	2727	9.715
2	2706	9.805
3	2693	10.24

4.4 Test 3 Results

This section discusses the results from the algorithm test detailed in Section 3.7.3. The objective of this test is to validate the concept star field LED features as usable data inputs into a star pattern and attitude determination algorithm. The first step in this process is the calibration step, performed in a similar manner as the preceding two tests. The second step was actual implementation and evaluation of the cataloging, tracking, star pattern recognition, and attitude determination algorithm. For both steps, the same 5-LED pattern described in Section 3.7.3 was used.

The test begins with the collection of 50 images at 5 different positions. Figures 72 and 73 depict the locations of the pattern on the image frame at the corresponding SimSat positions. The top left of Fig. 72 contains a key to aid in visualizing the established PWM ranking. The recorded SimSat orientation data from the IMU is listed in Table 6 in Euler Angles $(\theta_1, \theta_2, \theta_3)$, where 1, 2, 3 correspond to the inertial X-, Y-, and Z-axis, respectively. It should be noted here that, in maneuvering SimSat into the fifth and final position, SimSat was slightly 'bumped'; the extent of harm to the recorded IMU data is discussed later in this section.



Figure 72: Test 3 Snapshot, Position 1



Figure 73: Test 3 Snapshots, Positions (clockwise from top left): 2, 3, 4, and 5

Table 6: Test 3 IMU Euler Angle Data for Each Position

Position	θ_1 (deg)	θ_2 (deg)	θ_3 (deg)
1	0	0	0
2	-0.0090	2.3	0.0070
3	0.25	-2.1	0.0040
4	3.3	-0.14	-0.028
5	-1.9	0.28	0.19

4.4.1 Test 3 Calibration. The distribution of magnitude measurements assigned to each LED over the course of 250 total image collections is illustrated in Fig. 74. Figure 75 displays a combined histogram of the data in the previous figure. Furthermore, Table 7 lists the averaged values for the LED mean magnitudes and standard deviations across all five positions. Additional histogram figures for this calibration can be found in Appendix A.3.

As evidenced from Fig. 74, a slightly discernible relationship between position and LED magnitude can be noted. However, the most critical aspect of the magnitude

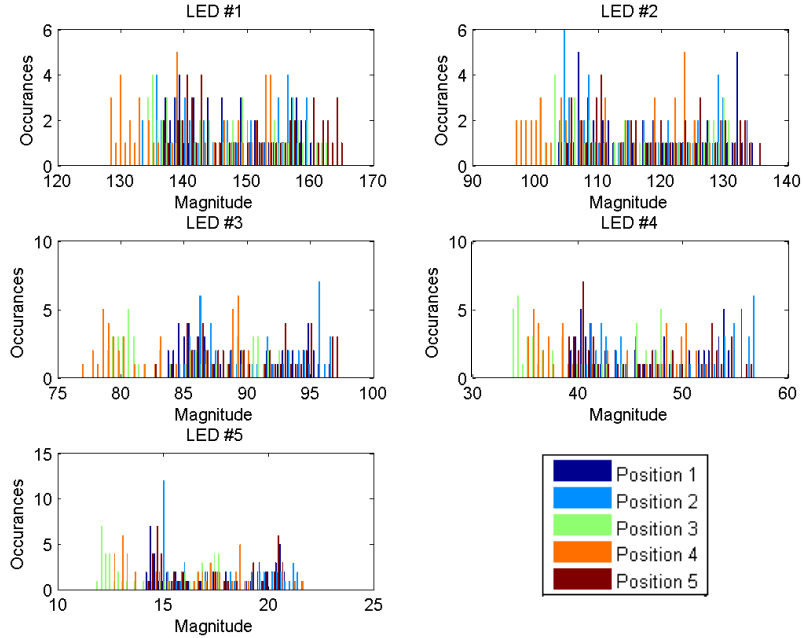


Figure 74: Test 3 Magnitude Distribution Across Positions, by LED

Table 7: Test 3 Mean Instrument Magnitude Data Across All Positions

LED	Mean	Std. Dev
1	146.69	9.2704
2	116.01	10.191
3	87.770	5.1960
4	44.894	6.5327
5	16.612	2.6475

distributions for this patch board configuration is seen in Fig. 75, where each LED roughly corresponds to a unique magnitude bin across all measured magnitudes, with very little room for additional unique LEDs measurements. There is small overlap for some LEDs. These regions of overlap are relatively limited, but when considering the match criteria for magnitude values in this research effort to be the range $\pm 3\epsilon_{\text{magnitude}}$, the effective overlap between magnitude values of specific LEDs becomes considerable. For example, considering LED #2 from Table 7, ± 3 times its standard deviation centered over its mean magnitude of 116.01 places the mean values of LEDs #1 and #3 within this range. However, the remaining criteria in the direct match test are

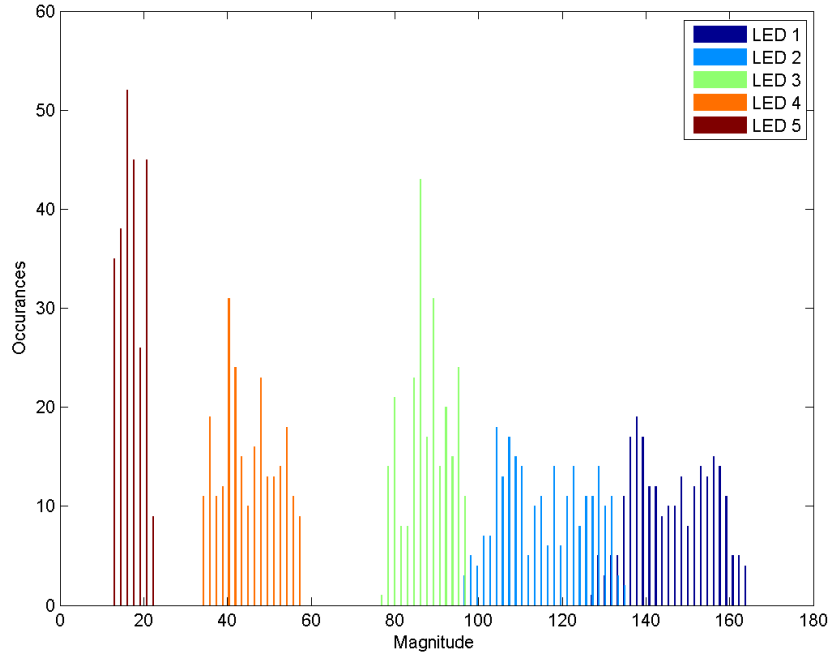


Figure 75: Test 3 Magnitude Distribution Across Positions, Combined

designed to address this situation, therefore the PWM settings are satisfactory for this test.

Figure 76 shows the distribution of angular measurements for the LED pairs comprising the star pattern. Three angular measurements are statistically discernible here for this pattern, which can be deduced by reexamining Fig. 72. The implication here is that the pattern recognition algorithm will have a more limited set of uniqueness criteria to apply in the Direct Match test. Table 8 lists the mean LED pair separation angles across all positions and their corresponding standard deviations. It is also reflected here that the match criteria range of $\pm 3\epsilon_{separation}$ places pair angles within overlapping bins. Again, the multiple matching criteria used in direct match test is designed for this scenario.

As mentioned in Section 3.6.3, the calibration algorithm uses input Euler Angles gathered from the IMU to transform the body frame vectors mapped as discussed in Section 3.6.2.2 into the inertial frame. How closely the corresponding LEDs are

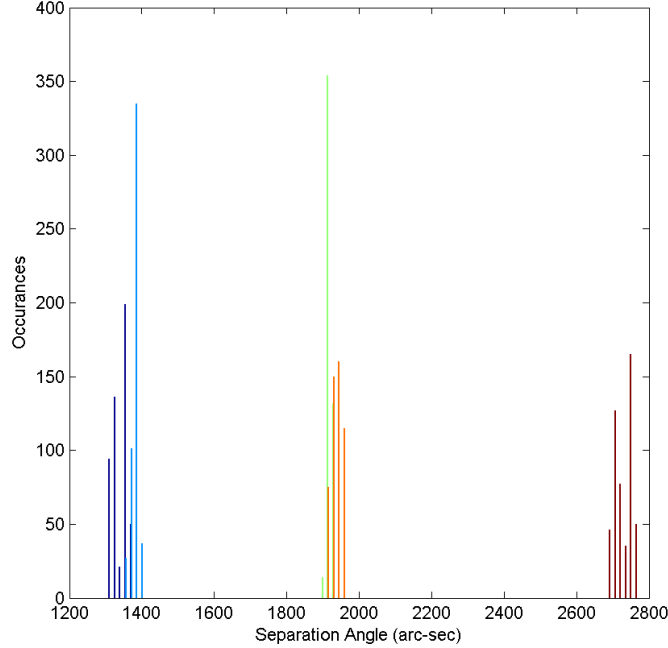


Figure 76: Test 3 Angular Separation Distribution Across Positions, Combined

mapped back into theoretically the same inertial location determines the error associated with the LED spatial positioning. Thus, Figs. 77 and 78 shows the distributions of the X-,Y-, and Z-coordinates of the vector observations associated with the 250 images of the the 5 LEDs. Outliers are clearly visible from Fig. 77 (a) at approximate X-coordinates 0.75 mm, 8.5 mm, and 17 mm. This was the result of the slight 'bump' of SimSat prior to recording the last image. Thus, the IMU's rate limits were momentarily exceeded, which resulted in unreliable position measurement data at this point. However, the data was recorded and the test proceeded as planned.

Figure 78 shows a small non-Gaussian distribution of less than 1 mm for the Z-coordinates. The inertial Z-coordinates are approximated values derived from the formulation of the tracker frame vectors in Eq. (44), specifically in the $(R - M)$ term. This method does not take into account the non-linear projections of the objects on the spherical surface to the flat image plane, depicted in Fig 50, which is a function of the distance of the object on the image plane to the bore sight and the height h of

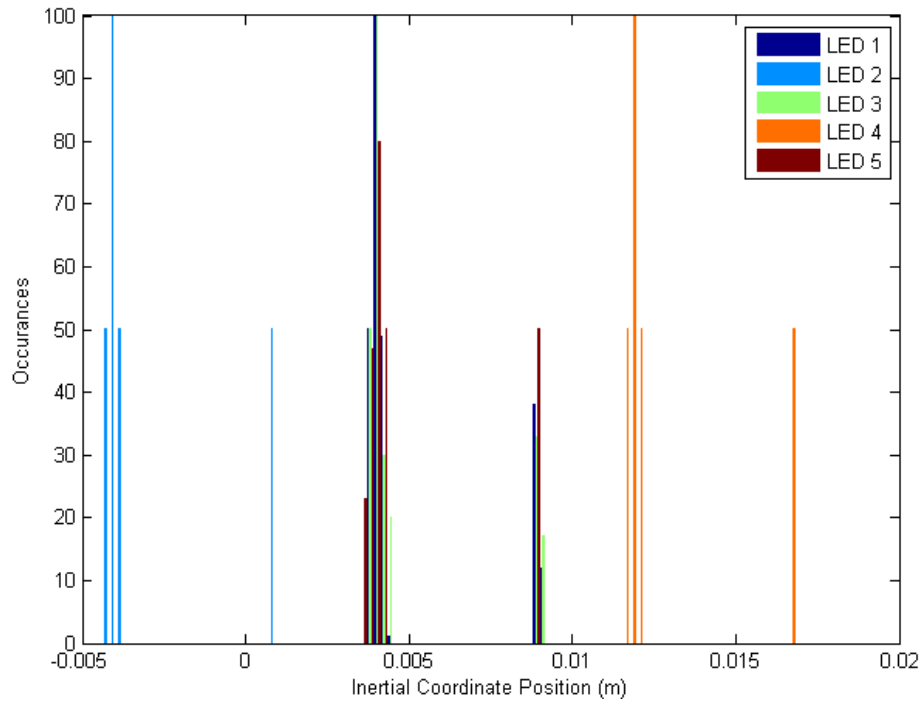
Table 8: Test 3 Mean Separation Angle Values Across All Positions

LED Pair	Mean Angle (arcseconds)	Std. Dev (arcseconds)
1	1,325	8.871
2	1,359	5.229
3	1,377	8.369
4	1,388	4.901
5	1,913	4.957
6	1,919	5.972
7	1,925	7.368
8	1,950	5.838
9	2,703	9.195
10	2,746	9.675

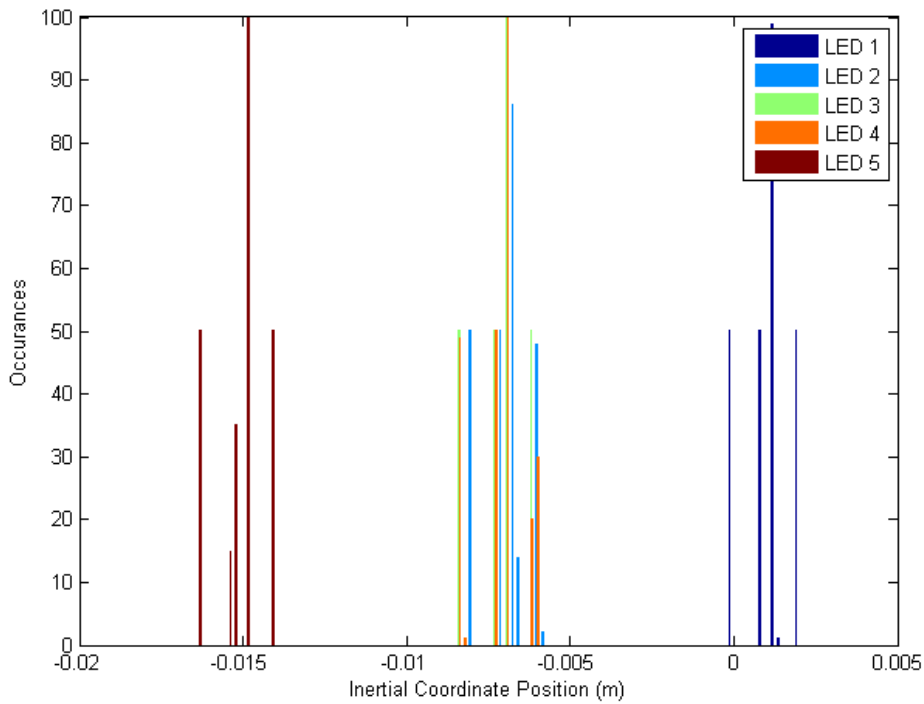
the spherical arc. Because the radius of the sphere is relatively large, and the FOV is kept small, this effect is reduced to the small degree of error seen in Fig. 78.

In order to better visualize the complete calibration 'picture', Figure 79 shows a scatter plot of LED vector coordinates in the X-Y internal plane. The figure is shown from roughly the vantage point of SimSat. Within it, plots of the patch board pattern are displayed for each position recorded during the calibration step. The sizes of the markers indicate the relative brightness of a particular LED with respect to the other LEDs in its corresponding pattern. In other words, the magnitude ranking of each LED is depicted by the size of the marker. The outliers resulting from the SimSat 'bump' during Position 5 is seen falling outside the closer LED groupings, which will affect the error estimate LED position. However, noting the black markers indicating the averaged X-Y coordinates for all positions, the overall LED position results remain very close to Position 1. Therefore, instead of reproducing the experiment with more optimal measurements, it was decided to use a set of measurements with some increased inherent error to test the robustness of the algorithm.

To derive the final error constants necessary for the star pattern recognition algorithm, the maximum values of the averaged multi-positional standard deviation



(a) X-Coordinates



(b) Y-Coordinates

Figure 77: Test 3 LED X, Y Inertial Coordinate Distributions, Combined

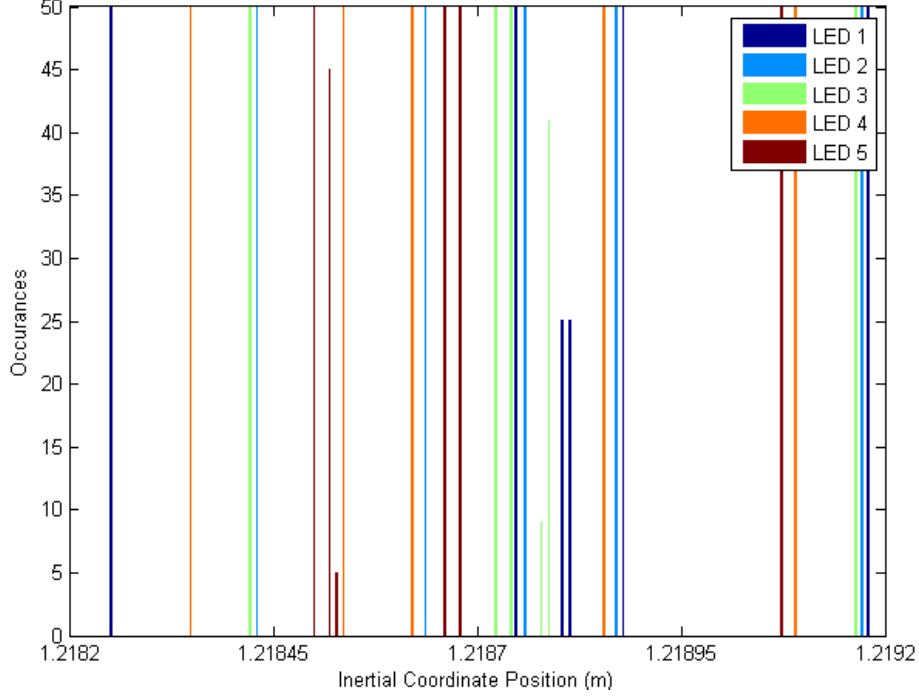


Figure 78: Test 3 LED Z Inertial Coordinate Distributions, Combined

values for magnitude, separation angle, and position are set at $\epsilon_{magnitude}$, $\epsilon_{separation}$, and $\epsilon_{position}$, respectively. Table 9 lists the calculated error constants ϵ for use by the star pattern recognition algorithm. There is some overlap within the distributions of magnitude, separation, and position values when considering the 3ϵ range of these values, which is not optimal. However, these ranges of overlap are localized and therefore are utilized by the algorithm to narrow the list of possible match candidates.

Table 9: Test 3 Algorithm Error Values

$\epsilon_{magnitude}$	10.191 (unitless)
$\epsilon_{position}$	1.9861 (millimeters)
$\epsilon_{separation}$	9.675 (arcseconds)

4.4.2 Test 3 Star Pattern Recognition and Attitude Determination. With the measurement calibrations completed, the image seen in Fig. 72 served as the image viewed when the body and inertial frames are aligned, in order to build a star catalog,

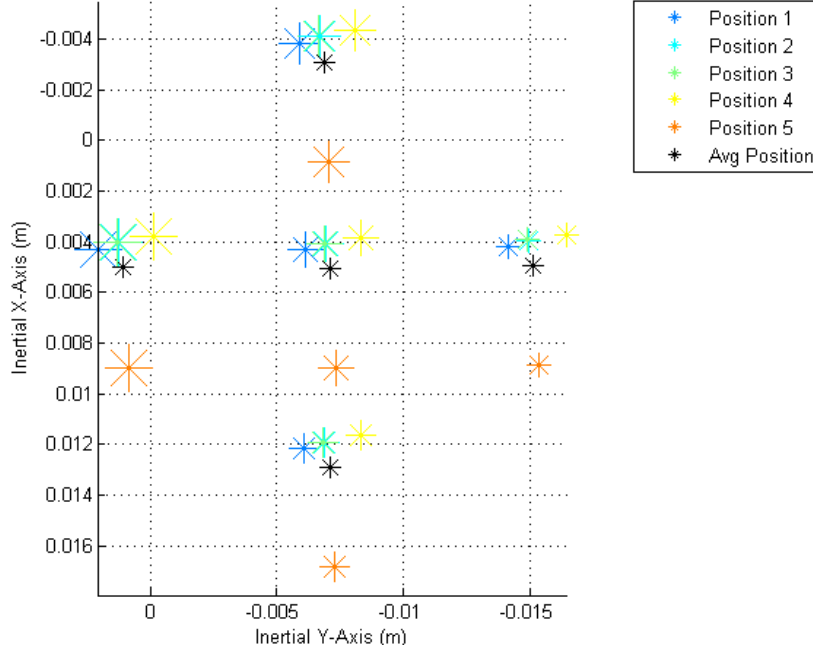


Figure 79: Test 3 Mean X-Y Coordinate Scatter Plot

as outlined in Section 3.6.4. Next, the images represented in Fig. 73 were evaluated by the attitude determination algorithm one at a time. The algorithm was executed on one image at each position. The ϵ error values found in the previous section were used to facilitate star matching within the star pattern recognition algorithm. The output of the QUEST algorithm is a quaternion vector \vec{q} , which is then converted to a 3-2-1 rotation matrix in order to plot the vector visualizations. Finally, the quaternions are converted to Euler Angles here for ease of presentation. The following sections present the results from these tests.

4.4.2.1 Position 1 Estimation Results. The first position test was a baseline test of the algorithm, where no change in images, and thus no apparent change in position, is actually made. The star pattern recognition algorithm easily matched each LED from both images as seen from the top-right of Fig. 80, which illustrates the vector visualization of the results, the star tracker, the body frame, and the inertial frames. The blue asterisks represent the cataloged star locations,

while the magenta lines represent the algorithm-mapped inertial vectors. The degree to which these two objects coincide indicates how well the cataloged and tracked observations physically matched. Note that the close-up view of the body and inertial frames shows the two coordinate frames to be coincident.

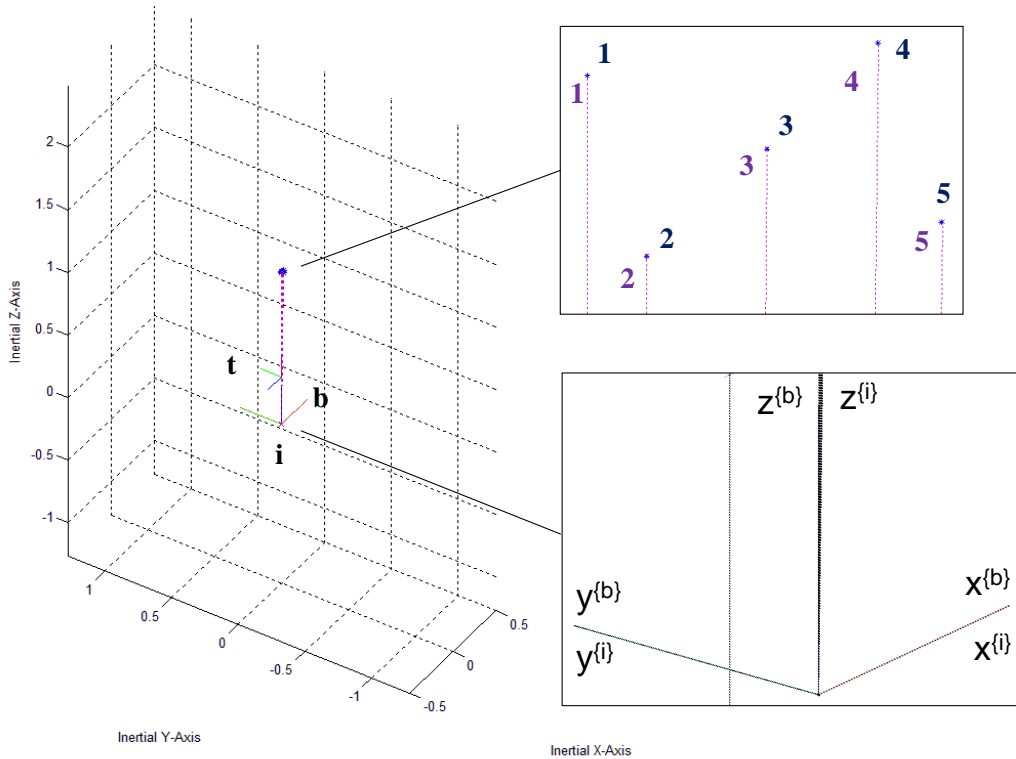


Figure 80: Test 3 Attitude Estimation Visualization, Position 1

Some useful insight about the algorithm was gained from the data in Table 10, the estimated body frame Euler Angles with respect to the inertial frame are shown compared to the IMU measurements. There is some disagreement between the two sets of Euler Angles. Since the images used for cataloging and attitude determination are the same, there should be no variations in LED centroiding. Therefore, these errors may be attributed to algorithm noise.

4.4.2.2 Position 2 Estimation Results. The results of the attitude estimation for the second position are described below. Again, the star pattern recognition

Table 10: Test 3 Attitude Estimation Results, Position 1

	IMU (deg)	Algorithm (deg)	Abs. Diff (deg)
θ_1	0	-0.0335	0.0335
θ_2	0	0.0335	0.0335
θ_3	0	0.0005	0.0005

algorithm easily matched each LED from both images. Figure 81 illustrates the vector visualization of the results, where the the star tracker, body frame, and inertial frames are depicted. From Fig. 81, the catalog and mapped inertial coordinates closely match. The roughly 2.3 degree rotation about the inertial Y-axis is depicted by the close-up view of the body and inertial frames. Table 11 lists the estimated Euler Angles for this test. The Y-axis rotation angle is in close agreement, while the X and Z-axis rotation angles differ as much as 0.18 degrees from the IMU data.

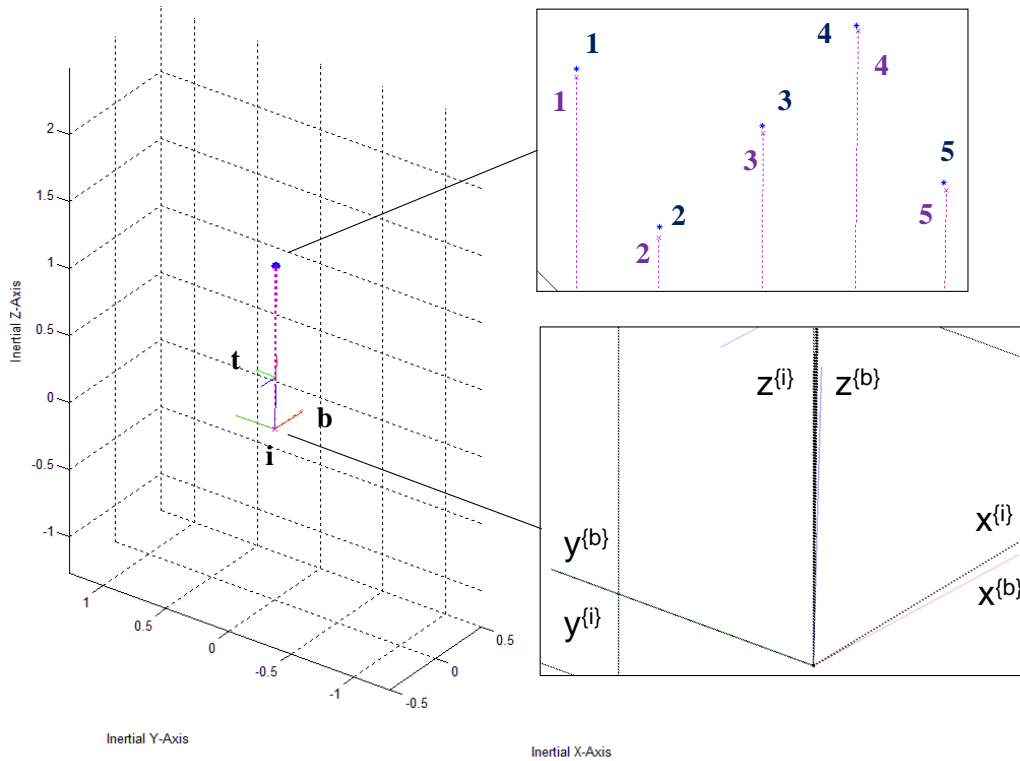


Figure 81: Test 3 Attitude Estimation Visualization, Position 2

Table 11: Test 3 Attitude Estimation Results, Position 2

	IMU (deg)	Algorithm (deg)	Abs. Diff (deg)
θ_1	-0.0090	0.1732	0.1822
θ_2	2.3130	2.3273	0.0143
θ_3	0.0070	-0.0389	0.0459

4.4.2.3 *Position 3 Estimation Results.* The third position test proceeded similar to the previous runs. The LEDs were readily matched by the star pattern recognition algorithm. From Fig. 82, the catalog and mapped inertial coordinates closely match. The roughly -2.06 degree rotation about the inertial Y-axis is depicted by the close-up view of the body and inertial frames. Table 12 lists the estimated Euler Angles for this test. The Y-axis rotation angle is again in close agreement for this test. A roughly 0.72 degree difference is noted for the X-axis rotation.

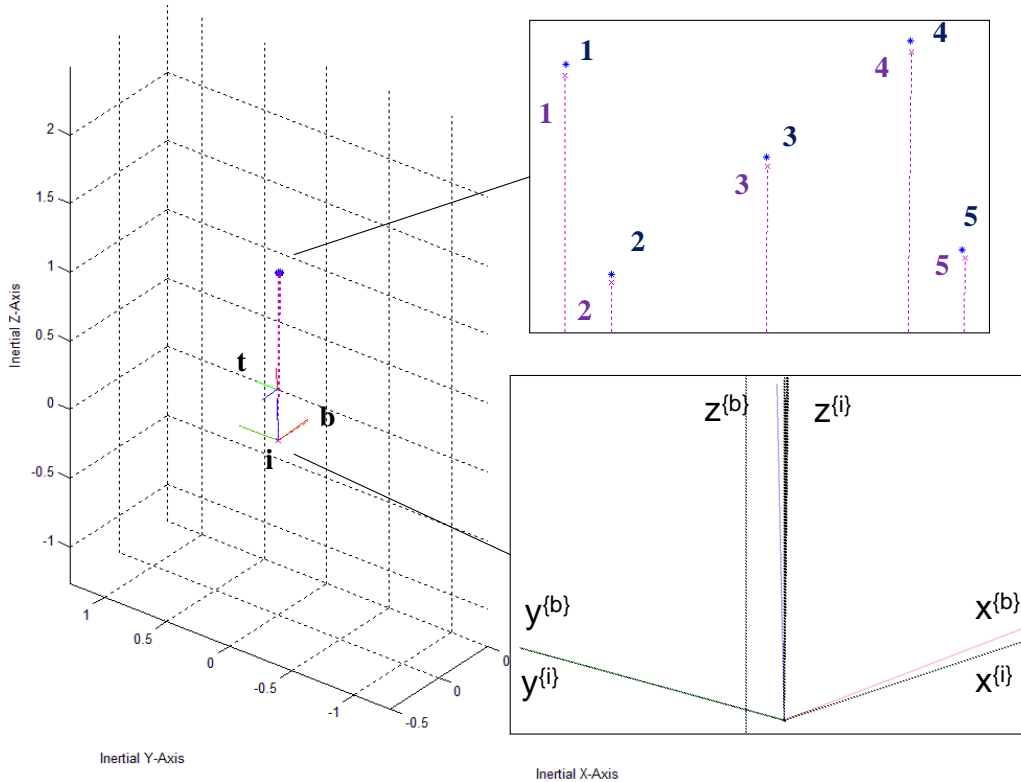


Figure 82: Test 3 Attitude Estimation Visualization, Position 3

Table 12: Test 3 Attitude Estimation Results, Position 3

	IMU (deg)	Algorithm (deg)	Abs. Diff (deg)
θ_1	0.2490	-0.4672	0.7162
θ_2	-2.0760	-2.0595	0.0165
θ_3	0.0040	0.2312	0.2272

4.4.2.4 *Position 4 Estimation Results.* The results of the fourth attitude estimation test produced closely-agreeing results. As before, no notable issues with LED matching. From Fig. 83, the catalog and mapped inertial coordinates closely match. An approximate rotation angle of 3.2 degrees about the inertial X-axis is depicted by the close-up view of the body and inertial frames. The Euler Angle results are listed in Tab 13. All estimated Euler Angles closely agree, with a maximum difference of approximately 0.11 degrees on the Z-axis Euler Angle.

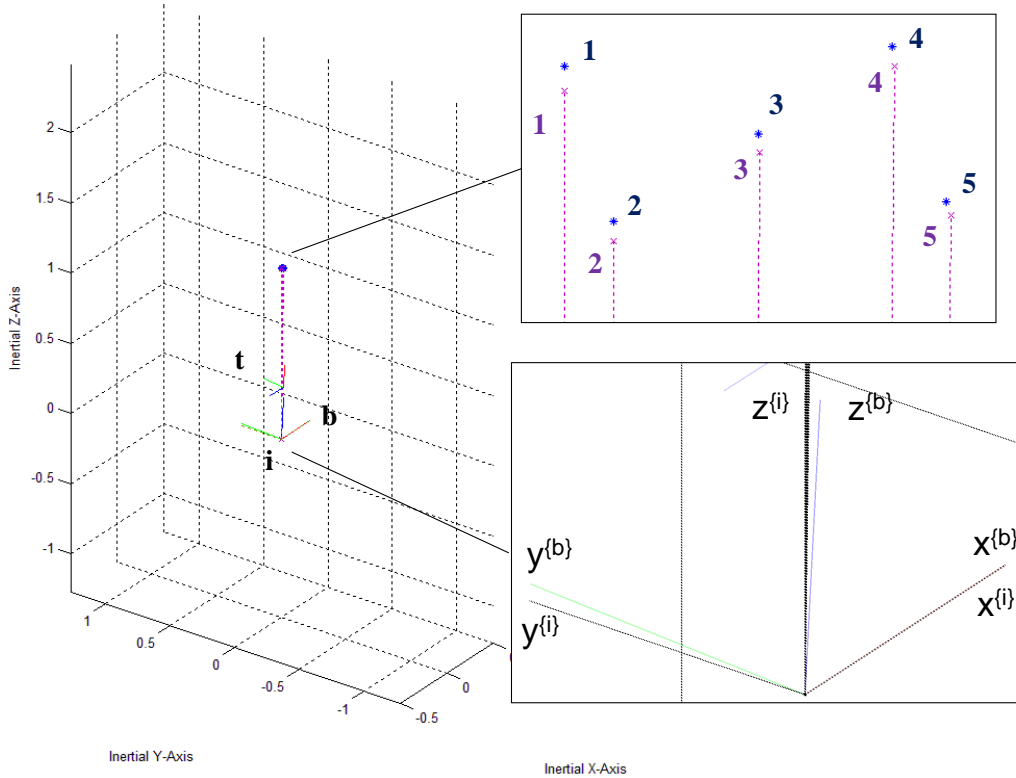


Figure 83: Test 3 Attitude Estimation Visualization, Position 4

Table 13: Test 3 Attitude Estimation Results, Position 4

	IMU (deg)	Algorithm (deg)	Abs. Diff (deg)
θ_1	3.3370	3.2338	0.1032
θ_2	-0.1370	-0.1171	0.0199
θ_3	-0.0280	0.0848	0.1128

4.4.2.5 Position 5 Estimation Results. The fifth attitude estimation test results are shown below. It is important to note that the IMU data was expected to be unreliable due to the accidental 'bumping' of SimSat during manual maneuvering. The LED matching by the star pattern recognition algorithm proceeded smoothly. From Fig. 84, the catalog and mapped inertial coordinates are still in relatively close agreement. The estimated Euler Angles for this test are listed in Tab. 14. The Euler Angles for both sets remain in relatively close agreement given that the IMU data is not completely reliable in this test. Based on the successes of the previous experiments, this test helps to highlight a scenario where the attitude estimate may be used to correct the IMU bias.

Table 14: Test 3 Attitude Estimation Results, Position 5

	IMU (deg)	Algorithm (deg)	Abs. Diff (deg)
θ_1	-1.8820	-1.9375	0.0555
θ_2	0.2800	0.0410	0.239
θ_3	0.1910	-0.5982	0.7892

4.4.2.6 Attitude Estimation Overall Results. Table 15 lists the pertinent statistics of the absolute differences between the IMU-measured Euler Angles and the calculated Euler Angles. Computing across the five positions, the algorithm returns a minimum Euler Angle difference of approximately 0.0005 degrees and a maximum of about 0.7892 degrees. Overall, the averaged maximum angular deviation across the three Euler Angles from the IMU measurements was 0.5815 degrees. There-

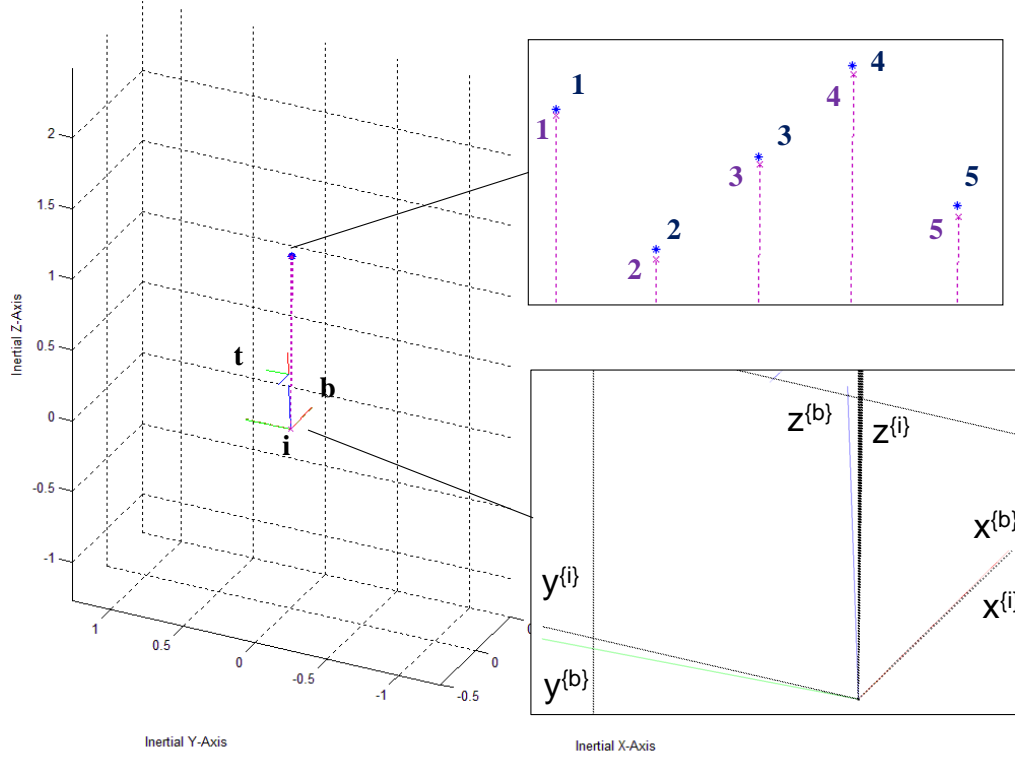


Figure 84: Test 3 Attitude Estimation Visualization, Position 5

fore, the attitude solution returned by the algorithm under the described conditions is accurate to within less than one degree in any Euler Angle direction.

Table 15: Test 3 Attitude Estimation Results, Position 5

	Min (deg)	Max (deg)	Mean (deg)	Std Dev (deg)
θ_1	0.0335	0.7162	0.2181	0.2842
θ_2	0.0143	0.2390	0.0646	0.0978
θ_3	0.0005	0.7892	0.2351	0.3213
Averaged	0.0161	0.5815	0.1726	0.2344

4.5 Summary

Chapter IV presented the results and analysis of the concept validation tests in order to validate the concept developed in this research effort. Regarding the results of the tests, all aspects of the system concept performed to an acceptable level,

with some exceptions. First, the LEDs exhibit characteristic light outputs given equal voltage inputs. Second, the elliptical surface contour of the dome causes variational measurements of both magnitude and separation angle. Suggested approaches for resolving these issues are presented as future work in the next chapter. The testing discussed in this section demonstrates that the external reference system concept for SimSat is capable of providing relatively accurate attitude estimates. The results further indicate that the current PWM methodology only provides sufficient range of magnitude for five unique magnitude measurements, while the fixed pattern arrangement of the LED patch board allows for only 3 uniquely-measurable separation angles. Additionally, using the current dome surface, cataloging of LEDs must be done by the on-board camera and not through an external source, since there would not be agreement between the angular separations measured by the two methods.

V. Conclusion and Recommendations

5.1 Conclusion

The objectives of this research effort were to investigate the critical parameters for a lab-scale star tracker-based external reference system for AFIT's SimSat, integrate a working concept of it within the current SimSat laboratory, and characterize the performance of the concept system through initial validation testing against key algorithmic requirements. The effectiveness is determined by implementing the necessary software coding into SimSat's current programming software and utilizing the data provided by the concept reference system as algorithm inputs. The result of this research effort is a preliminary working concept of a unique star tracker-based external reference system for SimSat to act as an initial point for subsequent research towards a precise, accurate, and robust final solution.

The research methodology was designed to parallel the analysis of space-rated star trackers as much as possible. With the selection of an industrial-purpose digital camera, the selection and configuration of the star representative LEDs and the star field surface had to be made such that the entire system resulted in consistent intensity and spatial measurements with manageable system noise. The first key aspect of the system, the LED configuration, was addressed through preliminary analysis of the critical system-specific lighting and image collection parameters. The key parameters for the system were identified to be the lens focus and aperture setting, the camera exposure setting, the algorithm star recognition settings, and the LED PWM settings. With these parameters identified, the LED configuration was validated through a multi-positional, multi-image test of the LED patch board from various viewing angles. It was determined through this testing that identically-commanded LEDs produced measurably different outputs relative to each other, and that these outputs varied systematically with different viewing angles of the LEDs. Furthermore, it was

seen that overlaps in the magnitude measurements caused inconsistent ranking of the LED, which is a critical parameter in the cataloging and matching of LEDs. Thus, this illustrates the star recognition algorithm's sensitivity to overlapping magnitude values. A secondary finding from this test was that the uniform 3×3 LED square patch board configuration produced five discrete angular measurements. This is the limit to the patch board's flexibility, since the 36 total pair angles provided by nine LEDs is reduced to only five measurable angular separations. Therefore, the symmetry of the final patch board configuration, while easy to construct, limits the overall potential to provide the requisite unique angular measurements. Possible solutions to this are suggested as future work in the next section.

The next portion of this research addressed the star field surface on to which the LEDs would be mounted. It was found from the results of previous research, along with additional analysis provided in this research effort, that a flat surface, while simplistic, did not provide the necessary measurement consistency required of a star-tracker based external reference system. Thus, a spherical surface was chosen in order to better conform to the pinhole camera model for space-rated star trackers. Initial precision measurements of the interior surface of the dome showed that it is appreciably elliptical, caused by a low-cost production process which is unable to produce a perfect sphere.

Formal testing of the star field surface utilized a star pair produced by the same patch board, imaged at three different positions on the sphere near the camera's bore sight. It was seen from testing that the separation angle decreased steadily over the course of the three images totaling 34 arcseconds, or a 0.77% reduction in measured angular separation. Thus, the testing showed that a measurable, systematic change in separation angle resulted from the patch board's changes in location, most likely due to an effective change in viewing angle on the LED patch board as the surface contour

is no longer perpendicular to the camera boresight from these off-apex locations. The 1.9% difference in LED magnitude at the first and last positions also support this conclusion. Suggestions to possibly address this issue is discussed as future work in the next section. However, this drawback is not expected to affect the overall performance of the system, since this affect should not be appreciable for small FOVs. It does, however, limit cataloging of the star field to on-board vector catalog measurements, such as using the star tracker itself. An additional finding from this test was that setting the LEDs used to make up the pair at the maximum and minimum PWM settings produced two vastly different magnitude measurements. Furthermore, it was seen that the higher PWM setting produced a wider distribution of magnitude measurement values, presumably from the increased LED flicker caused by the increased PWM duty cycle. Suggestions to address this issue is discussed in the next section.

The final portion of this research effort was to implement an attitude determination algorithm in order to validate the entire system. After selecting the algorithms used in this research based on prior related research and the desire to reduce complexity, a custom-tailored variation of Boeing's SAA star pattern recognition algorithm, as well as the QUEST attitude determination algorithm, were coded into MATLAB[®]. Testing of the algorithm proceeded in two stages. First, the chosen star pattern was used to calibrate the algorithm and determine the statistical error constants utilized later. The results from this stage show that for a pattern of five LEDs with each LED at a different PWM setting, an acceptable spread of measured magnitudes results, allowing each LED to have a unique, characteristic intensity. Again, the flicker effect is noticeable from the increasing distributions of the brighter LEDs. However, using the five selected PWM values, it was seen that very little room was left for additional LEDs to obtain a unique measurement distribution, especially with increasing distributions. Therefore, an upper limit exists for the number of PWM values that could be

utilized in this current configuration. A suggestion for future work to address this issue is presented in Section 5.2.1. Overall, the necessary error constants for magnitude, spatial position, and angular separation were determined for the next step.

Applying the error constants determined from the algorithm calibration, the star pattern and attitude determination algorithms were executed at five positions to measure the effectiveness of the algorithms using the inputs from the concept system. What was first noted from the results is that a ± 0.033 -degree bias on the first and second Euler Angles existed within the algorithm, independent of image data noise. This algorithmic noise is small, however, and because it is systematic it can be readily addressed through future research. The affect of the overlap of the 3ϵ ranges did not affect the star pattern recognition algorithm. Overall, the stars matched on the first iteration, and the first rotation matrix derived from the quest QUEST algorithm was sufficient to satisfy the direct match test. Thus, the algorithms were quickly and successfully executed when compared to the recorded IMU data. When the IMU data was seen to be unreliable, the algorithm returned an attitude solution that was still close to the unreliable IMU data, and in light of the successes of the previous tests, demonstrates its potential to be utilized to correct the false IMU readings.

Two criteria regarding the accuracy of the system may be applied to the concept system. First, the vector mapping accuracy of the star tracker system, typically related to the bore sight angle by Eq. (10) in space-rated applications, was defined for this research effort to be the accuracy with which the system mapped the LED to within the $3\epsilon_{position}$ region centered about its inertial location on the LED patch board. It was then determined from the calibration prior to Test 3 that the system could map an LED back to its inertial location within 2 mm. Second, the accuracy of the attitude solution was found to be less than 1 degree of any Euler Angle when compared to the reference IMU orientation values for a select region of the dome.

In conclusion, the critical parameters for a lab-based star tracker have been studied and we have found that an indoor star tracker-based reference system capable of accurate attitude determination can be built. Future work must be done in order to evolve the concept developed in this research into an accurate, robust final solution. Overall, this research and the system it produced has introduced AFIT with a new area of research into the field of spacecraft attitude determination.

5.2 Recommendations for Future Development

Below are specific areas of improvement and research areas that apply to the current system concept.

5.2.1 Star Representation Improvements. The LEDs being used to represent stars are currently larger than true point-source light sources, are powered by an analog-emulating digital PWM from an electronic prototyping board, and are physically configured in a symmetrical fashion due to the need to rapidly implement a working system concept. With the algorithm producing initially-satisfying attitude solutions using the current LEDs, a next course of action is to utilize smaller LEDs that require no further modification and still produce Lambertian light outputs. Smaller LEDs could also be spaced closer together, thus improving the star density over the FOV. Reducing the LED size would vastly improve errors caused by centroiding noise and would allow for future use of more space-representative star trackers with unique baffles and smaller FOVs.

As seen from this research effort, PWM was an outstanding choice to power the LEDs from the Arduino Mega as compared to the fixed voltage and resistor method. However, the two major drawbacks were that the Arduino Mega only has a handful of true PWM channels, and that the remaining digital channels were accessed in

sequence using the PWM method described in this research. Therefore, work should be performed in locating or developing a controller board capable of powering each LED independently. Additionally, the use of digital PWM resulted in larger distributions of the measured LED magnitudes at higher PWM settings, or flicker. Furthermore, the effective range of PWM settings was limited by duty cycles that produce acceptable amounts of flicker. Thus, the application of a low pass filter to the power applied to the LED should be considered in order to produce truly analog-like control of individual LEDs that results in a larger min-max range of brightnesses.

Having the LEDs arranged in a symmetrical fashion greatly simplifies construction of the numerous patch boards, and producing each patch board to identical specification further simplifies matters. However, this also reduces the flexibility of the overall utilization of the LEDs to produce unique star pairs necessary for attitude determination. Future work should be dedicated to determining a more flexible method to quickly produce multiple LED groupings that could easily be integrated onto the star field surface. Because of the direct relationship between the LED physical configuration and the star field, the next section suggests a different approach.

5.2.2 Star Field Improvements. It was determined through measurement that the star field surface is not perfectly spherical. Although this is not expected to affect accuracy for the current configuration of the concept system, acrylic domes similar to the one used by this system can be created to within higher precision requirements, but at five times the cost. For example, the same size dome was specified to a different company, which quoted a price of approximately \$2,500, since it required a custom mold for the forming process.

Most importantly, the overall arrangement of the LEDs will govern the star tracker system's attitude determination performance. At the conclusion of this re-

search, only a small portion of the star field is populated with LEDs. In order to populate the entire surface, further study should be conducted into the best possible configuration and arrangement of the LEDs on the dome. Using a variation of Eq. (8) found in Boone's paper (3), the minimum number of total LEDs on the star field surface can be determined by specifying a desired average number of stars imaged per orientation and a desired FOV. If this number is large, regimenting and simplifying the physical arrangement of the LEDs using the patch board method on the star field may produce a more rapidly-implementable solution. However, the negative consequence to this is a star field that is less representative of the night sky, limiting the future application of this system to non-space-rated star trackers. Therefore, solutions other than the patch board method should be considered. This includes researching custom manufactured, flexible adhesive tapes with pre-installed LEDs and resistors. Additional wiring may be specified to allow for independent control of the LEDs. A second option would be to pursue an advanced image projection method onto the dome surface. Specialized projectors which allow for image projection onto the dome inner surface from an off-centered position could allow for a planetarium-like construct. Finally, the method with the most potential for accuracy and representation may be an approach similar to Boone's optical simulator which utilizes the star tracker actuator mount as a laser aiming device to mark the catalog-derived star locations prior to mounting the star-representative fiber optics at locations on the dome (3).

5.2.3 Algorithm Improvements. The current algorithm may be improved by determining a closer estimate to the actual location of the LED on the star field surface. Because the objects on the spherical surface project radially toward the focal point, their projected distances from the boresight are slightly distorted as a function of the height of the arc formed by the spherical surface within the FOV. Research efforts could be dedicated to determining a compensation for this distortion based on

knowledge of the sphere's radius and the width of the field of view. Additionally, multi-positional cataloging will be required when populating the entire dome with LEDs. The algorithm will then need to be integrated into the SimSat SIMULINK control system. Finally, research into advanced algorithms, specifically non-dimensional, or invariant, methods should be performed as a study into their abilities to mitigate such distortions.

Appendix A. Supplemental Results Figures

A.1 Test 1 Results

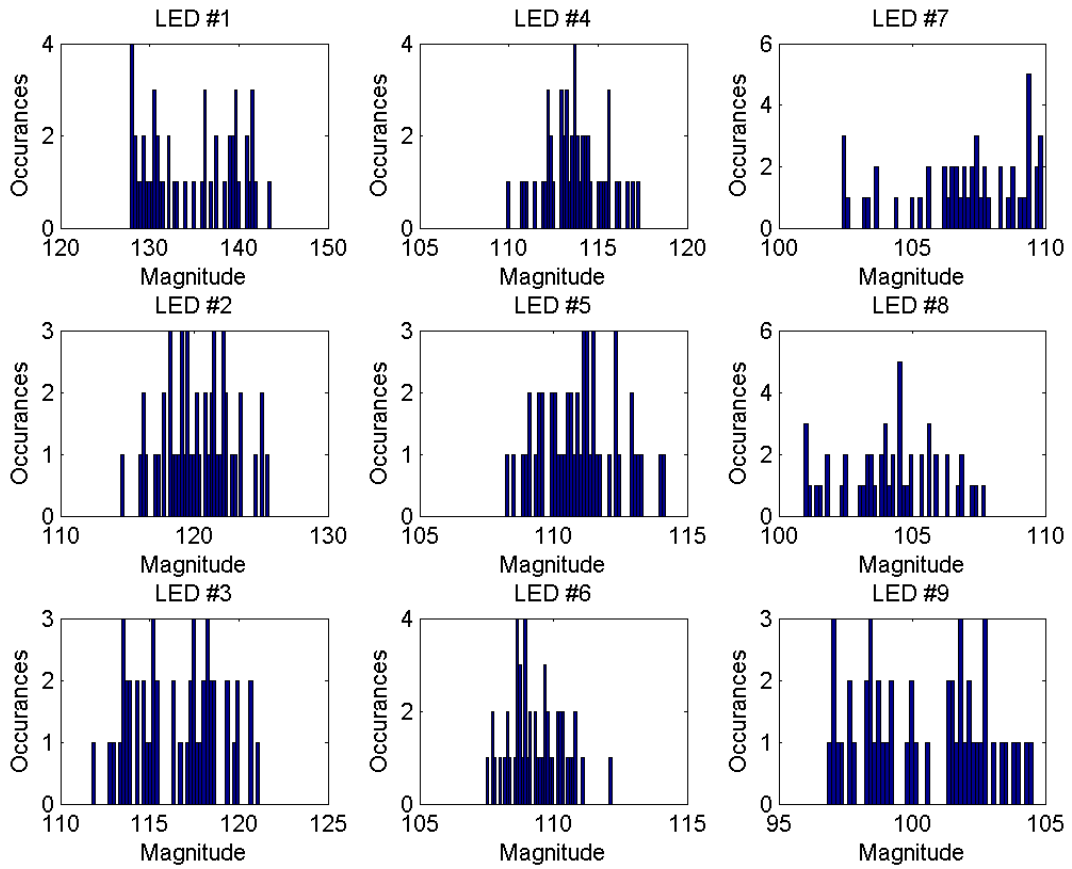


Figure 85: Test 1: Magnitude Distribution at Position 1, by LED

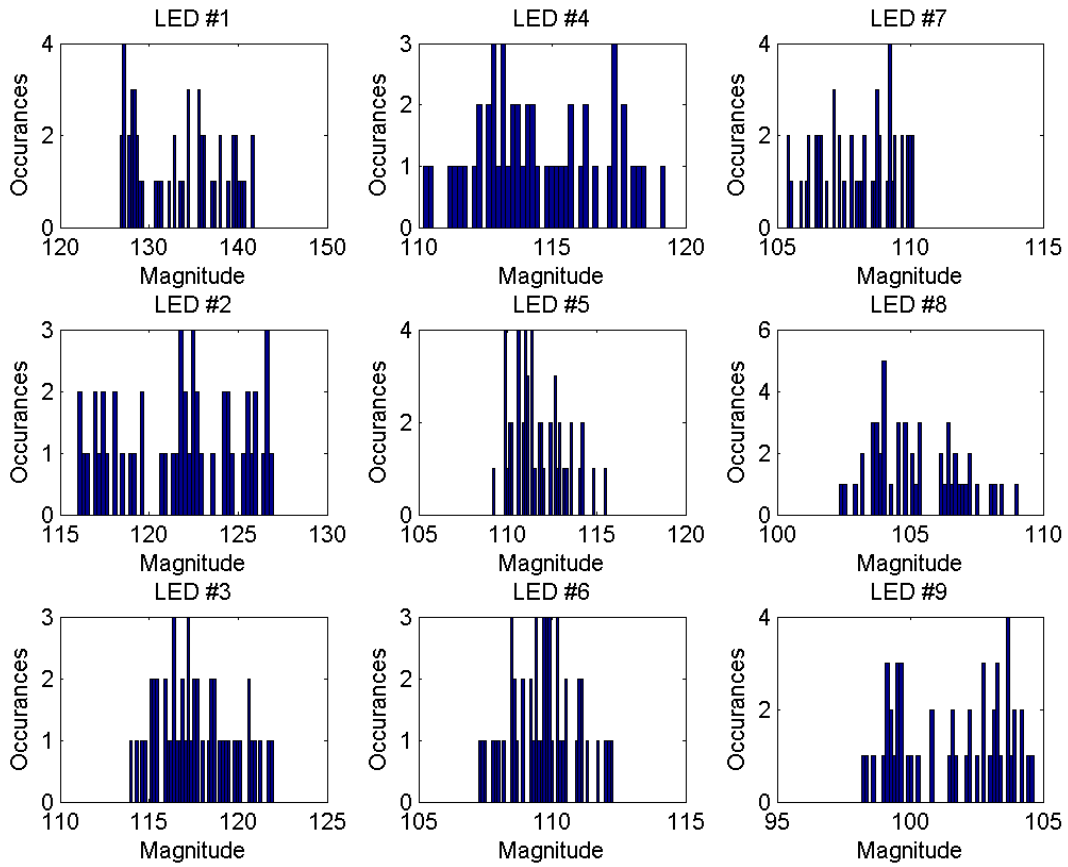


Figure 86: Test 1: Magnitude Distribution at Position 2, by LED

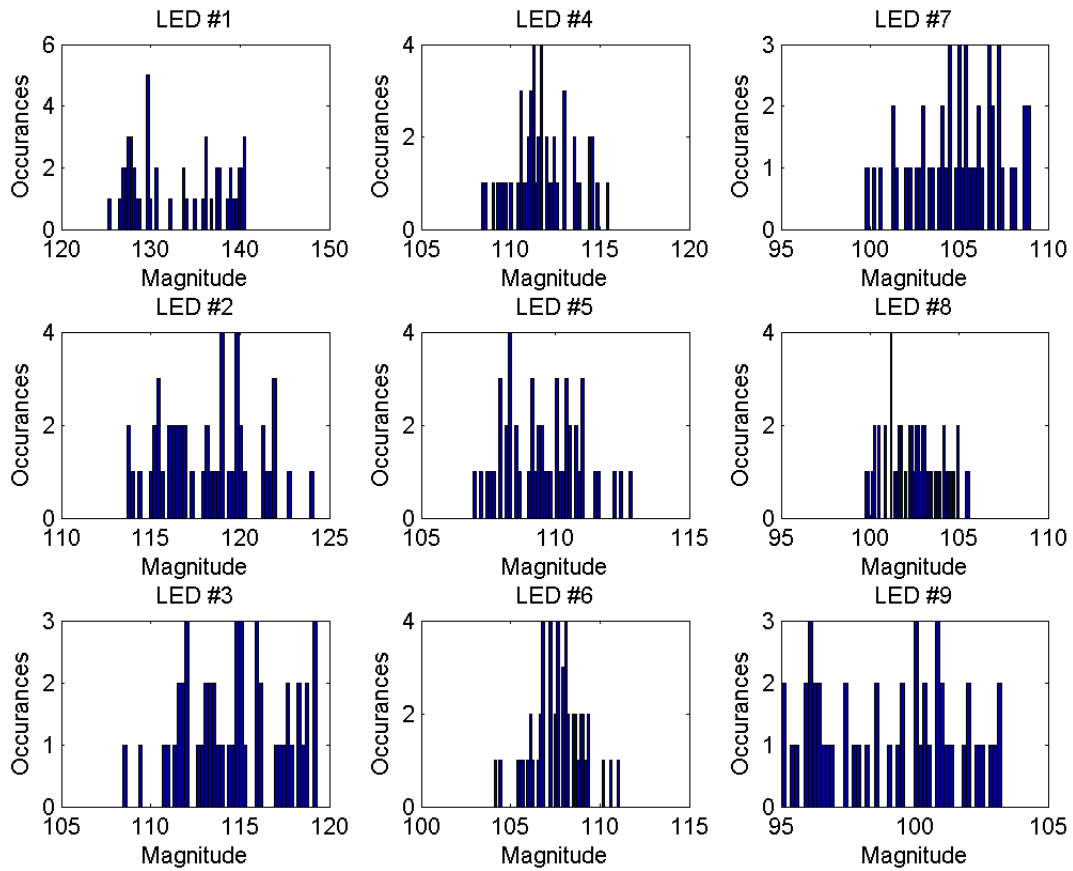


Figure 87: Test 1: Magnitude Distribution at Position 3, by LED

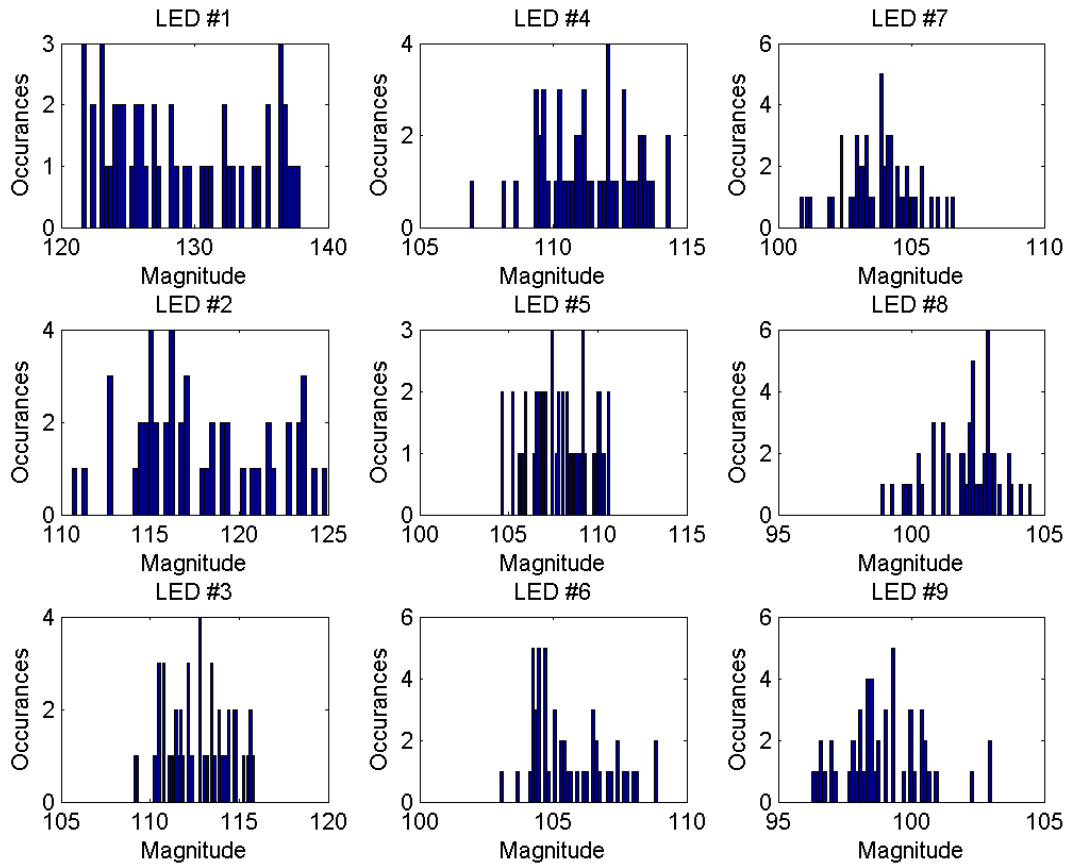


Figure 88: Test 1: Magnitude Distribution at Position 4, by LED

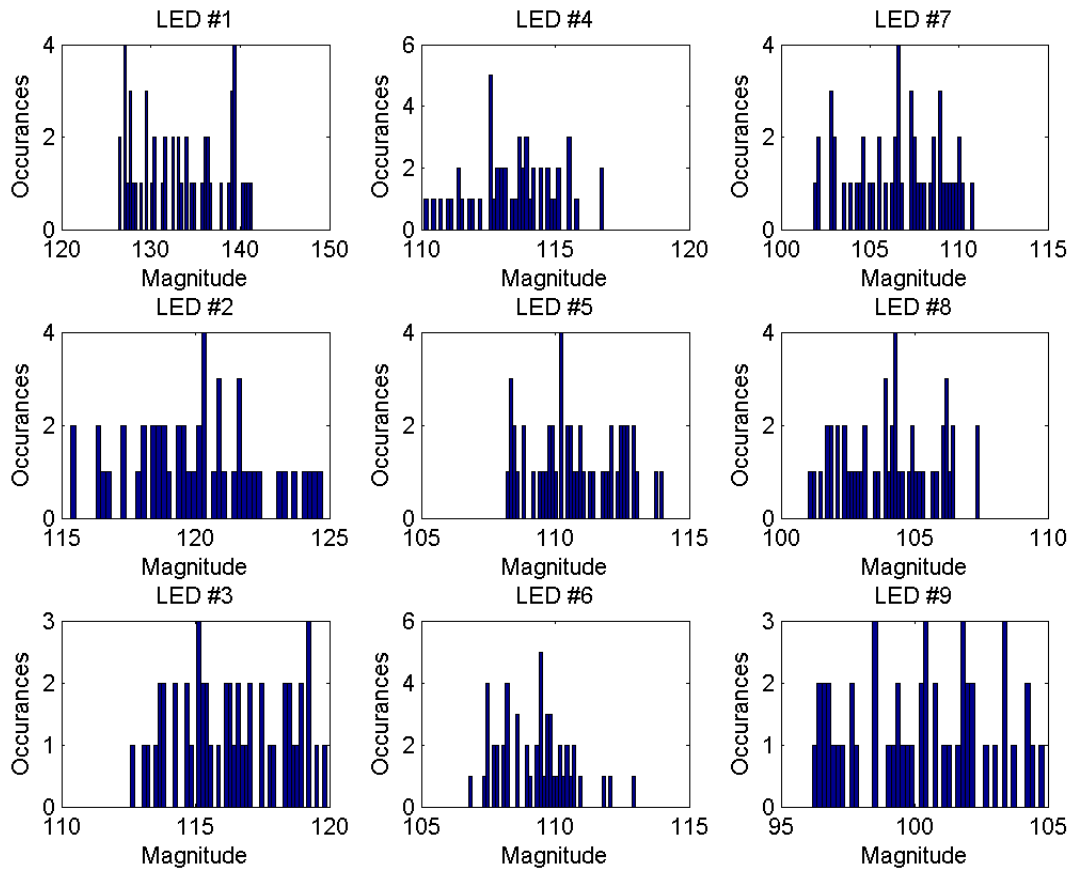
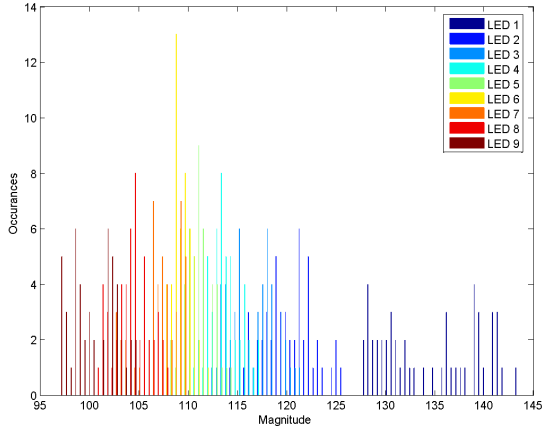
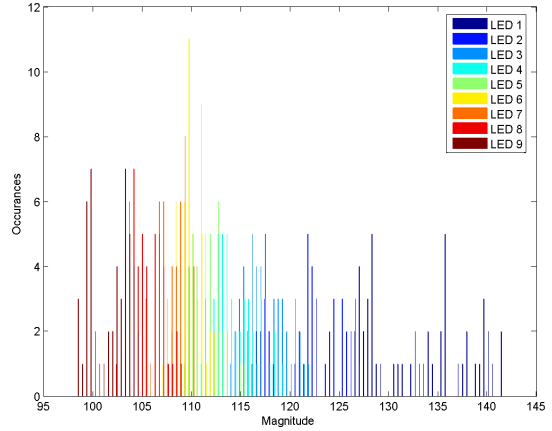


Figure 89: Test 1: Magnitude Distribution at Position 5, by LED

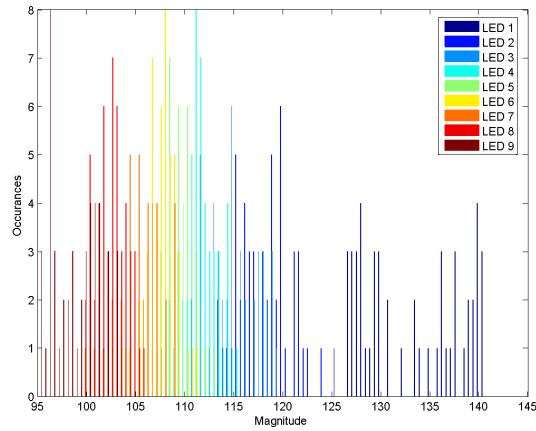


(a) Magnitude Distribution at Position 1

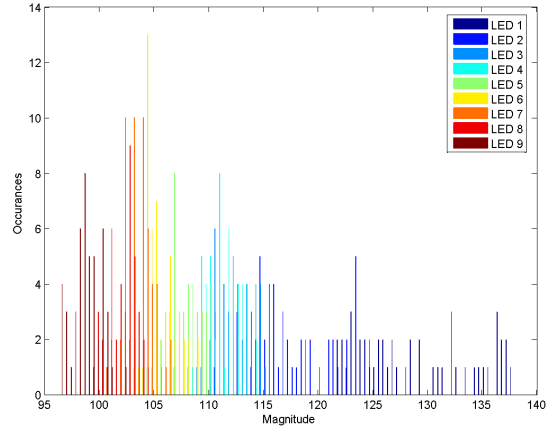


(b) Magnitude Distribution at Position 2

Figure 90: Test 1: Magnitude Distribution at Positions 1 and 2, Combined



(a) Magnitude Distribution at Position 3



(b) Magnitude Distribution at Position 4

Figure 91: Test 1: Magnitude Distribution at Positions 3 and 4, Combined

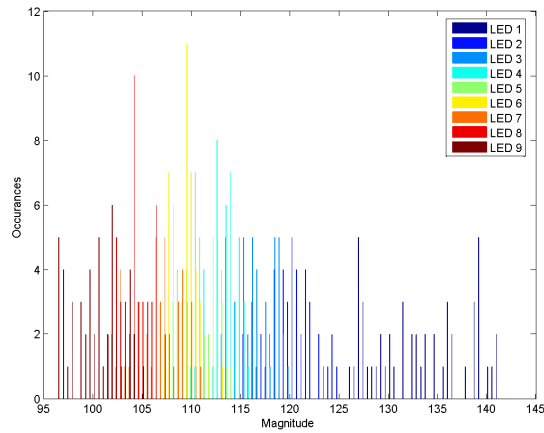


Figure 92: Test 1: Magnitude Distribution at Position 5, Combined

A.2 Test 2 Results

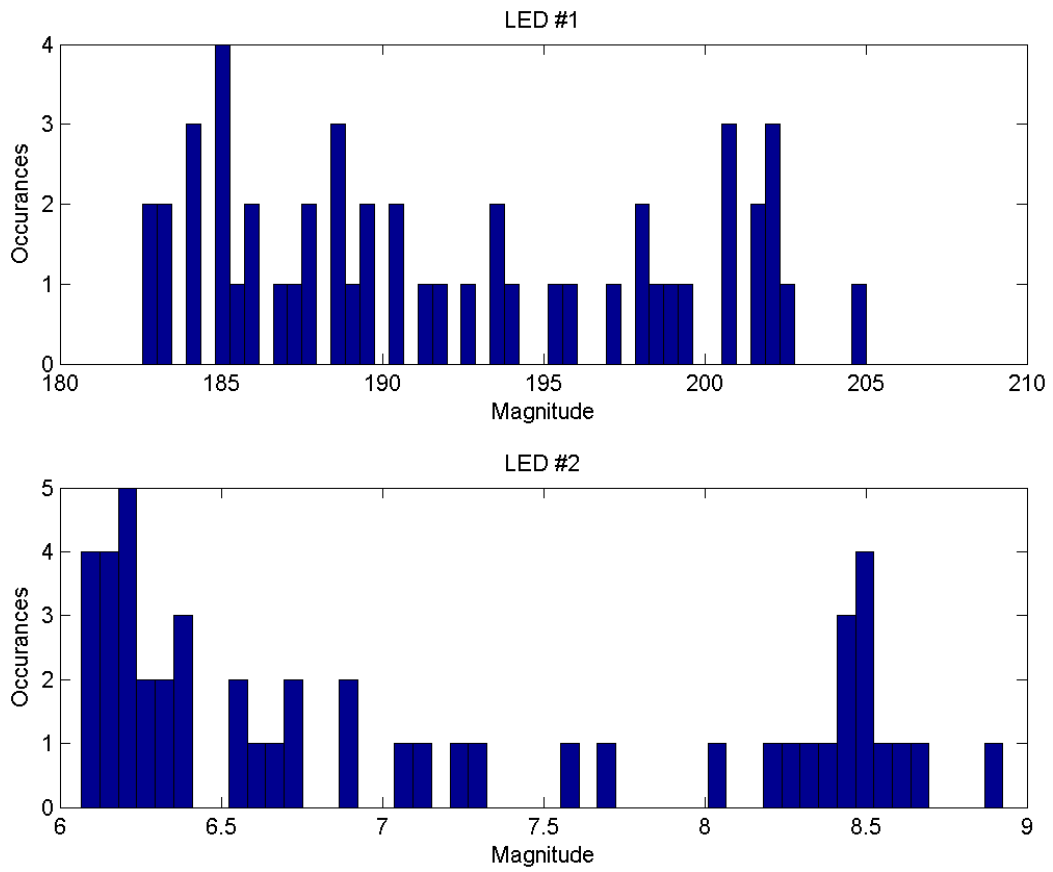


Figure 93: Test 2: Magnitude Distribution at Position 1, by LED

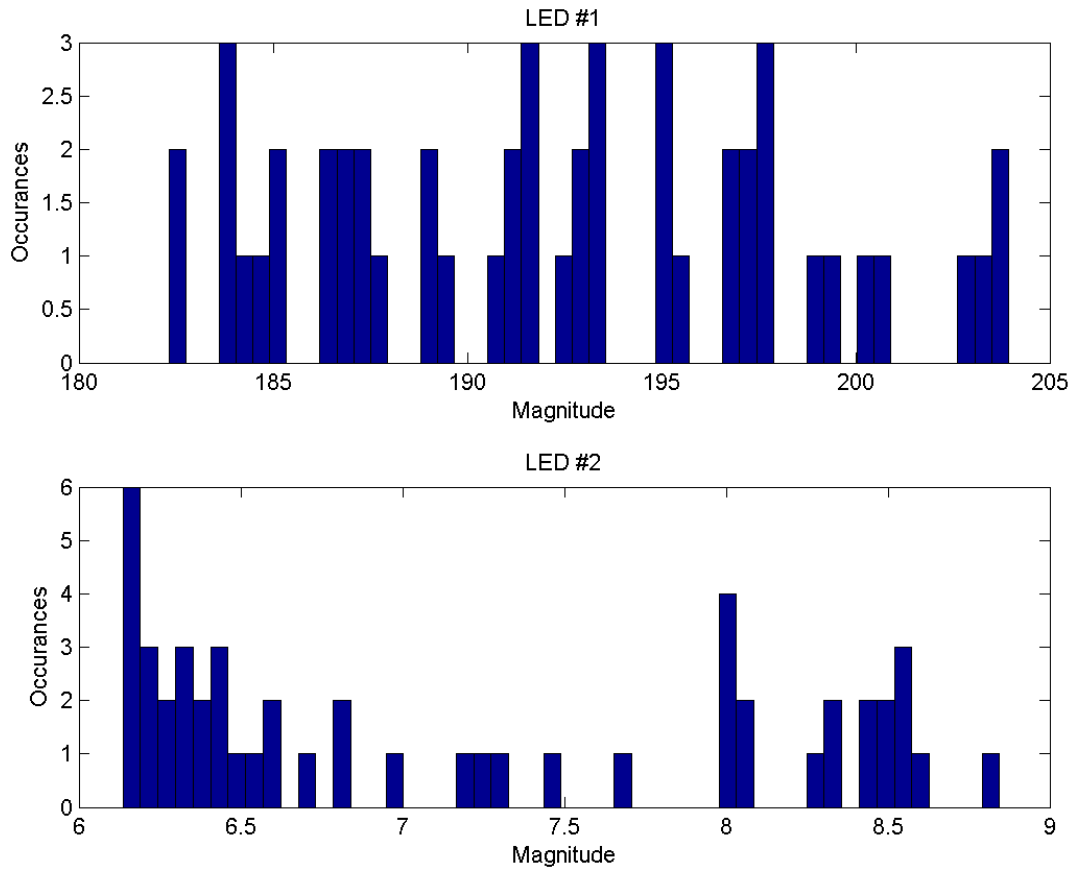


Figure 94: Test 2: Magnitude Distribution at Position 2, by LED

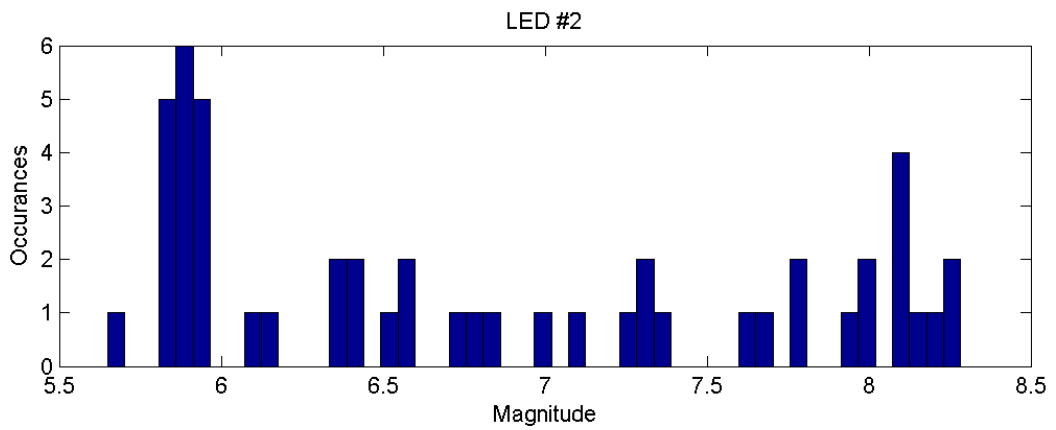
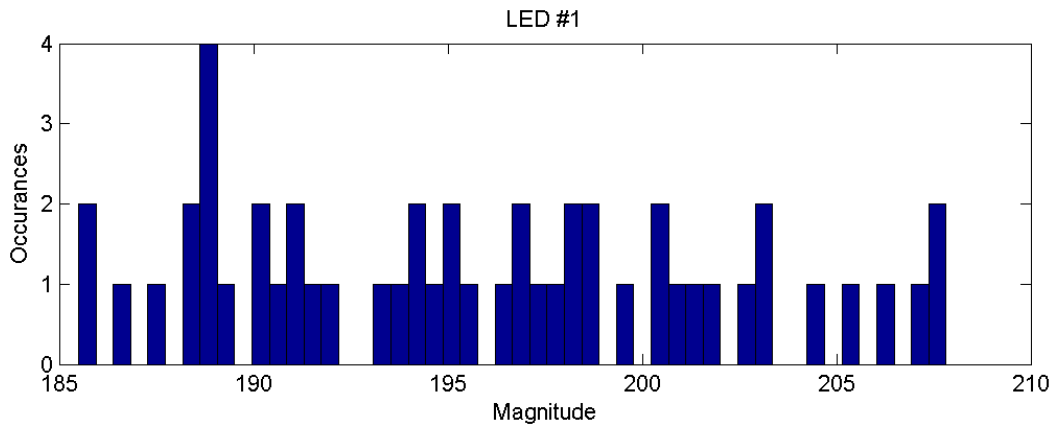
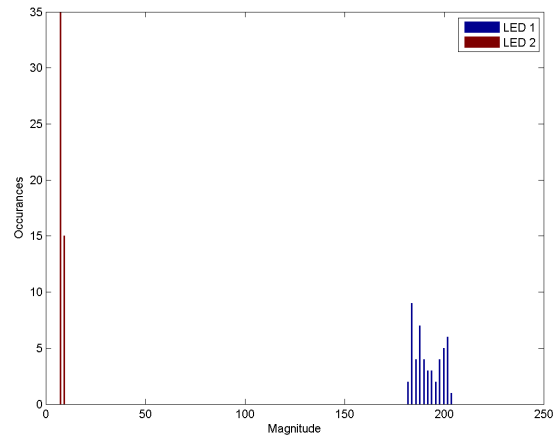
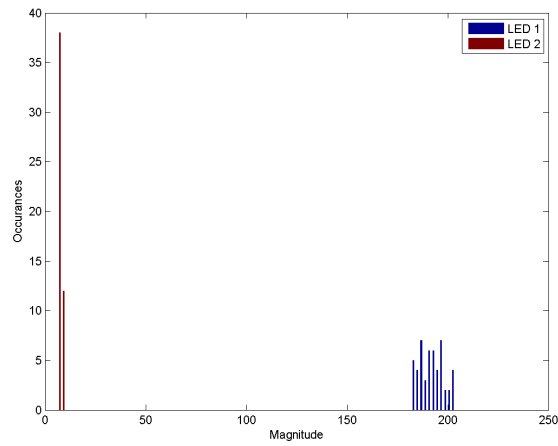


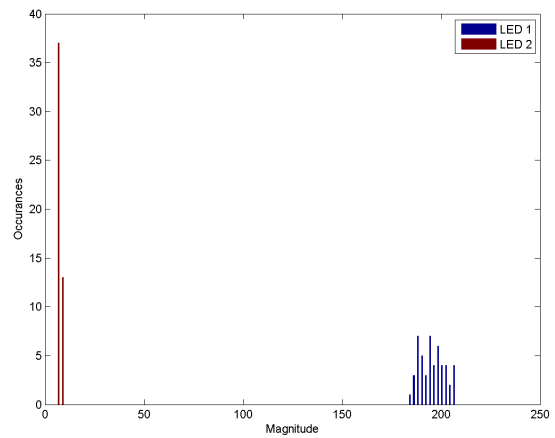
Figure 95: Test 2: Magnitude Distribution at Position 3, by LED



(a) Magnitude Distribution at Position 1

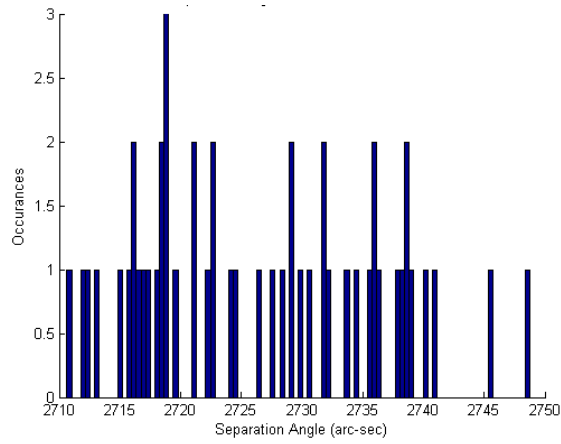


(b) Magnitude Distribution at Position 2

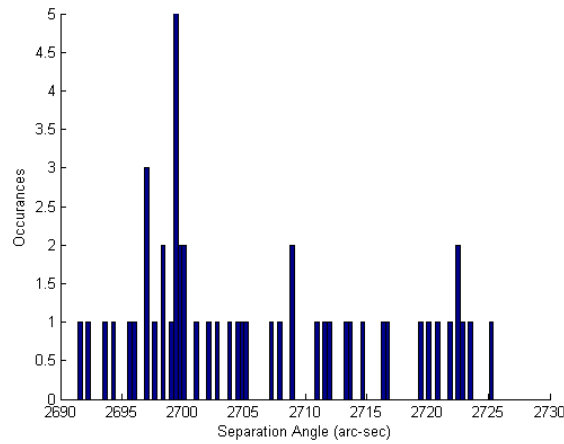


(c) Magnitude Distribution at Position 3

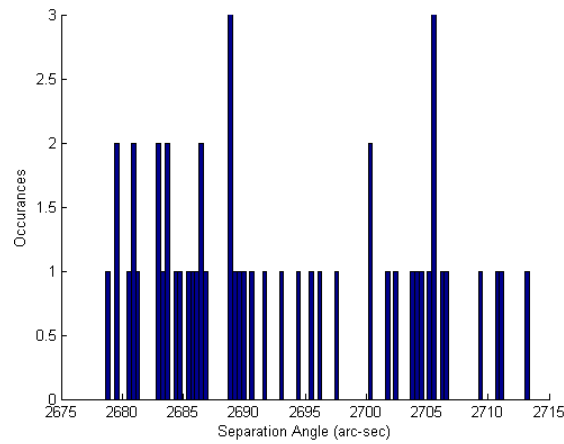
Figure 96: Test 2: Magnitude Distribution by Position, Combined



(a) Angular Separation Distribution at Position 1



(b) Angular Separation Distribution at Position 2



(c) Angular Separation Distribution at Position 3

Figure 97: Test 2: Angular Separation Distribution by Position

A.3 Test 3 Results

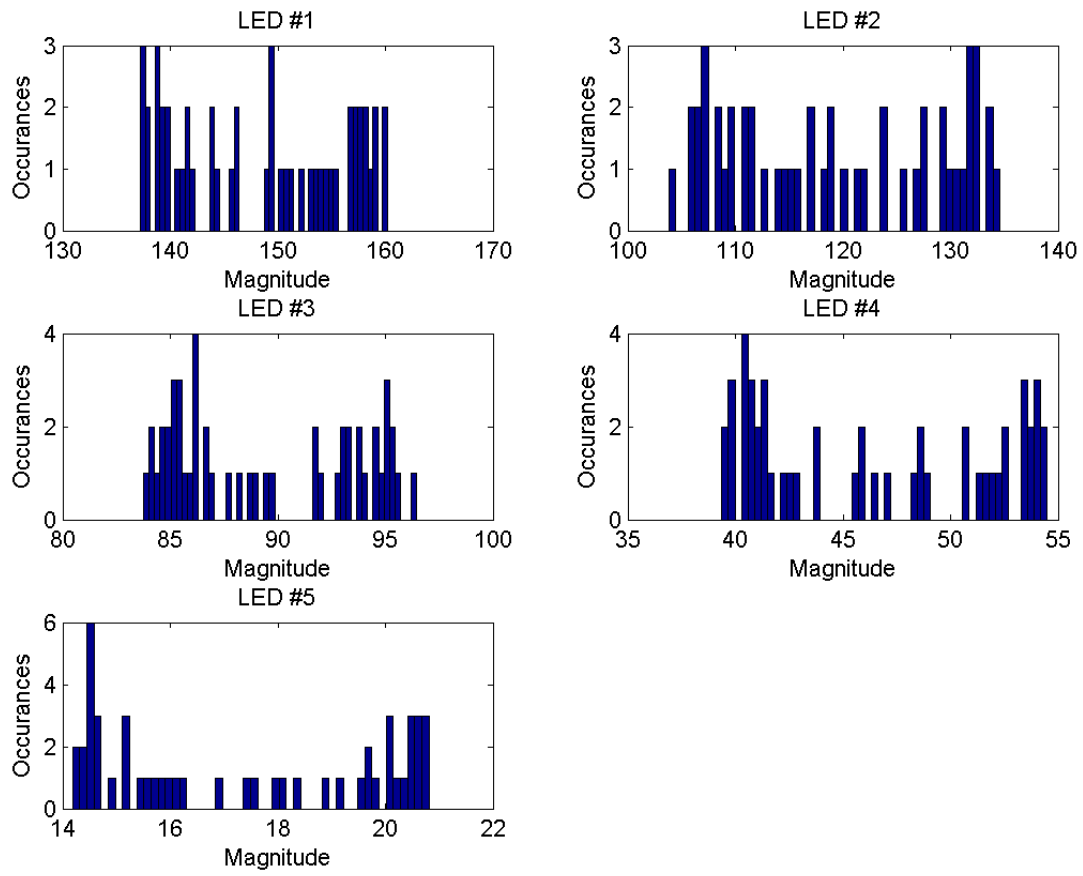


Figure 98: Test 3: Magnitude Distribution at Position 1, by LED

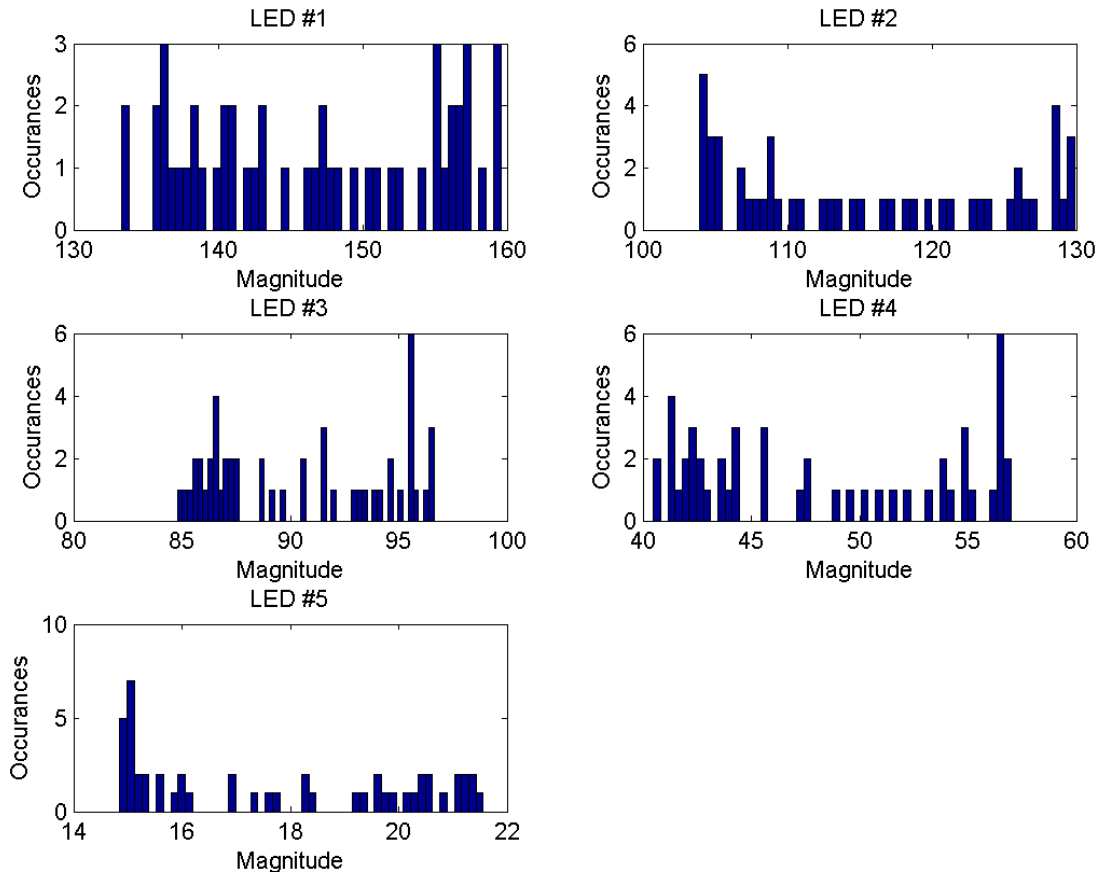


Figure 99: Test 3: Magnitude Distribution at Position 2, by LED

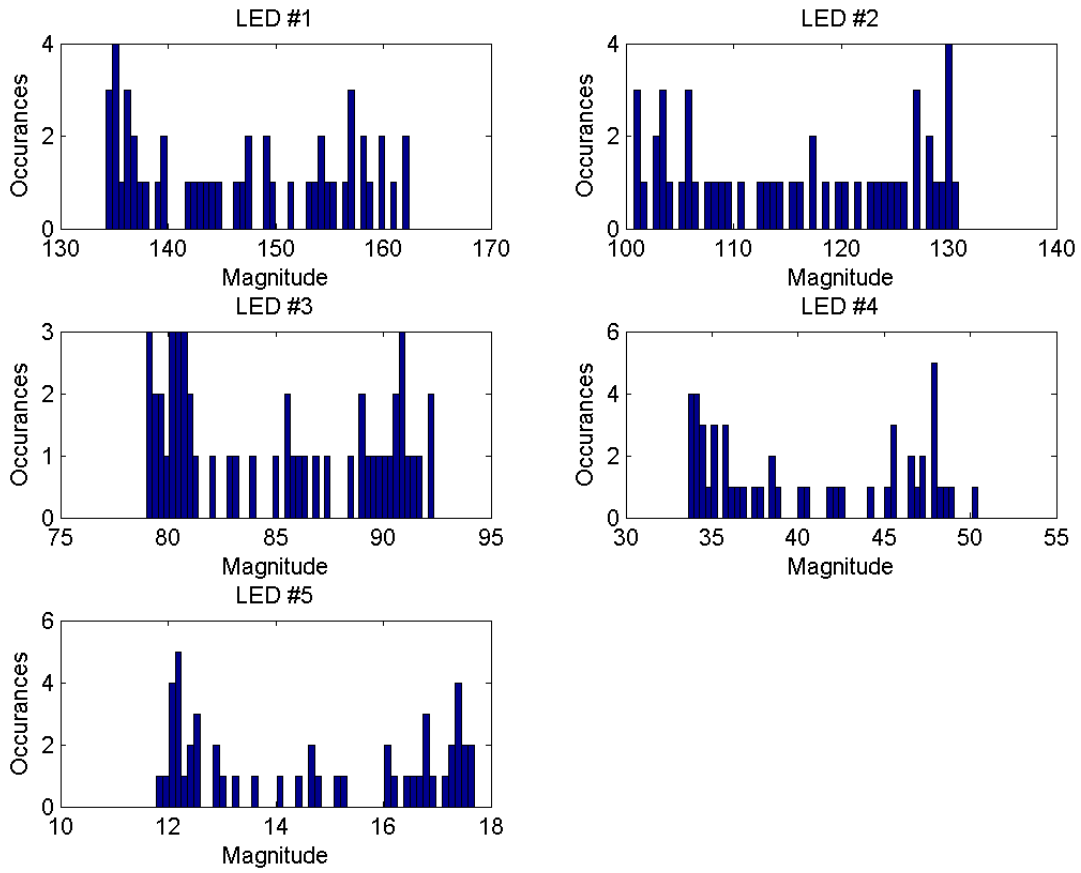


Figure 100: Test 3: Magnitude Distribution at Position 3, by LED

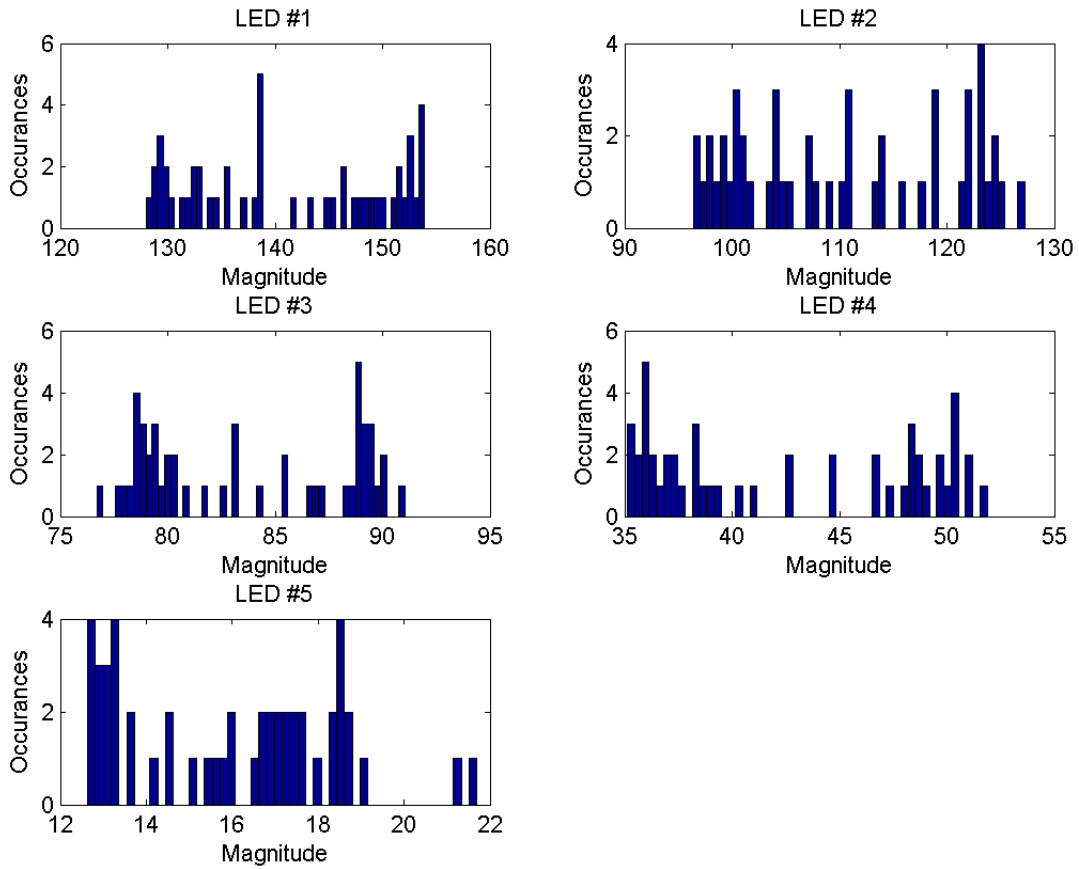


Figure 101: Test 3: Magnitude Distribution at Position 4, by LED

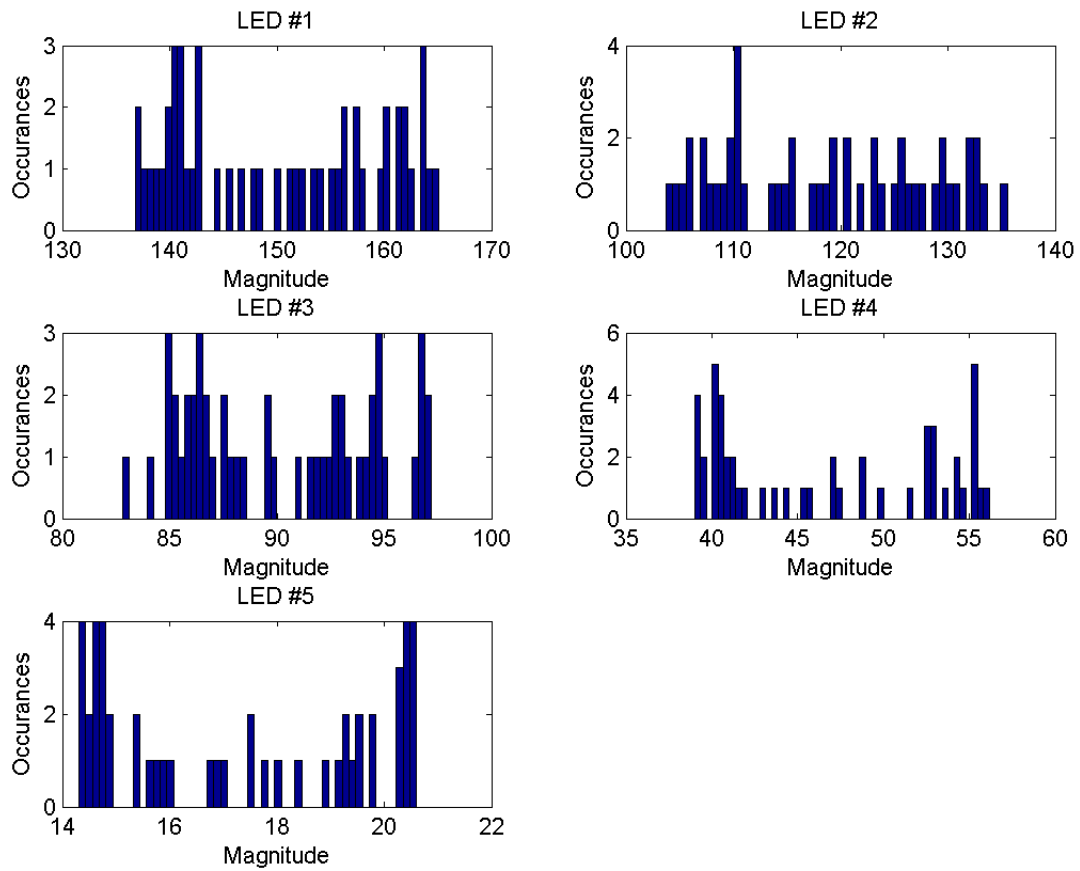
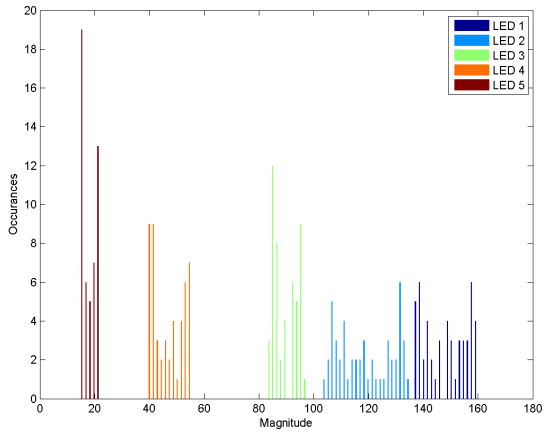
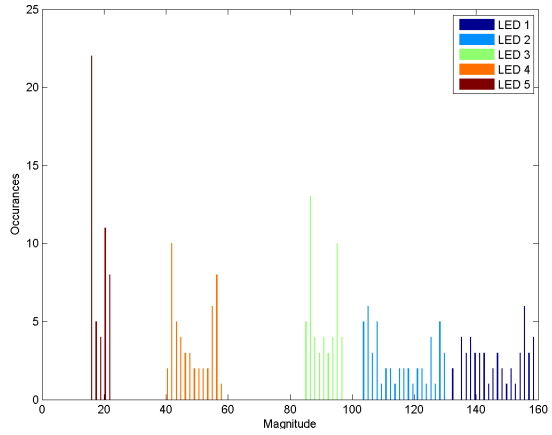


Figure 102: Test 3: Magnitude Distribution at Position 5, by LED

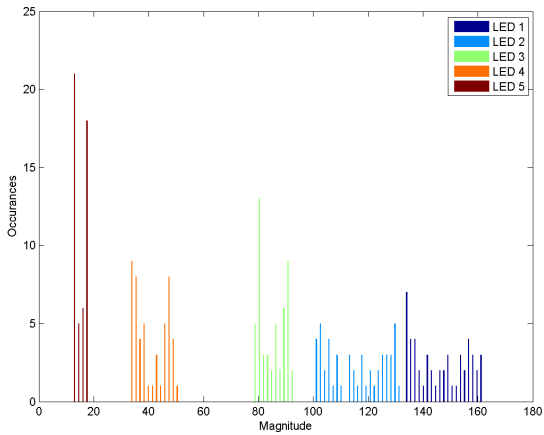


(a) Magnitude Distribution at Position 1

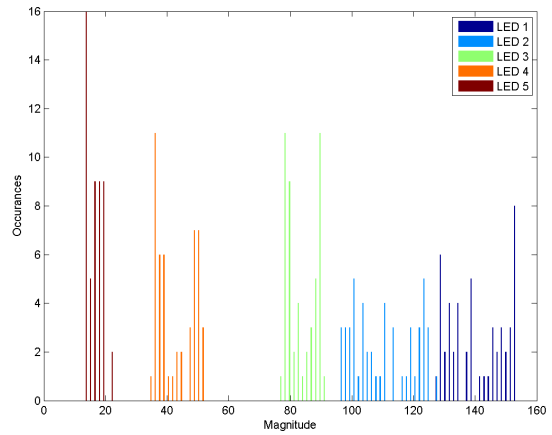


(b) Magnitude Distribution at Position 2

Figure 103: Test 3: Magnitude Distribution at Positions 1 and 2, Combined



(a) Magnitude Distribution at Position 3



(b) Magnitude Distribution at Position 4

Figure 104: Test 3: Magnitude Distribution at Positions 3 and 4, Combined

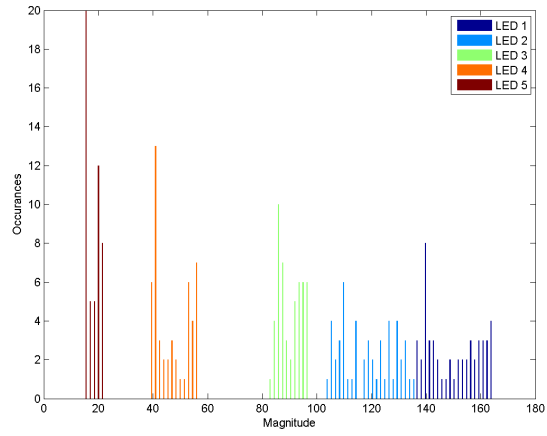


Figure 105: Test 3: Magnitude Distribution at Position 5, Combined

Bibliography

1. Astrium. “A Minitiarized Star Tracker Optical Simulator”. URL http://www.astrium.eads.net/media/document/datasheet_%C2%B5stos_2011-01.pdf. Retrieved 5 Dec 11.
2. Bar-Itzhack, Itzhack Y. and Richard R. Harman. “Optimized TRIAD algorithm for attitude determinatio”. *Journal of Guidance, Control, and Dynamics*, 20(1), July 1996.
3. Boone, B.G., J.R. Bruzzi, W.F. Dellinger, B.E. Kluga, and K.M. Strohhahn. “Optical Simulator and Testbed for Spacecraft Star Tracker Development”. *Optical Modeling and Performance Predictions II*, volume 5967. Aug 2005.
4. Cos, Stefan, Werner Ogiers, Jan Bogaerts, and Stephen Airey. “Image sensors for space: An overview of APS technology”. *Guidance and Control 2007: Proceedings of the 30th annual AAS Rocky Mountain Guidance and Control Conference*, 519. Jul 2007.
5. Diaz, Kenneth D. *Performance Analysis of a Fixed Point Star Tracker Algorithm for Use Onboard a Picosatellite*. Master’s thesis, California Polytechnic State University, San Luis Obispo, August 2006.
6. Eisenman, Allan R. and Carl C. Liebe. “The Advancing State-of-the-art in Second Generation Star Trackers”. *IEEE Aerospace Applications Conference Proceedings*, volume 1, 111–118. Institute of Electrical and Electronics Engineering, Mar 1998.
7. Eisenman, Allan R., Carl C. Liebe, and John L. Jorgensen. “The New Generation of Autonomous Star Trackers”. *SPIE Proceedings*, volume 3221, 524. Sep 1997.
8. Juang, Jet-Nan, Hye Young Kim, and John L. Junkins. “An Efficient and Robust Singular Value Method for Star Pattern Recognition and Attitude Determination”, 2003.
9. Lee, S., G. G. Ortiz, and J. W. Alexander. “Star Tracker-Based Acquisition, Tracking, and Pointing Technology for Deep-Space Optical Communications”. *Interplanetary Network Progress Report*, 42(161), May 2005. URL www.tmo.jpl.nasa.gov/progress_report/42-161/161L.pdf.
10. Liebe, Carl Chrsitian. “Accuracy Performance of Star Trackers - A Tutorial”. *IEEE Transactions on Aerospace and Electronic Systems*, 38(2):587–599, May 2005.
11. Lumex. “Lumex LED Technical Data”. URL <http://www.lumex.com/specs/SML-LXL1209SIC-TR.pdf>. Retrieved 12 Dec 11.
12. McChesney, Christopher G. *Design of Attitude Control Actuators for a Simulated Spacecraft*. Master’s thesis, Air Force Institute of Technology, March 2011.

13. McFarland, C. Douglas. *Near Real-Time Closed-Loop Optimal Control Feedback for Spacecraft Attitude Maneuvers*. Master's thesis, Air Force Institute of Technology, March 2009.
14. Needelman, David D., Rongsheng (Ken) Li, and Yeong-Wei Andy Wu. "Recent Advances in Stellar Attitude Acquisition (SAA) Algorithms and Procedures". *AIAA Guidance, Navigation and Control Conference and Exhibit*. American Institute of Aeronautics and Astronautics, Inc., Aug 2005.
15. Roach, Neal R., Wayne C. Rohe, and Nathan F. Welty. *A Systems Engineering Approach to the Design of a Spacecraft Dynamics and Control Testbed*. Master's thesis, Air Force Institute of Technology, March 2008.
16. Shuster, M. D. and S.D. Oh. "Three-Axis Attitude Determination from Vector Observations". *Journal of Guidance and Control*, 4(1):70–77, Jan-Feb 1981.
17. Shuster, Malcom D. "Focal-Plane Representations of Rotations". *The Journal of the Astronautical Sciences*, 48(2–3):381–390, Apr-Sep 2000.
18. Smith, Noah H. *Localized Distortion Estimation and Correction for the ICESat Star Trackers*. Master's thesis, The University of Texas at Austin, August 2006.
19. Snider, Ryan E. *Attitude Control of a Satellite Simulator Using Reaction Wheels and a PID Controller*. Master's thesis, Air Force Institute of Technology, March 2010.
20. Spratling, Benjamin B. and Daniele Mortari. "A Survey on Star Identification Algorithms". *Algorithms 2009*, 1(2):93–107, Jan 2009.
21. Swenson, Eric D. "Notes from Course: Intermediate Spaceflight Dynamics". Spring 2011.
22. Tappe, Jack A. *Development of Star Tracker System for Accurate Estimation of Spacecraft Attitude*. Master's thesis, Naval Postgraduate School, December 2009.
23. Voronkov, Sergey. "The Dynamic Test Equipment for the Star Trackers Processing". URL http://www.dlr.de/iaa.symp/Portaldata/49/Resources/dokumente/archiv5/1008P_Voronkov.pdf. Retrieved 30 Nov 11.
24. Wahba, Grace. "Problem 65-1, A Least Squares Estimate of Satellite Attitude". *Society of Industrial and Applied Mathematics Review*, 7(3):409, Jul 1965.
25. Wiesel, William E. *Spaceflight Dynamics*. Aphelion Press, Beavercreek, Ohio, USA, 3rd edition, 2010.

Vita

Captain Jorge G. Padro graduated from Northeast High School in Clarksville, Tennessee. He began undergraduate studies at Tennessee State University in Nashville, Tennessee where he graduated with a Bachelor of Science degree in Mechanical Engineering in May 2006. He earned his commission through the Detachment 790 AFROTC at Tennessee State University. His first assignment was at the 846th Test Squadron, Holloman AFB, New Mexico where he served as a Rocket Sled Test Engineer in August 2006. In August 2008, he was assigned to a sister squadron, the 586th Flight Test Squadron, where he served as a Flight Test Engineer. In August 2010, he entered the Graduate School of Engineering and Management, Air Force Institute of Technology. Upon graduation, he will be assigned to the Space Vehicles Directorate, Air Force Research Laboratory.

REPORT DOCUMENTATION PAGE			<i>Form Approved</i> OMB No. 0704-0188	
The public reporting burden for this collection of information is estimated to average 1 hour per response, including the time for reviewing instructions, searching existing data sources, gathering and maintaining the data needed, and completing and reviewing the collection of information. Send comments regarding this burden estimate or any other aspect of this collection of information, including suggestions for reducing this burden to Department of Defense, Washington Headquarters Services, Directorate for Information Operations and Reports (0704-0188), 1215 Jefferson Davis Highway, Suite 1204, Arlington, VA 22202-4302. Respondents should be aware that notwithstanding any other provision of law, no person shall be subject to any penalty for failing to comply with a collection of information if it does not display a currently valid OMB control number. PLEASE DO NOT RETURN YOUR FORM TO THE ABOVE ADDRESS.				
1. REPORT DATE (DD-MM-YYYY) 22-03-2012		2. REPORT TYPE Master's Thesis		3. DATES COVERED (From — To) Aug 2010 – Mar 2012
4. TITLE AND SUBTITLE Development of a Star Tracker-Based Reference System for Accurate Attitude Determination of a Simulated Spacecraft			5a. CONTRACT NUMBER	
			5b. GRANT NUMBER	
			5c. PROGRAM ELEMENT NUMBER	
6. AUTHOR(S) Padro, Jorge G., Capt, USAF			5d. PROJECT NUMBER	
			5e. TASK NUMBER	
			5f. WORK UNIT NUMBER	
7. PERFORMING ORGANIZATION NAME(S) AND ADDRESS(ES) Air Force Institute of Technology Graduate School of Engineering and Management (AFIT/ENY) 2950 Hobson Way WPAFB OH 45433-7765			8. PERFORMING ORGANIZATION REPORT NUMBER AFIT/GAE/ENY/12-M32	
9. SPONSORING / MONITORING AGENCY NAME(S) AND ADDRESS(ES) Air Force Research Laboratory, Space Vehicles Directorate Dr. Frederick A. Leve, Fred.Leve@kirtland.af.mil 3550 Aberdeen Ave SE Bldg 472 Rm 228 Kirtland AFB, NM, 87117 (505) 853-5764			10. SPONSOR/MONITOR'S ACRONYM(S) AFRL/RVSV	
			11. SPONSOR/MONITOR'S REPORT NUMBER(S)	
12. DISTRIBUTION / AVAILABILITY STATEMENT APPROVED FOR PUBLIC RELEASE; DISTRIBUTION UNLIMITED				
13. SUPPLEMENTARY NOTES This material is declared a work of the U.S. Government and is not subject to copyright protection in the United States.				
14. ABSTRACT The goal of this research effort is to investigate the analysis, design, integration, testing, and validation of a complete star tracker and star field simulator system concept for AFIT's satellite simulator, SimSat. Previous research has shown that while laboratory-based satellite simulators benefit from star trackers, the approach of designing the star field can contribute significant error if the star field is generated on a flat surface. To facilitate a star pattern that better represents a celestial sky, a partially hemispherical dome surface is suspended above SimSat and populated with a system of light emitting diodes of various intensities and angles of separation. Test results show that the spherical star pattern surface is effective in minimizing the effects of parallax when imaging in a finite conjugate mode and that more reliable attitude information within 1 degree of accuracy can be attained. The added capability to research star pattern recognition and attitude determination algorithms in the future is also significant.				
15. SUBJECT TERMS star tracker, attitude determination, spacecraft, simulator				
16. SECURITY CLASSIFICATION OF:			17. LIMITATION OF ABSTRACT UU	18. NUMBER OF PAGES 178
a. REPORT U	b. ABSTRACT U	c. THIS PAGE U		
			19a. NAME OF RESPONSIBLE PERSON Dr. Eric D. Swenson	
			19b. TELEPHONE NUMBER (Include Area Code) (937)255-3636, ext 7479 Email. eric.swenson@afit.edu	